MASTERARBEIT | MASTER'S THESIS

Titel | Title

Acquisition Algorithm and Centroid Combination for ARRAKIHS

verfasst von | submitted by

Roman Marwin Zoufal BSc

angestrebter akademischer Grad | in partial fulfilment of the requirements for the degree of

Master of Science (MSc)

Wien | Vienna, 2026

Studienkennzahl lt. Studienblatt | Degree programme code as it appears on the student record sheet:	UA 066 861
Studienrichtung lt. Studienblatt | Degree programme as it appears on the student record sheet:	Masterstudium Astronomy
Betreut von | Supervisor:	Univ.-Prof. Mag. Dr. Franz Kerschbaum

Acknowledgements

First, I want to thank my family for generally supporting me and my decision to study in a field I am truly interested in.
Second, I want to thank my supervisors Franz Kerschbaum and Roland Ottensamer for allowing me to work on such an interesting topic.
Furthermore, I want to thank Gerald Mösenlechner for answering all my questions about the ARIEL centroiding algorithm and ARIEL simulators, as well as Armin Luntzer for his excellent help with the hardware testing.

This research has made use of "Aladin sky atlas" developed at CDS, Strasbourg Observatory, France (Bonnarel et al., 2000; Boch and Fernique, 2014; Baumann et al., 2022)
This research has made use of the SVO Filter Profile Service "Carlos Rodrigo", funded by MCIN/AEI/10.13039/501100011033/ through grant PID2023-146210NB-I00 (Rodrigo et al., 2024, 2012; Rodrigo and Solano, 2020)
This research has made use of the Guide Star Catalogue-III. As there is no acknowledgment for GSC-III available, the GSC-II version is given below:
The Guide Star Catalogue-II is a joint project of the Space Telescope Science Institute and the Osservatorio Astronomico di Torino. Space Telescope Science Institute is operated by the Association of Universities for Research in Astronomy, for NASA under contract NAS 5–26555. The participation of the Osservatorio Astronomico di Torino is supported by the Italian Council for Research in Astronomy. Additional support was provided by European Southern Observatory, Space Telescope European Coordinating Facility, the International GEMINI project and the European Space Agency Astrophysics Division.
This work has made use of Astropy:[1] a community-developed core Python package and an ecosystem of tools and resources for astronomy (Astropy Collaboration et al., 2013, 2018, 2022).
This work has made use of Scipy (Virtanen et al., 2020).
This work has made use of Matplotlib (Hunter, 2007).
This work has made use of Cython (Behnel et al., 2011).

[1]http://www.astropy.org

Abstract

The Analysis of Resolved Remnants of Accreted Galaxies as a Key Instrument for Halo Surveys (ARRAKIHS) mission is an upcoming ESA F-class mission with a planned launch date of 2030. ARRAKIHS aims to study the nature of Dark Matter by observing the structures in the halos of nearby Milky Way-like galaxies. To reach this goal, the satellite needs to achieve surface brightnesses of better than 29 mag/arcsec^2. This requires the use of a so-called Fine Guidance System (FGS), which, in the case of ARRAKIHS, uses the same detectors as the scientific observations to track the movement of stars and reports to the satellite platform in order to have the movement suppressed.

The University of VIEnna (UVIE) has been tasked with developing the Application Software (ASW) including FGS functionality for ARRAKIHS, due to its experience with the development of such systems for prior missions like CHEOPS and ARIEL. The UVIE-FGS consists of two parts. The Acquisition, which finds suitable guide stars, and the Guiding, which tracks the movement of the stars during the exposure in order to stabilize the satellite. In contrast to previous missions, ARRAKIHS performs imaging, which also requires the rotation along the Line of Sight to be stopped. As a result, multiple guide stars are now needed.

The goal of this thesis was to develop and test new algorithms for the Acquisition and centroid combination of the ARRAKIHS-FGS. For the testing, a previously developed simulator was expanded to handle new mission specific phenomena. The algorithms were confirmed to fulfill their precision requirements for a wide range of kinematic conditions and execute sufficiently fast on representative hardware, too. Requirements for the platform were formulated that should ensure successful Acquisition. The main challenges were the autonomous selection and centroid combination for multiple guide stars and the handling of the long frame readout time.

Kurzfassung

Die Analysis of Resolved Remnants of Accreted Galaxies as a Key Instrument for Halo Surveys (ARRAKIHS) Mission ist eine neue F-class mission der ESA. Der Start ist für 2030 geplant. Das Ziel von ARRAKIHS ist es, die Natur der Dunklen Materie (DM) zu studieren, indem die Strukturen in den Halos von nahen milchstraßenähnlichen Galaxien beobachtet werden. Um seine Aufgabe zu erfüllen, muss ARRAKIHS Oberflächenhelligkeiten von besser als 29 mag/arcsec^2 erreichen. Dazu ist ein sogenanntes Fine Guidance System (FGS) notwendig. Das Fine Guidance System (FGS) von ARRAKIHS nutzt einen derselben Detektoren wie die wissenschaftlichen Beobachtungen, um die Bewegung von Sternen zu verfolgen und diese Information an die Satelliten-Plattform weiterzugeben. Die Plattform kann dann, wie erforderlich, die Bewegung des Satelliten gering halten.

Die Universität Wien (UVIE) ist damit beauftragt worden, die Application Software (ASW) mit FGS Funktionalität für ARRAKIHS zu entwickeln, da sie durch andere Missionen wie ARIEL und CHEOPS bereits Erfahrungen damit hat. Das UVIE-FGS besteht aus zwei Komponenten. Die „Acquisition“ lokalisiert geeignete Leitsterne. Das „Guiding“ verfolgt die Position der Leitsterne während der Belichtung und informiert die Plattform über die ungewollten Bewegungen, welche dann von dieser kompensiert werden. Im Gegensatz zu früheren Missionen nimmt ARRAKIHS Bilder auf. Daher muss auch die Bildfeldrotation gestoppt werden, wozu mehrere Leitsterne benötigt werden.

Das Ziel dieser Masterarbeit war es, für das ARRAKIHS-FGS neue Algorithmen für die „Acquisition“ und Kombination von Zentroiden zu entwickeln und zu testen. Um die Tests durchführen zu können, wurde ein bereits von früheren Missionen vorhandener Simulator umgebaut/erweitert damit er mit den neuen missionsspezifischen Effekten umgehen kann. Es wurde gezeigt, dass die Algorithmen die benötigte Präzision für einen weiten Bereich an kinematischen Startbedingungen erreichen können. Außerdem ist die Berechnungsgeschwindigkeit, welche auf repräsentativer Hardware getestet wurde, ausreichend hoch. Um sicherzustellen, dass die „Acquisition“ erfolgreich ist, wurden Anforderungen für die Satelliten-Plattform formuliert. Die größten neuen Herausforderungen waren die automatische Auswahl und Kombination der Zentroide für multiple Leitsterne und die lange Auslesezeit der einzelnen Bilder.

Contents

1. Introduction

The nature of Dark Matter (DM) is a major open question in astrophysics. There are many different theories like the Λ-Cold Dark Matter model (ΛCDM), which need to be tested against real observations. One important area of interest for comparison are the small scale structures like dwarf galaxies in the halos of galaxies. These structures are faint and thus the number of available observations is limited.

The Analysis of Resolved Remnants of Accreted Galaxies as a Key Instrument for Halo Surveys (ARRAKIHS) mission aims to observe the halos of nearby Milky Way (MW)-like galaxies down to the Surface Brightness (SB) needed to reveal the desired structures. ARRAKIHS is an ESA F-class mission carrying two visual and two Near Infrared (NIR) telescopes.

The SB targeted requires long exposure times and stable pointing of the telescopes. The spacecraft's Attitude and Orbit Control System (AOCS) needs to be assisted by a Fine Guidance System (FGS) included in the instrument.

The FGS first needs to automatically find appropriate stars to track (guide stars). This is accomplished by the so-called Acquisition. Afterwards, the so-called Guiding determines the precise positions (centroids) of the guide stars and combines this information into orientation correction information for the satellite. The main focus of this thesis is the development and testing of the algorithms for Acquisitions and centroid combination.

1.1. The ARRAKIHS mission

The Analysis of Resolved Remnants of Accreted Galaxies as a Key Instrument for Halo Surveys (ARRAKIHS) mission has been selected as an F-class mission by ESA in November 2022 as part of the Cosmic Visions program (ESA, 2022). The ARRAKIHS consortium is responsible for the planning and construction of the scientific instruments carried by ARRAKIHS. It has members from eight European countries and collaborates with research institutes from six more (ARRAKIHS Consortium, 2025), an overview of the core team is given in Figure 1.1.

The main goal of ARRAKIHS is to perform observations with unprecedented depth in order to study and compare them with predictions from the Λ-Cold Dark Matter model (ΛCDM) (ARRAKIHS Project Team, 2024a).

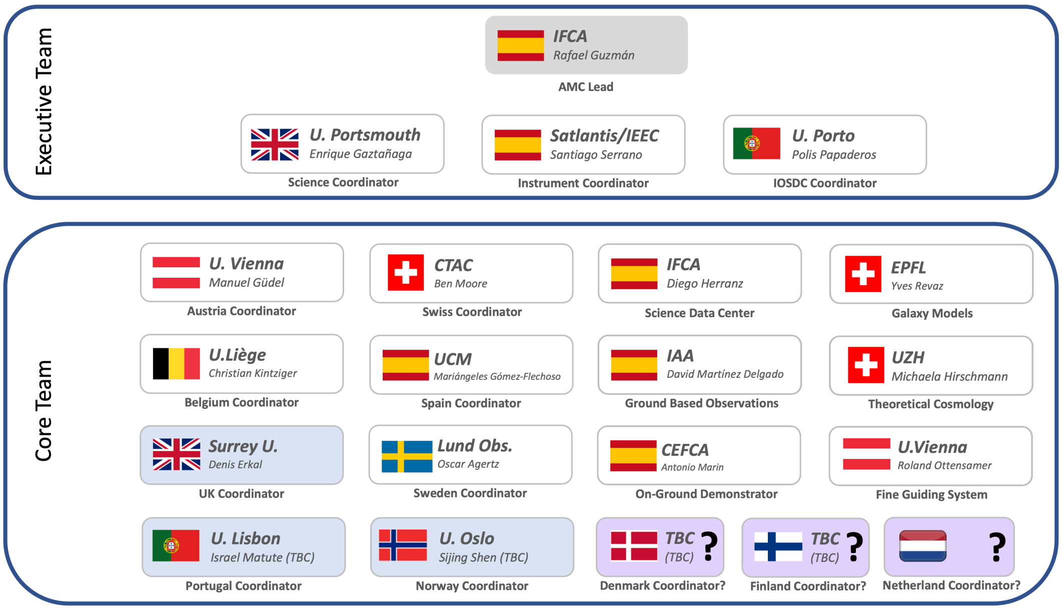

Figure 1.1.: Overview of the executive and core team of the ARRAKIHS consortium (ARRAKIHS Consortium, 2025)

1.1.1. Science Goals and Requirements

The scientific goals of ARRAKIHS are split into three science cases, described hereafter. Those form the basis of all requirements for the ARRAKIHS mission.

Science Case A: Satellite Galaxies beyond the Local Group

The first ARRAKIHS science case aims to obtain a statistically representative sample of dwarf-galaxy-sized sub-halos that are embedded in the halos of nearby MW-like galaxies, by observing down to a Surface Brightness (SB) of better than $29\,\mathrm{mag/arcsec^2}$. The number of dwarf-galaxy-sized sub-halos predicted by CDM models (including ΛCDM) is higher than the number observed thus far. As it is challenging to reach such low SB from the ground, only the MW and M31 have been mapped to the ultra-faint regime at this time. Therefore, the discrepancy mentioned could be due to a lack of data, which ARRAKIHS aims to rectify. An additional inconsistency between the models and current observations is the alignment of satellite galaxies into flattened, co-rotating planes. In ΛCDM such distributions are very rare ($< 5\,\%$), while they seem to be observed for MW and M31. More observations will allow to quantify the rate of occurrence (Guzmán, 2022).

Science Case B: Measuring the Statistics and Shapes of the Stellar Streams

Studying so-called stellar streams is the goal of the second ARRAKIHS science case. Stellar streams are created when the gravitational potential of a galaxy disrupts an infalling satellite galaxy or a globular cluster and strips away stars. The distribution and abundance of these streams allows to probe the abundance of sub-halos, the recent merger history and the shape of the gravitational potential of the parent galaxy. As mentioned for satellite galaxies, a statistically representative sample is required for comparison with simulations. Since stellar streams typically reach SB of lower than 29 mag/arcsec^2, ground based observations have not been able to produce a sufficient sample. In order for ARRAKIHS to observe the stellar streams, the telescope's Field of View (FoV) needs to cover the virial radius of the targeted galaxy. For a galaxy at a distance of 25 Mpc and a virial radius of 300 kpc a FoV diameter of 1.35° is required (Guzmán, 2022).

Science Case C: Stellar Streams as Tracers of the Intra-Halo Light (IHL) in the Local Universe

The third ARRAKIHS science case is directly connected to the second one. By using the properties of the stellar streams observed, constraints for the number of stars that are stripped and ejected into intergalactic space during merger events can be obtained. These constraints can then be used for simulations that aim to predict the Intra-Halo Light (IHL), which is produced by the ejected stars. The simulation results then can be used to estimate the contribution of the IHL to the fluctuations found in the cosmic IR background. The origin of these fluctuations is currently unclear. An alternative scenario is that they are caused by the emissions from the first stars and black holes during re-ionization (Guzmán, 2022).

Requirements for the ARRAKIHS Survey

Combining the needs for all three science cases, the ARRAKIHS survey has to achieve the requirements listed in Table 1.1 (Guzmán, 2022). The number of targets was reduced from 100 in Guzmán (2022) to >75 in ARRAKIHS Project Team (2024a).

1.1.2. ARRAKIHS Instrumentation

The instrumentation carried by the ARRAKIHS satellite consists of two iSIM-170 binocular telescopes. One is operated in the visual (VIS-1 and VIS-2) and the other one in the NIR (NIR-1 and NIR-2), leading to a total of four instrument channels. All four channels are used for scientific observations, but the NIR channels are utilized by the FGS, too (Guzmán,

Category	Requirements
Vis imaging	SB > 29 mag/arcsec^2
NIR imaging	SB > 29 mag/arcsec^2
Spatial resolution	2.6″
Field of View	1.35° × 1.35°
Target number	>75 galaxies

Table 1.1.: Overview of the requirements for the ARRAKIHS survey (Guzmán, 2022; ARRAKIHS Project Team, 2024a)

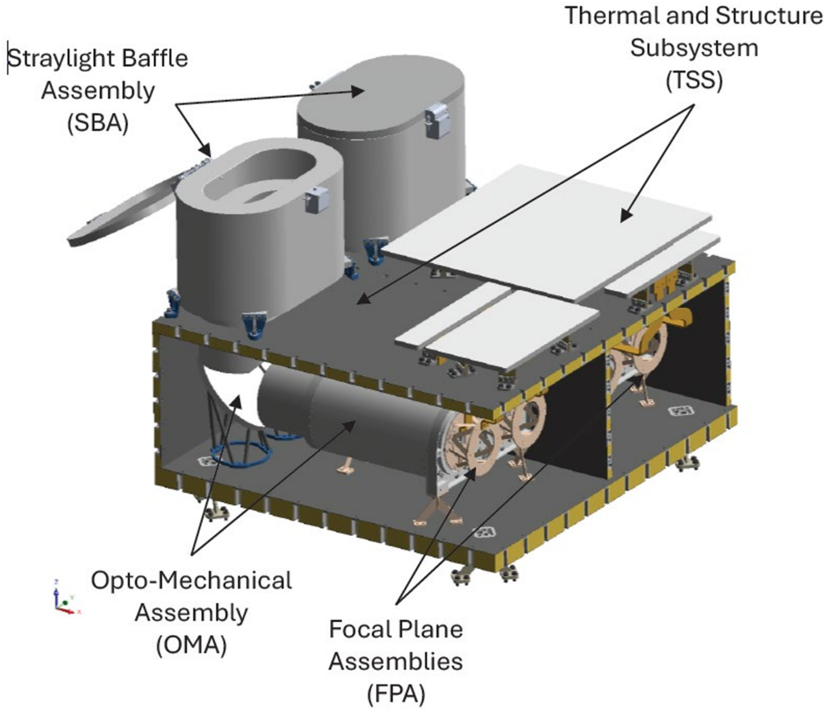

Figure 1.2.: Diagram of the ARRAKIHS Instrument (ARRAKIHS Project Team, 2024a, Figure 5)

2022). Each of the telescopes will have its own straylight baffle and 45° folding mirror, as can be seen in Figure 1.2.

iSIM-170 Telescope

The iSIM-170 telescopes carried by ARRAKIHS are developed by SATLANTIS. Both telescopes making up a iSIM-170 module are identical and have a modified Maksutov-Cassegrain design with an effective aperture of 150 mm, a focal length of 1500 mm and a FoV diameter of about 1.4° (Guzmán, 2022). A schematic can be seen in Figure 1.3.

VIS Detectors

For the visual detectors, none of the two CCD options originally described in Guzmán (2022) were chosen. Currently, the plan is to use a CMOS detector from the CIS-300 family developed by Teledyne (team members, 2025).

NIR Detectors

In the NIR, ARRAKIHS will use H2RG detectors developed by Teledyne Imaging. The main properties are summarized in Table 1.2. The detector will be operated in up-the-

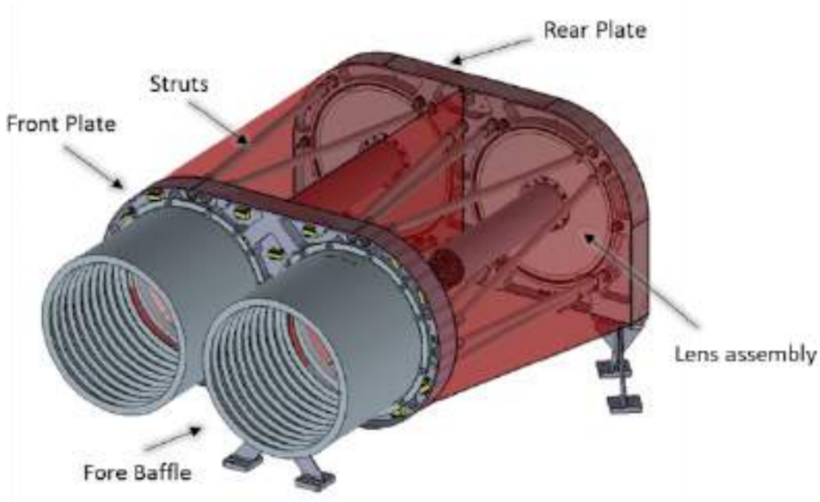

Figure 1.3.: Schematic of the iSIM-170 binocular telescope (Guzmán, 2022, Figure 9)

Image size	2048 x 2048 px
Wavelength	400 nm to 1600 nm
Quantum efficiency	$> 80\,\%$
Pixel pitch	18 µm
Plate scale	$2.3''$/px
RN	$5\,e^-$
DC	$0.5\,e^-/(s\,px)$
Temperature	140 K
Readout time	$\approx 1.5\,s$

Table 1.2.: General properties of the H2RG detectors to be used for the NIR channels of ARRAKIHS (Guzmán, 2022)

ramp sampling mode (described below). One detector feature crucial for the FGS is the ability to readout and individually reset configurable regions of the detector. Those regions will be used as guiding windows (Guzmán, 2022).

MACC

Multiple ACCumulated sampling (MACC) is a technique employed for NIR detectors to reduce the impact of high readout noise. The detector is repeatedly read out non-destructively (up-the-ramp sampling mode). Several reads are averaged to a so-called group. At the end of the exposure, a fit is performed using the groups as data points and the signal is obtained from the slope of the fit (Kubik et al., 2016). A schematic example for a MACC setup can be seen in Figure 1.4.

For ARRAKIHS, the NIR channels will use MACC (team members, 2025). The MACC

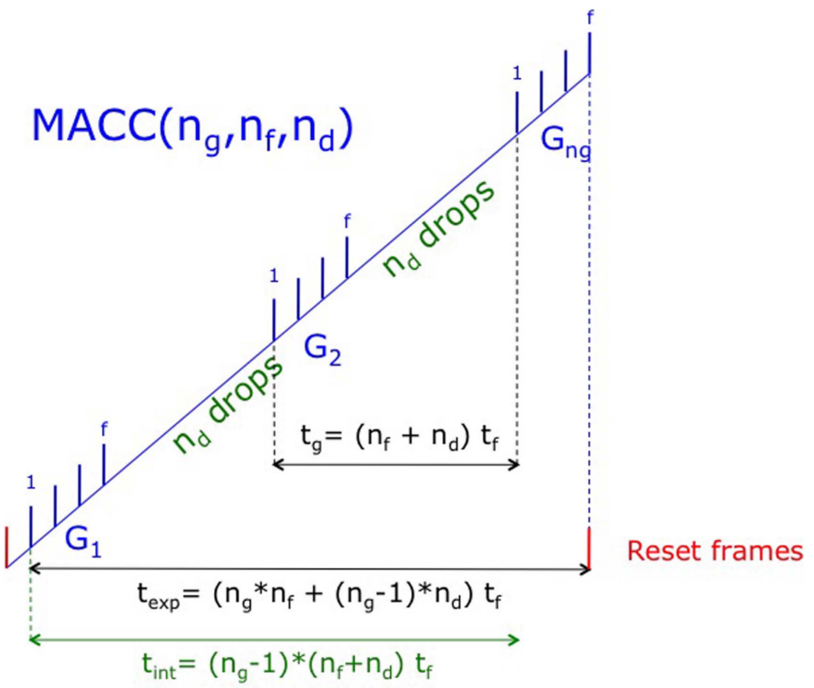

Figure 2. Multiple accumulated sampling MACC(n_g, n_f, n_d) with n_g—number of equally spaced groups sampled up the ramp, n_f—number of frames per group and n_d—number of dropped frames between two successive groups. (A color version of this figure is available in the online journal.)

Figure 1.4.: Figure 2 from Kubik et al. (2016), showing the schematic of a MACC setup

implementation used is the same one utilized for Euclid and described in Kubik et al. (2016).

1.1.3. Mission Profile

The mission profile of ARRAKIHS foresees placing the satellite in a dawn-dusk sun-synchronous Low Earth Orbit (LEO), with an altitude between 650 km and 800 km. During observations the satellite will be pointed more than 90° away from the sun, more than 15° away from the moon and have at most a LoS-Zenith angle[1] of 60° (ARRAKIHS Project Team, 2024a).

The nominal science operations phase is planned to last for three years, during which the satellite will perform observations almost continuously with the exception of South Atlantic Anomaly (SAA) passages. After slewing to a target and stabilizing its pointing, the satellite activates the FGS and performs one or multiple 10 min long exposures. One or more consecutive exposures of the same target are called a visit. In order to improve the quality of the final science images, each exposure during a visit is offset on the scale of arc-seconds and the different visits have offsets on the scale of arc-minutes. In total, each target will have a total of 900 exposures, i.e. a total of 150 hours of observation time (ARRAKIHS Project Team, 2024a).

[1] As per ARRAKIHS Project Team (2024a), the LoS-Zenith angle is defined as the angle between the spacecraft's LoS and the direction coincident with the vector from the center of the Earth to the spacecraft center of mass.

1.2. Fine Guidance Systems

Starting with the invention of photographic plates, the need arose to keep a telescope stably pointed onto the desired target in order to produce sharp images. While this was initially accomplished by hand, guiding systems are automated nowadays.

For space telescopes, guiding systems are especially important, because even small forces will cause movement as they cannot be stabilized against a larger nearby object like the ground. The task of any guiding system is to continuously measure and counteract the movements caused by external forces and the internal processes of the spacecraft.

The following two subsections briefly describe common terminology related to pointing errors and provide a demonstration of the improvements to observation quality possible by the use of a Fine Guidance System (FGS) in the case of ARIEL time series.

1.2.1. Terminology

Pointing errors and related terminology are described in ESSB-HB-E-003 Working Group (2011) based on European Cooperation for Space Standardization (2008). The definitions given there will be used in this thesis, with one exception elaborated below.

A pointing error e_p describes the deviation of the telescope's Line of Sight (LoS) from the desired orientation due to internal or external physical phenomena. The actual pointing error e_p is caused by the combined contributions of Pointing Error Sources (PESs). PESs can be split into two groups based on their time dependence. A time-random PES randomly changes over time. Examples for time-random PES are environmental disturbances like solar pressure noise or sensor bias as well as noise of the detector used for guiding. A time-constant PES remains unchanged, like the misalignment of a sensor and the telescope.

There are different indices for describing the pointing error. Their definitions are given in Table 1.3 and an example is shown in Figure 1.5.

European Cooperation for Space Standardization (2008) describes the PDE as the difference between the mean of two time intervals. For defining requirements for Acquisition in ARRAKIHS (see below) it was decided to use an alternative instantaneous description for the PDE (team members, 2025). The new definition is given in Equation (1.1), where the PDE is now defined as the difference of the APE at two points in time t_1 and t_2. A comparison between the two versions in shown in Figure 1.6. The new definition now allows to formulate requirements which sharply restrict the LoS to a given area. For the purposes of this thesis, this instantaneous definition is used.

$$\mathrm{PDE}(t_1, t_2) = e_p(t_1) - e_p(t_2) \tag{1.1}$$

Name	Definition	Calculation
Absolute Performance Error (APE)	Difference between target and actual parameter at time t	$\text{APE}(t) = e_p(t)$
Mean Performance Error (MPE)	Mean APE over a time interval Δt	$\text{MPE}(\Delta t) = \bar{e_p}(\Delta t) = \frac{1}{\Delta t}\int_{\Delta t} e_p(t)dt$
Relative Performance Error (RPE)	Difference between APE at time t and MPE for time interval Δt containing t	$\text{RPE}(t, \Delta t) = e_p(t) - \bar{e_p}(\Delta t)$
Performance Drift Error (PDE)	Difference of the MPE for two time intervals Δt_1 and Δt_2 within a single observation	$\text{PDE}(\Delta t_1, \Delta t_2) = \bar{e_p}(\Delta t_1) - \bar{e_p}(\Delta t_2)$
Performance Reproducibility Error (PRE)	Difference of the MPE for two time intervals Δt_1 and Δt_2 for different observations	$\text{PRE}(\Delta t_1, \Delta t_2) = \bar{e_p}(\Delta t_1) - \bar{e_p}(\Delta t_2)$

Table 1.3.: Different pointing error indices following the definitions from ESSB-HB-E-003 Working Group (2011) and European Cooperation for Space Standardization (2008)

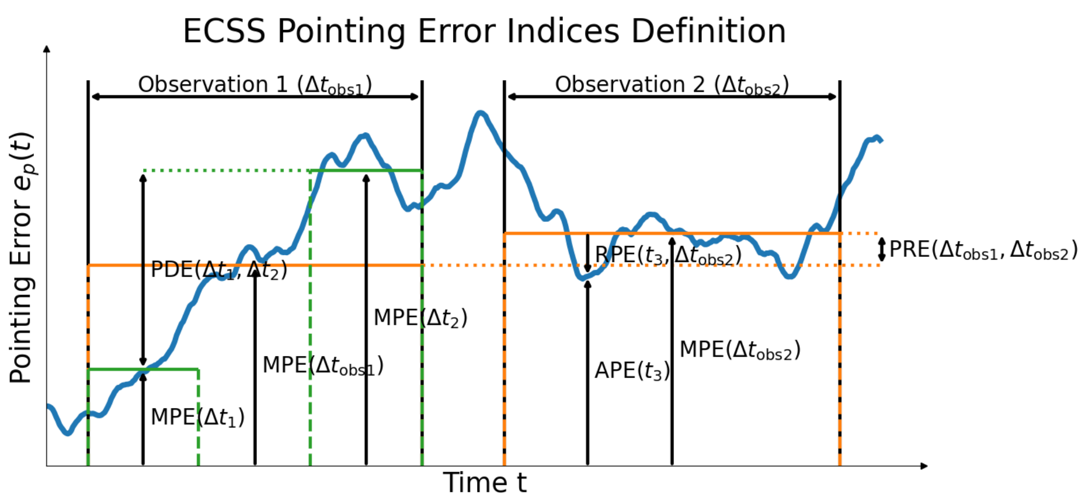

Figure 1.5.: Definitions of pointing error indices as defined in European Cooperation for Space Standardization (2008)

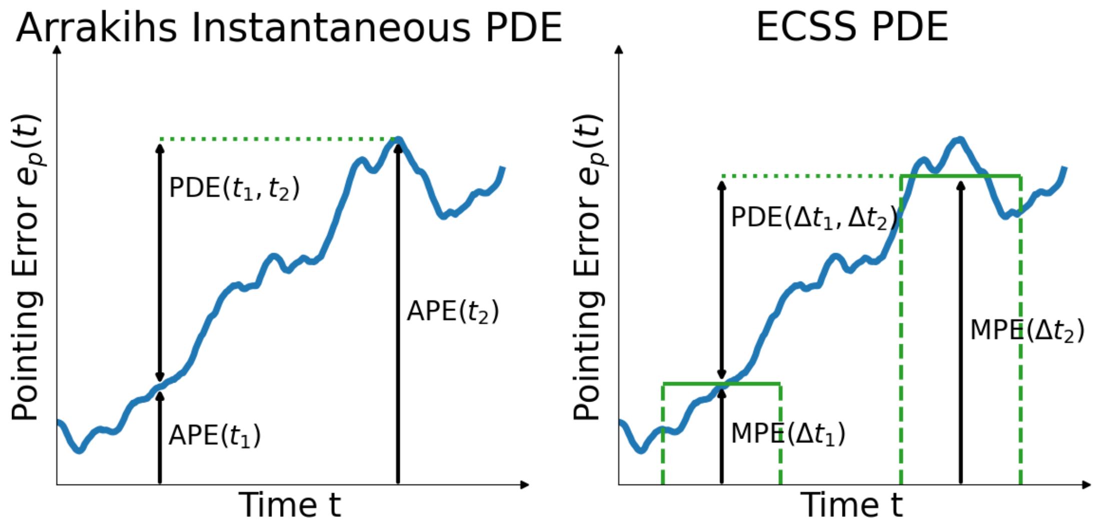

Figure 1.6.: Comparison between PDE definitions from ARRAKIHS (left) (during Acquisition) and European Cooperation for Space Standardization (2008) (right)

1.2.2. FGS Observation Improvement for ARIEL

The Atmospheric Remote-sensing Infrared Exoplanet Large-survey (ARIEL) mission also employs a FGS in order to improve pointing stability. The analysis in Figure 1.7 shows the same star with a true signal of 4500 ADU being observed for a period of 120 s at 10 Hz (1200 data points). As can be seen, a growing jitter amplitude increases the error of the observed stellar signal. By using the FGS the maximum jitter amplitude can be limited thus improving the quality of the observed results (Mösenlechner, 2026).

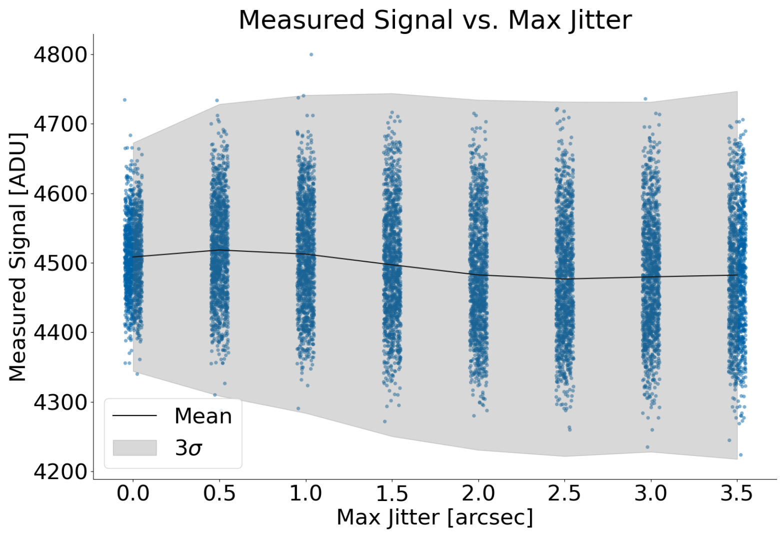

Figure 1.7.: Signal error for different jitter amplitudes in simulations for the ARIEL mission (Mösenlechner, 2026)

1.3. Attitude description

The attitude describes the rotational orientation of an object (e.g., a satellite) in 3D Euclidean space (Großekatthöfer and Yoon, 2012). There are three common mathematical descriptions for a change in attitude (rotation): Direction Cosine Matrix (DCM), Euler angles and quaternions (Großekatthöfer and Yoon, 2012). In the following these methods are described in detail and some related terminology used throughout this thesis is given.

1.3.1. Direction Cosine Matrix

A Direction Cosine Matrix (DCM) $T_{B \leftarrow A}$ contains the cosines of the angles between the base vector[2] sets for the coordinate systems A ($\vec{x}_A$, $\vec{y}_A$ and $\vec{z}_A$) and B ($\vec{x}_B$, $\vec{y}_B$ and $\vec{z}_B$). The definition of a DCM is given in Equation (1.2). $T_{B \leftarrow A}$ allows to transform a vector given in system A ($\vec{v}_A$) into its representation in system B ($\vec{v}_B$) by following Equation (1.3). To obtain the reverse transformation $T_{A \leftarrow B}$, the original Matrix needs to be transposed (Großekatthöfer and Yoon, 2012).

$$T_{B \leftarrow A} = \begin{pmatrix} \cos\angle(\vec{x}_A, \vec{x}_B) & \cos\angle(\vec{y}_A, \vec{x}_B) & \cos\angle(\vec{z}_A, \vec{x}_B) \\ \cos\angle(\vec{x}_A, \vec{y}_B) & \cos\angle(\vec{y}_A, \vec{y}_B) & \cos\angle(\vec{z}_A, \vec{y}_B) \\ \cos\angle(\vec{x}_A, \vec{z}_B) & \cos\angle(\vec{y}_A, \vec{z}_B) & \cos\angle(\vec{z}_A, \vec{z}_B) \end{pmatrix} \tag{1.2}$$

$$\vec{v}_B = T_{B \leftarrow A} \cdot \vec{v}_A \tag{1.3}$$

[2]They are unit vectors

1.3.2. Euler Angles

The Euler angles describe the change in attitude of an object as a sequence of rotations around the three axes of the object's body (roll, pitch, yaw). The transformation from system A to B is calculated by the successive application of the matrices describing the rotation around each axis. The rotation angles for each axis θ_x, θ_y and θ_z are called Euler angles. Equation (1.4) provides the definition of the individual rotation matrices. For large angles the order of the rotation sequence is important, but for small angles the combined rotation matrix $R_{B\leftarrow A}$ can be written as in Equation (1.5). In order to transform a vector from system A ($\vec{v}_A$) into its representation in system B ($\vec{v}_B$) one needs to apply Equation (1.6) (Großekatthöfer and Yoon, 2012).

$$
\begin{aligned}
R^x(\theta_x) &= \begin{pmatrix} 1 & 0 & 0 \\ 0 & \cos(\theta_x) & \sin(\theta_x) \\ 0 & -\sin(\theta_x) & \cos(\theta_x) \end{pmatrix} \\
R^y(\theta_y) &= \begin{pmatrix} \cos(\theta_y) & 0 & -\sin(\theta_y) \\ 0 & 1 & 0 \\ \sin(\theta_y) & 0 & \cos(\theta_y) \end{pmatrix} \\
R^z(\theta_z) &= \begin{pmatrix} \cos(\theta_z) & \sin(\theta_z) & 0 \\ \sin(\theta_z) & \cos(\theta_z) & 0 \\ 0 & 0 & 1 \end{pmatrix}
\end{aligned} \tag{1.4}
$$

$$
R_{B\leftarrow A} = \begin{pmatrix} 1 & \theta_z & -\theta_x \\ -\theta_z & 1 & \theta_y \\ \theta_x & -\theta_x & 1 \end{pmatrix} \tag{1.5}
$$

$$
\vec{v}_B = R_{B\leftarrow A} \cdot \vec{v}_A \tag{1.6}
$$

1.3.3. Quaternion

Quaternions are a common way to describe the attitude of a spacecraft relative to a reference frame or to transform between different reference frames. The main advantages of quaternions over Euler angles are the lower computational cost and the absence of singularities (Großekatthöfer and Yoon, 2012).

Quaternion Definition

Quaternions describe the relative change in position via a single rotation of fitting angle around an appropriate rotation axis. A common definition for the normalized quaternion $\bar{q}$ is given in Equation (1.7), where θ is the rotation angle around the rotation axis $\hat{e}$. $\hat{e}$ is a unit vector. A quaternion $\bar{q}$ can be split into a scalar part q_0 and a vector part $\vec{q}$. The vector part $\vec{q}$ is a 3-D vector with components q_1, q_2 and q_3 (Großekatthöfer and Yoon, 2012; Yang, 2012).

$$\bar{q} = \begin{pmatrix} \cos\frac{\theta}{2} \\ \hat{e}\cdot\sin\frac{\theta}{2} \end{pmatrix} = \begin{pmatrix} q_0 \\ \vec{q} \end{pmatrix} = \begin{pmatrix} q_0 \\ q_1 \\ q_2 \\ q_3 \end{pmatrix} \tag{1.7}$$

Quaternion Multiplication

The multiplication of two quaternions $\bar{p}$ and $\bar{q}$ describes two consecutive rotations and is defined in Equation (1.8), where $\otimes$ is the quaternion multiplication and $\times$ the vector cross product (Großekatthöfer and Yoon, 2012; Yang, 2012).

$$\bar{p} \otimes \bar{q} = \begin{pmatrix} p_0 q_0 - \vec{p}\vec{q} \\ p_0\vec{q} + q_0\vec{p} + \vec{p} \times \vec{q} \end{pmatrix} \tag{1.8}$$

Quaternion Norm

The norm of a quaternion $||\bar{q}||$ is defined by Equation (1.9) (Großekatthöfer and Yoon, 2012; Yang, 2012).

$$||\bar{q}|| = \sqrt{q_0^2 + q_1^2 + q_2^2 + q_3^2} \tag{1.9}$$

Quaternion Complex Conjugate

The complex conjugate of a quaternion $\bar{q}^*$ is defined by Equation (1.10) (Großekatthöfer and Yoon, 2012; Yang, 2012).

$$\bar{q}^* = q_0 - \vec{q} = \begin{pmatrix} q_0 \\ -q_1 \\ -q_2 \\ -q_3 \end{pmatrix} \tag{1.10}$$

Quaternion Inverse

The inverse of a quaternion $\bar{q}^{-1}$ is defined by Equation (1.11) (Großekatthöfer and Yoon, 2012; Yang, 2012).

$$\bar{q}^{-1} = \frac{\bar{q}^*}{||\bar{q}||^2} \tag{1.11}$$

Minimum Angle Quaternion

Given two unit vectors $\hat{v}$ and $\hat{w}$, the quaternion $\bar{q}_{min}$ transforms $\hat{v}$ into $\hat{w}$ with the smallest angle possible. $\bar{q}_{min}$ can be calculated via Equation (1.12). The result obtained is normalized identical to the definition in Equation (1.7) (Yang, 2012).

$$\bar{q}_{min} = \frac{1}{\sqrt{2(1+\hat{v}\cdot\hat{w})}} \begin{pmatrix} 1+\hat{v}\cdot\hat{w} \\ \hat{v}\times\hat{w} \end{pmatrix} \tag{1.12}$$

Quaternion Change of Reference Frame

A vector $\vec{v}_A$ in reference frame A can be transformed into its equivalent $\vec{v}_B$ in reference frame B using the transform quaternion between the two reference frames $\bar{q}_{B\leftarrow A}$ following Equation (1.13). In order to perform the calculation, the vector $\vec{v}_A$ needs to be expanded into quaternion format by adding a scalar part of zero, so $\vec{v}_A$ becomes $\begin{pmatrix} 0 \\ \vec{v}_A \end{pmatrix}$ (Großekatthöfer and Yoon, 2012; Yang, 2012).

$$\vec{v}_B = \bar{q}_{B\leftarrow A} \otimes \vec{v}_A \otimes \bar{q}^*_{B\leftarrow A} \tag{1.13}$$

Transform Quaternion for Non-Normalized Vectors

For two non-normalized input vectors $\vec{a}$ and $\vec{b}$ the minimum angle quaternion $\bar{q}_{min}$ (see Equation (1.12)) can be calculated via Equation (1.14) (see A).

$$\begin{aligned} \vec{q} &= \vec{a}\times\vec{b} \\ q_0 &= ||\vec{a}||\cdot||\vec{b}|| + \vec{a}\cdot\vec{b} \\ \bar{q} &= \frac{1}{\sqrt{q_0^2+||\vec{q}||^2}} \begin{pmatrix} q_0 \\ \vec{q} \end{pmatrix} \end{aligned} \tag{1.14}$$

1.3.4. Conversion of Euler Angles to Quaternion

In order to convert a set of Euler angles θ_x, θ_y and θ_z into a quaternion $\bar{q}$ an intermediate step via a DCM can be used (Großekatthöfer and Yoon, 2012).

For small angles the DCM can be directly obtained from the Euler angles θ_x, θ_y, θ_z via Equation (1.5).

The transformation from DCM to the quaternion $\bar{q}$ is more complex. Using the diagonal components of the DCM T_{ii}, each of the quaternion's components $\bar{q}$ (q_0, q_1, q_2, q_3) could be calculated. In order to avoid precision issues due to small values, the largest of the initially calculated quaternion components should be used as a starting point. From there, all other components can be found by including the non-diagonal DCM entries. The following equations are for the cases where q_0 (1.15), q_1 (1.16), q_2 (1.17) and q_3 (1.18) is the largest initial component (Großekatthöfer and Yoon, 2012).

$$\bar{q} = \begin{pmatrix} q_0 \\ q_1 \\ q_2 \\ q_3 \end{pmatrix} = \begin{pmatrix} \sqrt{1/4 \cdot (1 + T_{11} + T_{22} + T_{33})} \\ (T_{32} - T_{23})/(4 \cdot q_0) \\ (T_{13} - T_{31})/(4 \cdot q_0) \\ (T_{21} - T_{12})/(4 \cdot q_0) \end{pmatrix} \tag{1.15}$$

$$\bar{q} = \begin{pmatrix} q_0 \\ q_1 \\ q_2 \\ q_3 \end{pmatrix} = \begin{pmatrix} (T_{32} - T_{23})/(4 \cdot q_1) \\ \sqrt{1/4 \cdot (1 + T_{11} - T_{22} - T_{33})} \\ (T_{21} + T_{12})/(4 \cdot q_1) \\ (T_{13} + T_{31})/(4 \cdot q_1) \end{pmatrix} \tag{1.16}$$

$$\bar{q} = \begin{pmatrix} q_0 \\ q_1 \\ q_2 \\ q_3 \end{pmatrix} = \begin{pmatrix} (T_{13} - T_{31})/(4 \cdot q_2) \\ (T_{21} + T_{12})/(4 \cdot q_2) \\ \sqrt{1/4 \cdot (1 - T_{11} + T_{22} - T_{33})} \\ (T_{32} + T_{23})/(4 \cdot q_2) \end{pmatrix} \tag{1.17}$$

$$\bar{q} = \begin{pmatrix} q_0 \\ q_1 \\ q_2 \\ q_3 \end{pmatrix} = \begin{pmatrix} (T_{21} - T_{12})/(4 \cdot q_3) \\ (T_{13} + T_{31})/(4 \cdot q_3) \\ (T_{32} + T_{23})/(4 \cdot q_3) \\ \sqrt{1/4 \cdot (1 - T_{11} - T_{22} + T_{33})} \end{pmatrix} \tag{1.18}$$

1.3.5. Across and Along Line of Sight

Two terms often used when describing spacecraft pointing and related movement are across and along Line of Sight. Across LoS refers to the plane perpendicular to the LoS. Along LoS refers to the same axis as the LoS.

1.4. The UVIE-FGS

The University of Vienna Flight Software Team is developing/has already developed a Fine Guidance System (FGS) for the ARIEL (Mösenlechner et al., 2021) and CHEOPS (Loeschl et al., 2016) missions (UVIE FGS). The ideas and lessons learned there give the starting point for the algorithms developed during this thesis.

The UVIE-FGS has two main components. First the Acquisition takes an image from the detector and locates the star(s) used by the second component, the Guiding, which then calculates the position(s) of the so-called guide star(s) to sub-pixel precision via a centroiding algorithm (Mösenlechner, 2021).

Both components are described in more detail in the following subsections.

1.4.1. Acquisition

The Acquisition is the first component of the UVIE-FGS. Starting with a detector image only, the Acquisition first extracts the location of visible sources (source extraction) and then determines which of those is/are the guide star(s) (target selection) (Mösenlechner, 2021; Löschl, 2018).

The source extraction of the ARIEL and CHEOPS FGS are based on SExtractor (Bertin and Arnouts, 1996). They function nearly identically (Mösenlechner, 2021; Löschl, 2018) and therefore will be described jointly in the section below. The target selection is fundamentally different for both missions thus will be described for CHEOPS and ARIEL separately.

Source Extraction

The source extraction of the ARIEL and CHEOPS FGS uses a peak finding method to locate stars on a frame. The approach is similar to how the tool SExtractor (Bertin and Arnouts, 1996) functions and was chosen due to the limited computational resources typically available on a satellite (Mösenlechner, 2021; Löschl, 2018).

The first step of the Acquisition is to bin the image (sum of the binned pixels) in order to reduce computation costs. Next, the brightest pixels within the binned image are located and stored as potential star candidates. Afterwards, the multiple pixels contributed by a single source are reduced to just one entry by grouping closeby candidate pixels (CHEOPS (Löschl, 2018)) or removing less bright neighbors (ARIEL (Mösenlechner, 2021)). The last step is the removal of cosmics. In the binned image, the 8 neighbors of each candidate are compared with a pre-calculated threshold. If sufficient neighbor pixels are above the threshold, a candidate is considered to be an extended source and kept as an extracted star (Mösenlechner, 2021; Löschl, 2018).

With this list of extracted stars available, the Acquisition then continues to search for the user-configured guide stars among them. This step is done differently in CHEOPS and ARIEL and will thus be described separately below.

Target Selection - CHEOPS

CHEOPS is equipped with two methods for target selection. First, the Angle Method which uses the stars' relative positions to each other. It is applied in more challenging cases. Second, the Magnitude Validation Acquisition Algorithm which considers the relative brightness of the stars. It is used for sparse regions and when the target's brightness limits the possible exposure time (too few stars for angle method)(Löschl, 2018).

Angle Method: The Angle Method is used for cases where the target star cannot be easily identified by its brightness alone. The basic procedure was developed by Liebe (1992) and later adapted for star trackers. The Angle Method considers one star called a base star and pairs of its neighbors called partner stars. The set of distances between the base and each partner star and the angle between them is called a fingerprint (Figure 1.8). On board the satellite, every star found within the region where the actual target is expected to be located is used as a base star to create a database of fingerprints with many different partner star pairs. For the actual target a database was pre-calculated on ground and uploaded to the satellite. On board the multiple databases are then compared with the uploaded one. The method then selects the star which best matches the reference and observed databases as the target after applying several correction and validation checks (Löschl, 2018).

Magnitude Validation Acquisition Algorithm: The Magnitude Validation Acquisition Algorithm is employed for cases where the target star can be identified by its unique brightness and cases where the exposure time is limited due to very bright sources inside the FoV, thus preventing extraction of sufficient stars for the Angle Method. This algorithm compares the signal of all stars within the region where the actual target is expected to be with a reference value and chooses the closest match as the target (Löschl, 2018).

Target Selection - ARIEL

The target selection for the Atmospheric Remote-sensing Infrared Exoplanet Large-survey (ARIEL) mission is simple. The signal of the extracted stars obtained during the neighbor pixel threshold check is compared with a user-defined value and the star closest to it is selected as the target/guide star (Mösenlechner, 2021).

1.4.2. Guiding

The Guiding is the second part of the UVIE-FGS. It takes the rough position of a guide star obtained during Acquisition and cuts out the area around it to obtain the so-called Region of Interest (ROI). All further calculations are limited to this region in order to speed up the process. Guiding performs a centroiding calculation on the ROI to obtain the

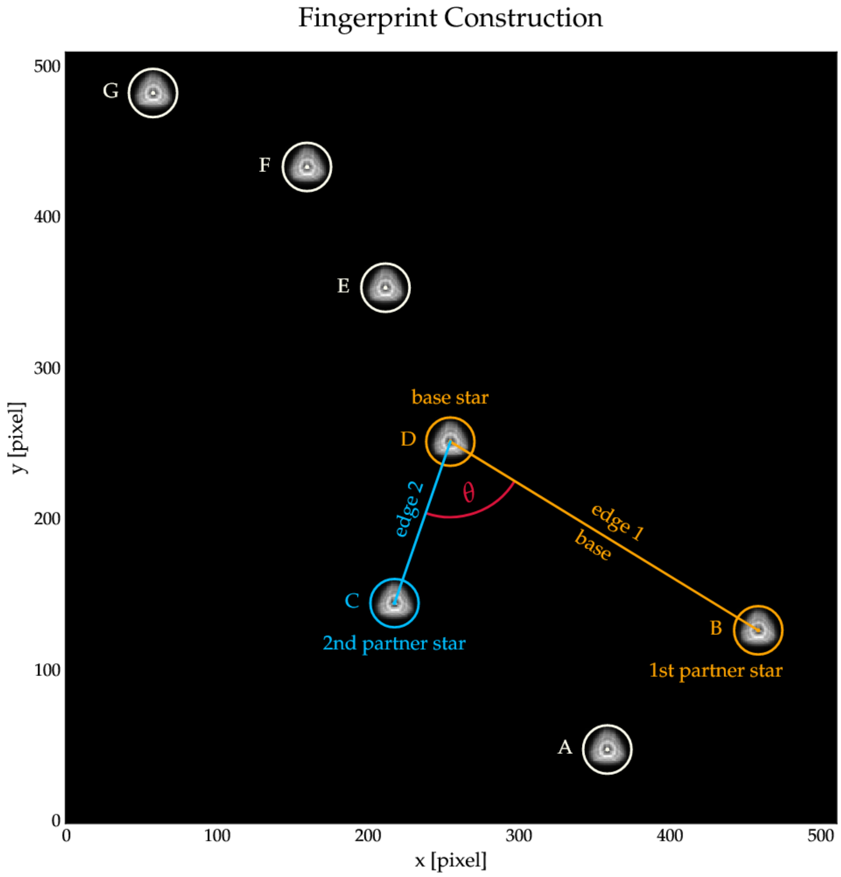

Figure 1.8.: A fingerprint used by the CHEOPS Angle method, with star D as the base star and stars C and B as the partner star pair. The length of edges one and two and the angle θ make up the fingerprint (Figure 2-2 Löschl, 2018)

star's position to sub-pixel precision and communicates this information to the satellite platform. The Guiding is active during the entire length of the exposure. For centroiding CHEOPS and ARIEL both employ algorithms from the Center of Gravity (CoG) family (Mösenlechner, 2021; Löschl, 2018). As the implementation developed for ARIEL will be re-used for ARRAKIHS, a detailed description of the ARIEL Guiding will be given below.

The Guiding operates on the original (not binned) version of the frame. It starts by obtaining a rough position of the star inside the ROI using Intensity Weighted Centroiding (IWC). The guess for the coordinates x_c and y_c is given in Equation (1.19), where N and M are the dimension of the ROI and $I_{i,j}$ is the intensity of the pixel at position (i, j) and x_i and y_i are the position relative to the corner of the ROI used as origin. The IWC method is preferred over the simpler Center of Gravity (CoG) one shown in Equation (1.20) (variables identical to IWC), because the precision of CoG is negatively influenced by background noise (Mösenlechner, 2021).

$$\text{IWC: } x_c = \frac{\sum_{i=0}^{N}\sum_{j=0}^{M} I_{i,j}^2 x_i}{\sum_{i=0}^{N}\sum_{j=0}^{M} I_{i,j}^2},\ y_c = \frac{\sum_{i=0}^{N}\sum_{j=0}^{M} I_{i,j}^2 y_i}{\sum_{i=0}^{N}\sum_{j=0}^{M} I_{i,j}^2} \tag{1.19}$$

$$\text{CoG: } x_c = \frac{\sum_{i=0}^{N}\sum_{j=0}^{M} I_{i,j} x_i}{\sum_{i=0}^{N}\sum_{j=0}^{M} I_{i,j}},\ y_c = \frac{\sum_{i=0}^{N}\sum_{j=0}^{M} I_{i,j} y_i}{\sum_{i=0}^{N}\sum_{j=0}^{M} I_{i,j}} \tag{1.20}$$

The rough position guess obtained using IWC is then iteratively refined via Iteratively Weighted Center of Gravity (IWCoG) calculations. Equation (1.21) gives the formula for IWCoG, where $W_{i,j}$ is a location specific weight function and all other variables are as in Equation (1.19). The values of $W_{i,j}$ are obtained by centering a 2D Gaussian which mimics the shape of the PSF on the rough location from IWC or the one from the previous IWCoG iterations (Mösenlechner, 2021).[3]

$$\text{IWCoG: } x_c = \frac{\sum_{i=0}^{N}\sum_{j=0}^{M} I_{i,j} W_{i,j} x_i}{\sum_{i=0}^{N}\sum_{j=0}^{M} I_{i,j} W_{i,j}},\ y_c = \frac{\sum_{i=0}^{N}\sum_{j=0}^{M} I_{i,j} W_{i,j} y_i}{\sum_{i=0}^{N}\sum_{j=0}^{M} I_{i,j} W_{i,j}} \tag{1.21}$$

Guiding's last step is the validation of the obtained centroids. The implementation for ARIEL builds on the one from CHEOPS (Mösenlechner, 2021) and is also used in this thesis as the starting point for ARRAKIHS. Therefore, the ARIEL version will be described in the following.

The ARIEL centroid validation works by checking the centroid and its ROI against five rules (Mösenlechner, 2021; Mösenlechner et al., 2024):

1. Image not constant (minimum $\neq$ maximum)
2. Image contains star (mean $>$ median)

[3] As described in Mösenlechner (2021) the initial implementation for ARIEL contemplated using a linear approximation of the PSF as a second option for the weight function. This feature was dropped during development (Mösenlechner et al., 2024)

3. Star is distinct/sharp feature ([median + 2 sigma] $<$ maximum)
4. There is a signal ([maximum $-$ minimum] $>$ Signal Limit)
5. The Pearson correlation coefficient between signal and model PSF is large ($\text{pearson}_x \cdot \text{pearson}_y >$ Pearson Limit)

The first four rules are applied to the binned image, while the last one is applied to the original one. The obtained Pearson correlation coefficient is also used as a quality indicator for the centroid (Mösenlechner, 2021; Mösenlechner et al., 2024).

In summary,

> the UVIE-FGS consists of the Acquisition, which extracts stars and identifies the target/guide star(s), and the Guiding, which uses an algorithm from the CoG family to obtain stellar position to sub-pixel precision.

2. ARRAKIHS Simulator

In order to test and verify the functionality of the algorithms developed as part of this thesis, mock ARRAKIHS observations are required. To produce these images, the Datasim v2 (DaSi2) simulator developed by Gerald Mösenlechner for the development of the ARIEL FGS (Mösenlechner, 2024b) was used as a starting point and then modified to fit the properties of ARRAKIHS.

2.1. ARIEL Simulator

The Datasim v2 simulator generates images in four steps. First, the so-called starmask is generated. Based on an XML file, containing the positions and brightnesses of stars around a reference LoS, and a pointing offset from the reference the simulator determines the pixel positions the stars would have on the detector and adds the star signals to the corresponding locations in the starmask. Next, a modified PSF is calculated by convolving the PSF with a linear smear kernel representing the satellite's large scale movement and optionally a second kernel representing small jitter movements. Third, the starmask is convolved with the modified PSF to produce the signal contributed by the stars. Lastly, various effects like background signal, shot noise, bias, dark current, cosmics and readout noise are added to produce the finished image, which is saved as a FITS file (Mösenlechner, 2024b).

As part of Mösenlechner (2026) real JWST images are compared to those produced by a simulator, whose detector effect implementation is also based on Datasim v2. The analysis confirms the correct functionality of the different detector effects. As an example, Figure 2.1 shows the histogram comparison of 100 averaged dark frames. Since the ARRAKIHS simulator developed as part of this thesis shares the detector effect implementation with the simulator from Mösenlechner (2026) (with the exception of hot-pixels), the analysis by Mösenlechner (2026) also verifies the correct functionality of the detector effects for this thesis.

2.1.1. Limitations from the Perspective of ARRAKIHS

The Datasim v2 simulator cannot produce images for testing the ARRAKIHS FGS algorithms, due to several limitations and "missing" features. The primary issue is the use of a single smear and jitter kernel for the whole FoV. This was not an issue for ARIEL, as the FGS there has its own channels with small detector size and fast readout Mösenlechner et al. (2024). For ARRAKIHS, the FGS uses the same 2048 × 2048 px detector with

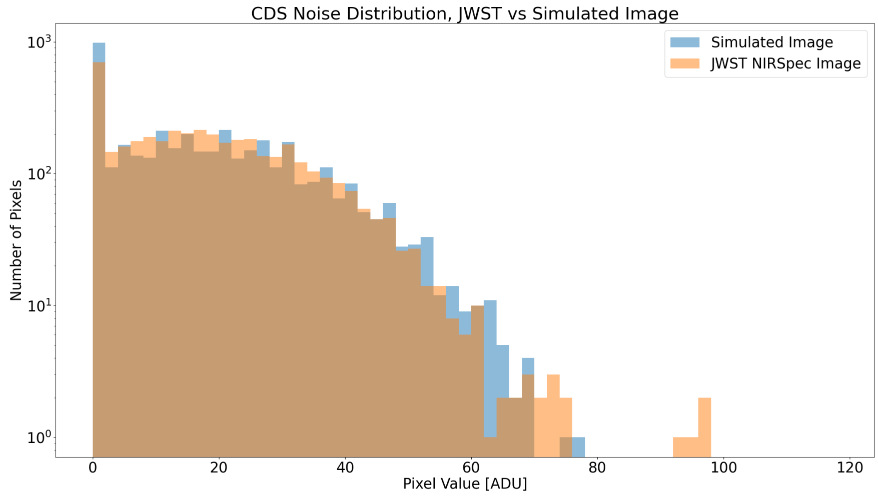

Figure 2.1.: Comparison of 100 averaged dark frames between the ARIEL simulator and JWST images

~ 1.45 s readout time as the science. Due to the larger detector size, there are significant differences between locations on the detector when it comes to the smearing of a star's signal over multiple pixel caused by the satellite's rotation along the LoS. In some cases, this could cause the combined across and along LoS movement to cancel out for some stars, while producing twice the effect for others. This is demonstrated in Figure 2.2. The long readout time of the ARRAKIHS detectors causes each location on the CCD to sample a different part of the satellite's movement history. Therefore, the use of a single smear kernel makes it impossible to reproduce scenarios where the movement rates change over time. This is especially problematic when looking at jitter movements, since those can vary on similar or even shorter time scales than the readout. Another limitation of the Datasim v2 simulator is, that it does not simulate the up-the-ramp sampling performed by the detector. This was resolved in a later developed spin off version of the simulator, the so-called HFS (Mösenlechner, 2024a). The implementation of the ramp used for this thesis is based on the HFS version.

2.2. Required Features

In light of the characteristics of the ARRAKIHS detector, the required features for the ARRAKIHS simulator considered in this thesis are:

- Mock images for actual ARRAKIHS targets
- Output Full Frame series with continuous stellar movement
- Simulated stellar movement consistent with readout time difference and changes in satellite movement rate over time

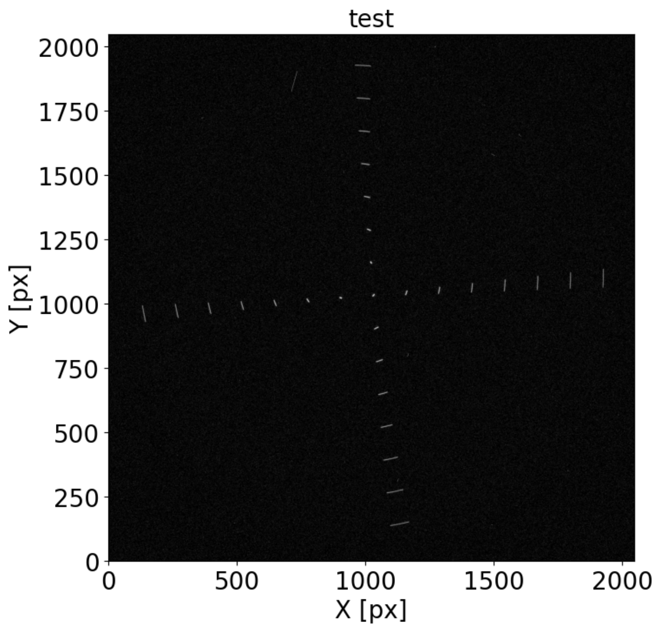

Figure 2.2.: ARRAKIHS Simulator image demonstrating location dependent movement smear due to large detector size and long readout time. The smear due to rotation is dependent on the distance from the detector center. The across and along LoS movement combines differently at every location, as demonstrated when comparing the stars above and below the rotation axis. The different readout times cause the originally plus shaped star distribution to become slanted to the right.

- Location dependent rotation effects
- Detector effects like DC, RN, photon noise, ...
- Up-the-ramp sampling with pixel saturation

Combining the available and "missing" functionality and keeping the new requirements in mind,

> the ARIEL simulator's implementation of nearly all detector features is suitable for ARRAKIHS, but the calculations for the smearing caused by movement of the stars needs to become time and location dependent.

2.3. Implemented Version

In the following, the image generation steps for the developed ARRAKIHS simulator are described. They can be split into two main parts. First, the production of the XML file containing the star positions and brightnesses for the surrounding sky of a given target.

Second, the calculation of the image series.

The various parameters like Dark Current (DC), Readout Noise (RN) and background signal required for the generation of the images are taken from Consortium (2024). Consortium (2024) has a security classification of *ARRAKIHS Consortium only*, therefore the actual values used cannot be reported as part of this thesis.

2.3.1. XML File Production

The production of the XML files is the first step in the image generation process. For each of the 240 galaxies that are part of the ARRAKIHS target pool (Consortium, 2025), one XML file is created per channel (NIR-1 and NIR-2) containing the pixel positions on the ARRAKIHS detector relative to the galaxy and the brightness in photons per second. Since the data in the XML files is independent of the setup for the different mock observations, the files need to be created only once.

The raw data used to generate the XML files is downloaded from the GSC version 3.1 using the API provided (McLean, 2024). For each of the galaxies a cone search centered on the galaxy with a radius of 1.3° is performed[1] and saved as a CSV file.

The next step is to calculate the photon flux of each star for the ARRAKIHS NIR-1 and NIR-2 channels. The dataset contains H and J band magnitudes from 2MASS. They are used due to their proximity in wavelength to the ARRAKIHS NIR-1 and NIR-2 channels. Using the Vega photon flux values $\mathrm{F}_{\mathrm{ref}}$ from Paul Martini and rearranging the standard magnitude definition (Equation 2.1, (Weigert et al., 2009, page 43)) into Equation 2.2, the flux of the stars F_1 in the desired band can be calculated from the known magnitude m_1 making use of the fact that the magnitude of Vega m_{ref} is zero by definition (Weigert et al., 2009, page 43). The flux in NIR-1 and NIR-2 are calculated by combining the contributions from the H and J band using 1450 nm as the switch-over point[2]. The contributed flux is then multiplied with the combined throughput and detector response curve of ARRAKIHS[3] and the effective aperture area of the telescope to obtain the finished photons per second.

$$m_1 - m_{\mathrm{ref}} = -2.5 \cdot \log_{10}\left(\frac{F_1}{F_{\mathrm{ref}}}\right) \tag{2.1}$$

$$F_1 = \mathrm{F}_{\mathrm{ref}} \cdot 10^{\frac{m_{\mathrm{ref}} - m_1}{2.5}} \tag{2.2}$$

[1] The diameter of the FoV of each channel is 1.3° (Guzmán, 2022). Therefore, the radius chosen allows for offsets of the satellite pointing by up to 1024 px on each side without reaching the edge of the data.

[2] The 1450 nm as switch-over are based on the filter curves from Rodrigo (2025)

[3] Cannot be shown in this thesis, the information is classified to consortium internal

The last step is to calculate the pixel positions of each star on the detector relative to the galaxy. First, the right ascension and declination of the galaxy and the surrounding stars α_i and δ_i is converted into 3-D unit vectors $\vec{a_i}$ via Equation (2.3). Then, the quaternion $\bar{q}$ which transforms the galaxy position into $\vec{b} = (0, 0, 1)$ (z-axis unit vector) is calculated following Equation (1.14). After calculating the inverse $\bar{q}^{-1}$, Equation (1.13) is applied to transform the vectors of the stars, too. The x and y components of $\vec{a_i}$ under the small angle approximation now directly provide the angle offset from the galaxy for each star. The angles are converted to pixel offsets via the plate scale.

$$\vec{a_i} = \begin{pmatrix} \cos(\delta_i) \cdot \cos(\alpha_i) \\ \cos(\delta_i) \cdot \sin(\alpha_i) \\ \sin(\delta_i) \end{pmatrix} \tag{2.3}$$

The calculated pixel positions and the previously found brightnesses for each star are then written to the XML file for later use.

In short,

> the input data for the ARRAKIHS simulator is based on the GSC version 3.1 and stored as one XML file per galaxy.

2.3.2. Image Series Calculation

With the XML file of the desired target available, the ARRAKIHS simulator can produce an image series. Each series contains a raw and subsequent differential FFs. This reproduces the behavior after a detector reset, where the first Full Frame (FF) has to be used directly and all following FFs have the previous one subtracted from them to produce differential FFs. Differential frames have better noise characteristics. The image series calculation can be split into two main steps, the setup with ramp reset and the up-the-ramp sampling.

Setup with Ramp Reset

The first part of the mock observation is the setup, which handles the initial position and movement of the stars. The stars' positions are loaded from the XML file and shifted (pitch and yaw) and rotated (roll) to reproduce the initial LoS orientation at the beginning of the first FF readout.

Next, the movement history of the satellite is generated. During the up-the-ramp sampling part, the movement of the stars over a FF readout is performed in many small steps. The history contains the shift movement (pitch and yaw), the rotation angle (roll) and the shift offset caused by jitter for each of those steps. Up to now, only histories with constant angular rates for all 3 axes (yaw, pitch, roll) and a simple single frequency sine jitter are used. Since the history is generated prior to the sampling, it will be possible to load movement histories with more complex behavior in the future.

The penultimate part of the setup is the calculation of the FoV mask, the flat and the hot pixel map. The FoV mask has a value of one inside a given radius around the image center and is zero otherwise. The flat has a mean value and an associated flat-field precision. Additionally, if the image calculation is performed with active oversampling, a subpixel-flat can be included to represent the pixel internal response. The hot pixel map represents the location and mean signal of hot pixels by storing the signals to be added to the DC during the up-the-ramp sampling after a Poisson distribution has been applied to them.

The last step of the setup is the initialization of the detector ramp by simulating a detector reset. This is done via a normal distribution with the user provided bias level as mean and the reset noise as standard deviation.

Up-the-Ramp Sampling

The second step of the image generation is the up-the-ramp sampling. This step is repeated for every FF readout simulated (normally 3). It can be split into four main parts. First the calculation of the incoming signal from the stars, second the application of detector effects, third the update of the ramp and fourth the finalization of the new image.

The calculation of the incoming stellar signal is done similar to the ARIEL simulator by the use of a star mask. In contrast to the Datasim v2 simulator, the pixel position of a star is not determined just once per FF readout, but the readout period is split into many small steps and the position is determined for each. To obtain the positions of the stars at every step, the movement history is used to calculate the trajectories of the stars across the detector for the whole FF readout. If a star is located inside the edges of the detector and below the row currently being read out, an appropriate fraction of its signal is added to the star mask at the star's current location. As sketched in Figure 2.3, depending on the star's location on the detector, a part of its trajectory is only relevant for the star mask of the next FF. Therefore, the trajectories from the current FF are stored for the calculation of the next FF. Additionally, with the exception of the first FF (no past trajectories relevant due to the detector reset), the calculation of the star mask starts by looking at the previous trajectories and adding the signal if the star has been inside the edges of the detector and above the readout row. The finished star mask is convolved with the PSF to obtain the star image for the current FF.

With the finished star image available, the various detector effects are applied. First, a constant background signal is added to obtain the total incoming photons per pixel. Then, the Poisson noise is applied to the combined signal. Afterwards, the signal is multiplied by the FoV mask to restrict it to the actually illuminated part of the detector. Following that, the signal is multiplied by the flat. Using the detector's quantum efficiency, the signal is converted from photons into electrons. The next step is the addition of the Poisson distributed DC. If the image has been calculated with oversampling up to this

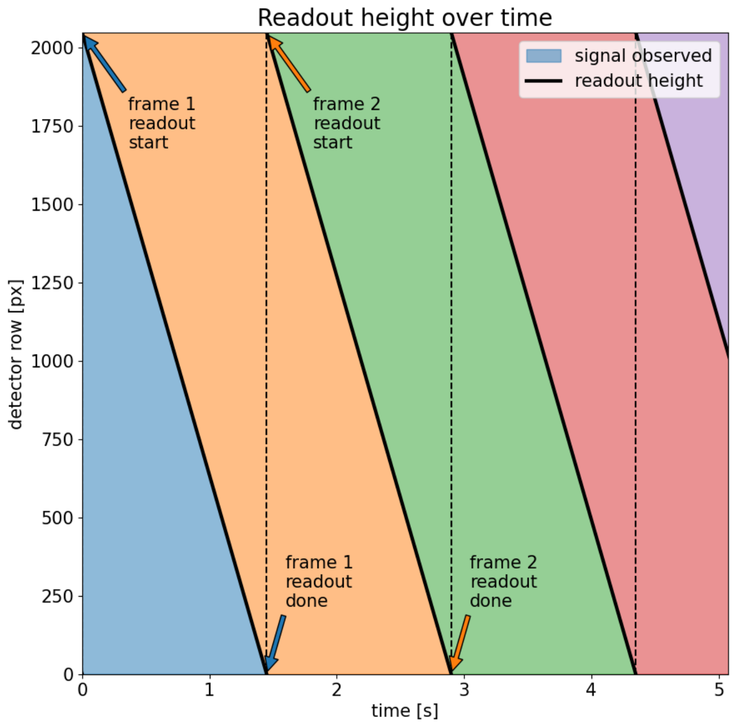

Figure 2.3.: Vertical position of the detector row being readout over time. This demonstrates how every row probes a different slice of the satellite's movement history.

point, it is now down-sampled to the final size. In addition to this, the image is converted into integer values (no partial electrons). Lastly, the electrons contributed by cosmics are added. This is done by simulating particles hitting the detector at various angles and with different energies. The functions used for this are the same as those used during development for the ARIEL mission (Mösenlechner and Ottensamer, 2024). In order to ensure that the algorithms developed during this thesis are capable of handling worst case conditions, the number of cosmics is boosted by five times. The same approach is also used for ARIEL testing (Mösenlechner and Ottensamer, 2024).

The third part is the updating of the ramp. The total electron signal calculated above is added to the ramp. If a pixel thus exceeds the FWC, it is set to the value of the FWC.

The last part is the generation of the read out image. A normally distributed readout noise is added to the updated ramp values. The electrons are converted into ADU via the system's gain. ARRAKIHS uses 16-bit unsigned integers for its images (team members, 2025), therefore any values above $2^{16} - 1 = 65535$ are limited to this number. Due to the improved noise properties, the ARRAKIHS algorithms will operate on differential images whenever possible (team members, 2025). Therefore, with the exception of the first FF, the previous image is subtracted from the newly produced one to obtain the new differential image. For a differential image negative values are set to zero, because ARRAKIHS uses 16-bit unsigned integers. The obtained (differential) image is stored as a FITS file.

Figure 2.4 demonstrates the effects of the different sampling times and location dependent rotation. The stars are distributed like a plus sign and a drift motion towards positive x, a counter-clockwise rotation and a jitter in y direction are applied. When comparing the trail of stars at the top of the image with those from the bottom, one can see the different sections of the sine-jitter experienced by the stars. For the top half the rotation partially counter-acts the drift thus reducing the overall length of the trails and on the right side the rotation cancels out (some) of the movement caused by the jitter.

To give an overview, the image series generation steps are summarized below:

1. adjust star positions to initial orientation
2. calculate movement history
3. generate FoV mask, flat and hot pixels
4. ramp reset
5. calculate star image + background
6. apply Poisson noise, flat and FoV mask
7. convert to electrons (integer casting)

8. add Dark Current (DC)
9. simulate and add cosmics
10. update ramp
11. limit to FWC
12. generate readout noise
13. produce new frame (ramp + readout noise)
14. limit to 16-bit ADU range
15. (calculate differential frame from new and previous one)
16. store new image
17. repeat steps 5-16 until image sequence is complete

With the described generation steps,

the ARRAKIHS simulator reproduces the up-the-ramp sampling performed by the real detector and accounts for the individual location and time dependent movement of the stars.

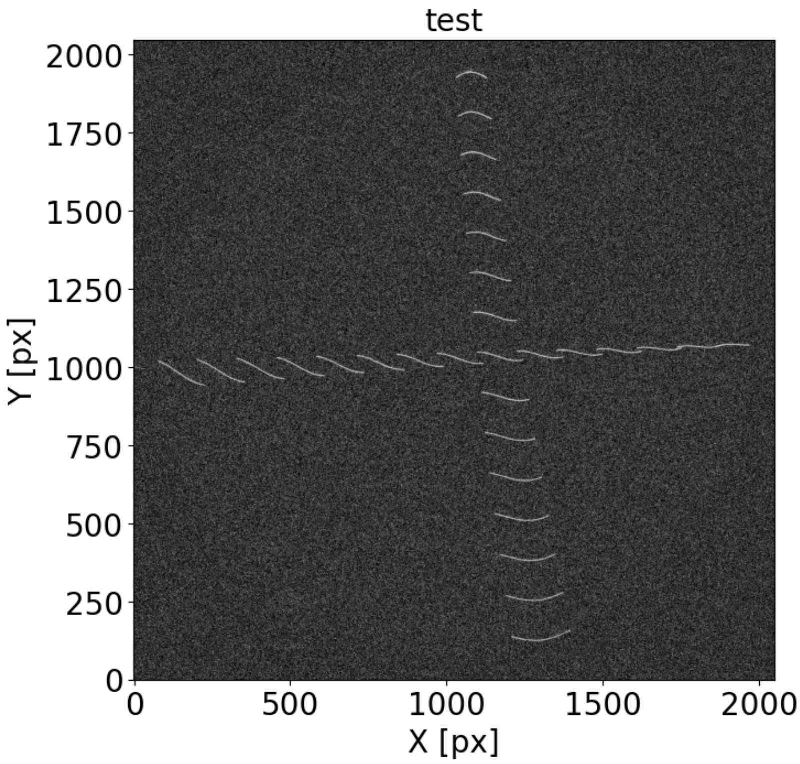

Figure 2.4.: ARRAKIHS simulator differential frame for a plus sign shaped distribution of stars with drift towards positive x, counter-clockwise rotation and jitter in y direction demonstrating the effects of readout time differences and location dependent movement of the stars.

3. Algorithm Design

In this chapter, the algorithms designed as part of this thesis will be explained in detail.

3.1. Requirements

This section provides an overview of the requirements for ARRAKIHS applicable to the algorithms developed in this thesis. The requirements are not taken verbatim from ARRAKIHS Project Team (2024a), ARRAKIHS Project Team (2024b) and Granabetter and Zoufal (2025), but are summarized below:

- **Exposure duration:** The exposures shall be 10 min long.
- **NIR channel synchronization:** It shall be possible to operate the two NIR channels (NIR-1 and NIR-2) synchronously (frame period).
- **Configurability:** Parameters controlling the instrument processing shall be configurable.
- **FGS Task:** The FGS shall provide AOCS information packets to the platform containing the pointing error relative to a reference obtained during Acquisition.
- **3-axis FGS:** The AOCS information provided by the FGS shall contain all 3 axes (roll, pitch, yaw).
- **AOCS information latency:** The AOCS information shall be transmitted to the platform with a maximum latency of 2 s.
- **AOCS information across LoS error:** The AOCS information across LoS error shall be less than 300 mas with 99.7% probability (3σ)
- **AOCS information along LoS error:** The AOCS information along LoS error shall be less than 30 arcsec with 99.7% probability (3σ)
- **Acquisition tasks:** The Acquisition procedure shall be able to autonomously extract and select suitable guide stars, calculate their centroids and provide an AOCS information packet to the platform.
- **Acquisition FoV:** The Acquisition algorithms shall support a FoV with diameter greater than 1.2°.

3.2. Acquisition

3.2.1. Overview

The task of the Acquisition algorithm is to determine the locations of the guiding windows containing the best guide stars possible. The guide stars are utilized later by the Guiding algorithm to inform the platform of deviations in pointing relative to the initial pointing during Acquisition. The Acquisition algorithm consists of six main parts. First, the search area definition that takes the first Full Frame (FF) (not differential) and identifies areas too bright to be included in the second step, i.e. the source extraction that takes the first differential FF and finds guide star candidates. Third, for each guide star candidate, a quality is calculated and its centroids are checked for validity in both differential FFs. If a centroid does not pass as valid, the candidate is removed. Fourth, the guiding window reset slot assignment is determined, where the candidates with the best quality are preferentially selected as guide stars. Fifth, the first AOCS information is calculated by combining the centroids of the guide stars chosen. Lastly, a quality parameter for the whole Acquisition is computed.

All steps of the Acquisition algorithm are described in detail below. The general method flow-down is as follows:

1. Define bright pixel search area
2. Find and sort the brightest pixels
3. Remove direct neighbors
4. Remove stars outside of candidate search area
5. Remove cosmics via neighbor pixel checks
6. Get brightness
7. Remove stars in danger of saturation
8. Look for other sources in potential guiding window and remove candidate if neighbors are too bright
9. Calculate guide star quality q_{gs}
10. Sort candidates based on q_{gs}
11. Confirm centroid validity for both differential images
12. Determine guiding window reset slot assignment
13. Place guiding windows around guide stars
14. Calculate AOCS information from centroids
15. Calculate Acquisition quality

3.2.2. Search Area Definition

To reduce the computation time and resources needed for the following source extraction step (see below) the area to be searched (search area) is limited to the FoV on the detector and excludes the region around features (stars) that are so bright as to saturate before the end of the third FF readout.

For the FoV limitation, the pixel positions per row corresponding to the left and right edge of a circle centered on the detector with a radius of `exclusion buffer` px larger than the outer edge of the guide star candidate area (see below) are computed. The position of the edges allow the source extraction to skip from the right FoV edge of a row to the left FoV edge of the following row.

Additionally, the first FF (not differential) is checked for features (stars) possessing signals higher than 1/3 of the ADU integer limit (1/3 of the FWC). These features need to be excluded for two reasons. First, since there are no detector resets during the Acquisition as the guiding window reset slot assignment is only defined after the third FF is read out. Therefore, if they are stars, their centroids and brightnesses would not be correctly calculable (signal no longer represents PSF). Second, since these features are the brightest objects in the FoV, they would take up a large portion of the brightest pixels used initially during source extraction (see below). Thus, the features and a small region around them need to be excluded from the source extraction. The size of the excluded region is user-defined (`exclusion buffer`). The too bright features are found by passing row by row once through the first FF and noting blocks of at least n (`exclusion min size`, user-defined) pixel that are above the 1/3 ADU limit threshold. If a new block is found with its central position inside the extent of a previously unfinished block, the new block is considered an extension to the previously found one. At the end of a row, each block that did not get an addition is considered a finished region. The extent of the regions found get expanded by n pixels (`exclusion buffer`, user-defined) to exclude further bright pixels from the same source. The pixel positions of the regions' borders are sorted by the order they are encountered in when passing through the image. This allows the source extraction to skip all pixels inside the exclusion regions in the same manner as the FoV edges.

In summary, the purpose of the Search Area Definition is,

> to reduce computation time in the following source extraction step by identifying and excluding the regions outside the FoV and around too bright features.

3.2.3. Source Extraction

The source extraction used here is loosely based on SExtractor (Bertin and Arnouts, 1996) and has previously been used in other missions like CHEOPS and ARIEL. It is employed on the first differential FF obtained for Acquisition.

The first step of the source extraction is generating a sorted list of the $\mathtt{N_{target}}$ brightest pixels within the search area configured (see above). The algorithm passes through the image once and only considers a pixel if it is a local maximum within its row and the pixel at the same position in the previous row is fainter. The sorted pixels are then considered star candidates. Next, all the less bright pixels up to 3 px around a candidate are removed as candidates under the assumption that they belong to the same source. Additionally, all candidates outside the candidate area (see below) are removed. The next step is the removal of (most) cosmics, which are contaminating the star candidate list. The removal is done by analyzing the 8 direct neighbor pixels of a candidate and applying two criteria. First, 4 neighbor pixels need to be a user-defined level ($\boldsymbol{\sigma}$) above the average image background. This removes most single pixel cosmics, since the neighbor pixels do not have any signal and are thus at the level of the background. Second, the slope (brightness fraction) between the central and the neighbor pixels is checked. If 5 or more pixels have a slope greater than 100, the candidate is considered a cosmic. This criterion removes multi pixel cosmics due to their sharpness as compared to the signal of an actual star. The second criterion is necessary, because many multi pixel cosmics manage to pass the first one. Lastly, sources in danger of saturating are removed by comparing the sum of the central and neighboring pixels with a reference value for a saturating source and rejecting the candidate if its signal is higher.

The remaining candidates are concluded to be stars and their guide star quality q_{gs} is calculated, as described below.

The shape of the area where star candidates are considered (candidate area) can be configured in one of four ways. All options share a circular outer boundary, normally configured a few pixels inside the FoV edge. First, `all` the area inside the outer boundary is used. Second, a `circular` inner boundary is defined and only the annulus inbetween is considered. Third, a `box` is excluded around the image center. Fourth, only an `u-shaped` region is considered. The placement of all the boundaries is user-configurable, including the orientation of the u-shaped region, the centers of the inner annulus boundary and even the center of the outer circular boundary. Examples are shown in Figure 3.1.

In short,

> sources are extracted from the two differential frames used by the Acquisition within the user defined candidate area via a peek finding algorithm including a temporal validation step to further remove contamination by cosmics.

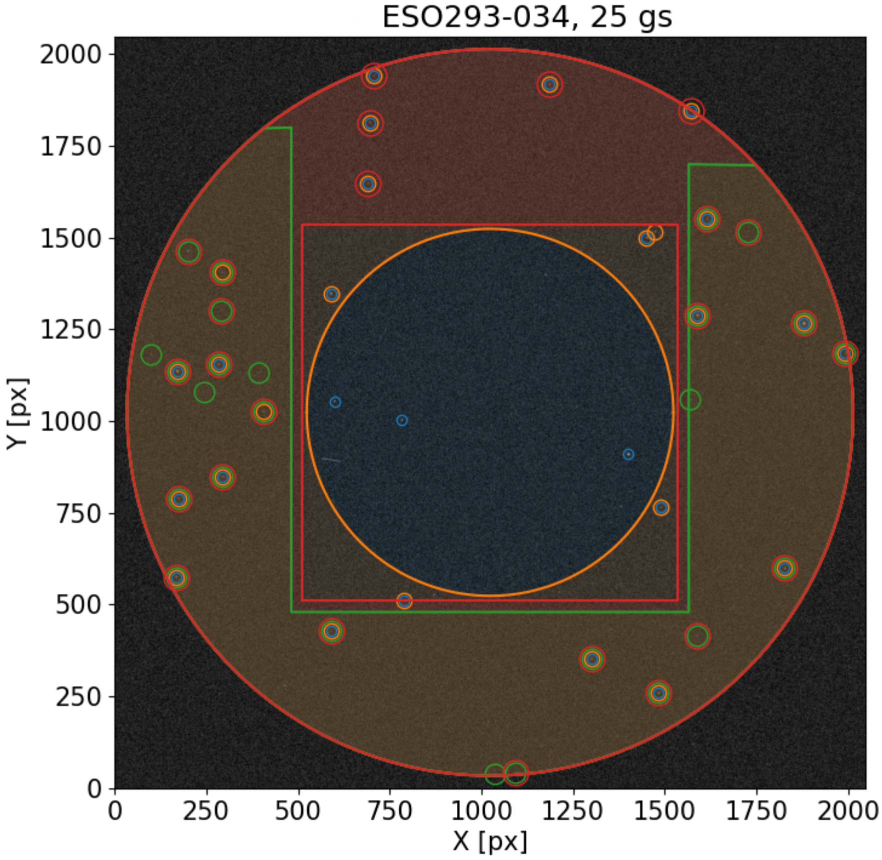

Figure 3.1.: Example for the different possible area shapes and how this influences guide star selections. All options share the outer circular boundary. The different configurations are colored as follows: `all` in blue, `circular` in orange, `box` in red and `u-shaped` in green. Selected guide stars are marked with a colored ring corresponding to the area shape used when they were selected.

3.2.4. Guide Star Selection

In order to determine the quality for use as a guide star (guide star quality) for each of the candidate stars found, several properties are determined and then combined to the final quality parameter q_{gs}.

The first value considered is the brightness, which is already known from the source extraction. The brightness quality parameter q_b is calculated as follows:

$$q_b = \frac{\log_{10}(\text{brightness})}{\log_{10}(\text{max brightness})}$$

where max brightness refers to the reference value for a saturating source (`maximum signal`) already used during source extraction (see above). The logarithm is used to prevent q_b from completely dominating over the other components.

Second, an additional source extraction is performed on an area centered on, but larger than, the area that would become the guiding window if the candidate star were selected. The extraction works identically as described above. If any additional sources are found, their relative brightness and distance to the guide star candidate is determined. The candidate is discarded, if a source of equal or greater brightness is located inside the extended area or a source with half or more brightness is found inside the potential ROI. These two criteria are included to prevent cases where the IWC step (part of the centroiding algorithm, see below) could jump to a different star. The neighbor quality component q_n is the mean relative brightness weighted distance to the star candidate normalized to the size of the extended area considered. If no neighbor stars are found, q_n is set to 1.

Third, the position of the guide star on the detector is considered. The position quality component q_p is calculated via a piecewise linear function. q_p is equal to 1 for the bottom $q_{p,\text{start}}$ rows of the detector, then decreases linearly until reaching a value of $q_{p,\text{min}}$ at row $q_{p,\text{stop}}$ and is equal to $q_{p,\text{min}}$ for all rows between $q_{p,\text{stop}}$ and the top detector edge.

The components described above are combined to the guide star quality q_{gs} following Equation 3.1, where the weights w_x are user configurable. The guide star candidates are sorted based on their quality.

$$q_{gs} = \frac{q_b \cdot w_b + q_n \cdot w_n + q_p \cdot w_p}{w_b + w_n + w_p} \tag{3.1}$$

Lastly, the centroiding algorithm and its validation are executed on the area to become the guiding window for both differential images. The candidate is rejected, if the validation fails for either of the images. This validation step serves two main functions. First, to remove candidates that have an incorrect light distribution to be an isolated point source, e.g., two optically very close stars or a faint star in the flank of a very bright source.

Second, to eliminate the remaining contamination due to cosmics by serving as a temporal filter (verifies found feature is persistent). From the remaining candidates the guiding window reset slot assignment is determined by the strategy described below, where the best quality candidates up to the desired number of guide stars are preferentially selected and the guiding window location and reset properties are finalized. The guiding algorithm then takes over and uses the already calculated centroids to produce the first AOCS information.

An example of how the shape of the guide star candidate area affects the selection process can be seen in Figure 3.1. The Acquisition algorithm was instructed to find a maximum of 25 guide stars. Especially for the "u-shaped" configuration (because its total area is smaller) the algorithm had to select stars that were ignored by the other configurations, as they managed to find sufficient other guide stars with higher quality.

The most important point is,

the guide star quality parameter combines brightness, position and distance to neighboring stars.

3.2.5. Guiding Window Reset Slot Assignment Strategy

When a guide star saturates, its signal no longer represents the expected shape of the PSF. As a result, the precision of its centroid decreases sharply. Therefore, the guiding windows of guide stars with saturation times shorter than the 10 minutes exposure time need to be reset as often as necessary to prevent saturation.

The H2RG detector is capable of resetting individual guiding windows, but at the time of writing the level of configurability and setup procedure is not yet defined. As such the Guiding Window Reset Slot Assignment Strategy is designed under the following assumptions. Each window is reset periodically with a individual period and phase measured in FF readout cycles[1]. However, there needs to be an upper limit of window resets per FF readout (`reset budget`), in order to keep the overall FF readout synchronized between both NIR detectors to prevent image artifacts due to varying current inside the readout electronics[2]. Resetting fewer windows in a given cycle is possible without affecting the timing, since there is a fixed delay between the end of the previous and the start of the following readout cycle.

Therefore, the task of the guiding window reset slot assignment strategy algorithm is to select guide stars and their window reset properties from the remaining guide star candidates so that the quality of the guide stars is maximized, while the number of resets per cycle does not exceed the fixed upper limit (during any cycle that is part of the 10-minute exposure).

[1]The phase is incremented at every readout and if it becomes equal to the period, the window is reset after the end of the current FF readout.

[2]The user is responsible for correct configuration in order to stay within the limit

An additional point that is handled as part of the strategy is the prevention of overlapping guiding windows. This would be problematic, because the satellite's movement could cause multiple guide stars to appear in the same window, thus causing the IWC step (see below) to be drawn in the direction of the additional stars. Furthermore, the reset of one of the windows would result in exposure time differences between the pixels of the overlapping window. In the worst case, this could cut away a part of the PSF. To prevent the overlapping, the positions of the remaining guide star candidates are compared. If the distance for both detector axes is smaller than the ROI size plus a user-configurable buffer (`overlap buffer`), the two stars are considered to overlap. All the overlaps are stored for later use.

The guiding window reset slot assignment algorithm starts with calculating the maximum number of cycles until a candidate requires a reset, based on the brightness used for the quality calculation described above. It sets up an initially empty schedule for the whole duration of the exposure. The schedule has as many rows as there will be FF readouts during the exposure and as many columns as the maximum number of allowed resets per cycle (`reset budget`). All stars with saturation times longer than exposure time are assigned a period equal to their theoretical maximum and a phase of zero, thus, they will never be reset during the exposure. Then, the star with the highest quality q_{gs} is assigned slots in the schedule with the maximum period and phase needed to prevent saturation. If there are other candidates that overlap with this one, they are marked as blocked and will not be considered in further steps. Next, the algorithm attempts to fit the remaining next-highest quality star into the schedule with its maximum period and phase, by checking if there still are slots available for every cycle where the star is planned to be reset. If it is not possible to use the maximum phase, because all slots in at least one cycle are already used up, consecutively shorter phases are attempted. If this does not work either, the period is shortened. If it turns out to be impossible to fit a star, it is skipped and excluded as a candidate. The algorithm continues assigning stars and blocking overlapping ones until no more stars can be assigned. Should the number of assigned stars be less than the number of desired guide stars and the number of initially available candidates be larger than the desired amount, a new schedule assignment attempt is made. However, the candidate with the lowest product of quality and cycles until saturation is removed, since it takes up the largest amount of resources (resets) relative to the provided quality. The schedule assignment process is repeated until a sufficient number of assignable candidates can be found or until there are no more stars left to be initially excluded. At this point, the best previously found setup is used (highest number of stars possible to assign). From the best found setup, the candidates with the highest qualities up to the desired number, if available, are selected as guide stars. A schematic example of the described algorithm is shown in Figure 3.2, where the candidate with 2 cycles until saturation is assumed to have the lowest product of quality and cycles until saturation.

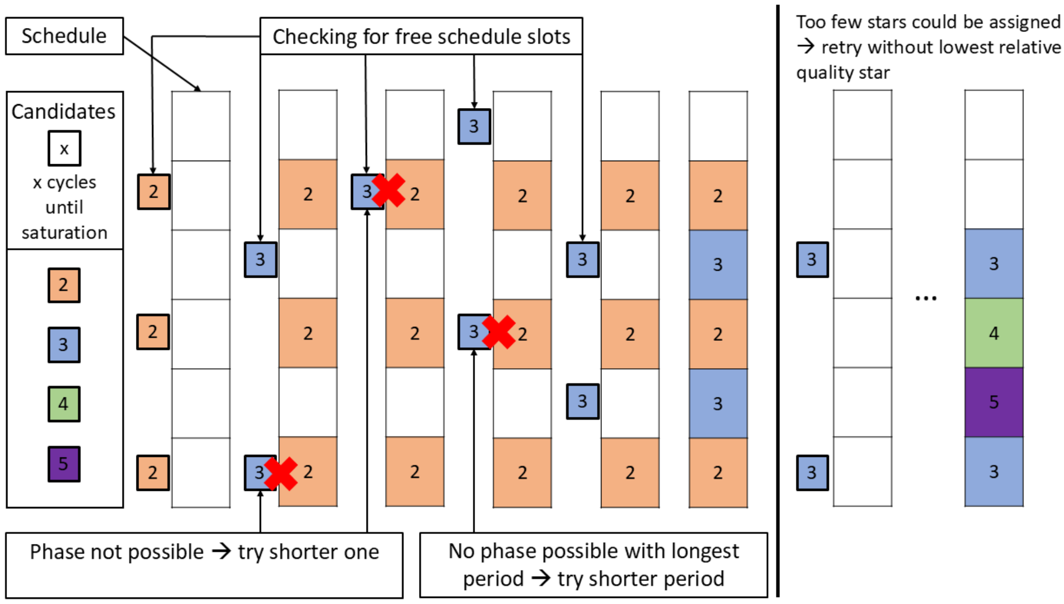

Figure 3.2.: Schematic example of how guide star candidates are assigned to the initially empty schedule and what happens if a star cannot be assigned with its longest possible period.

The Guiding Windows Reset Slot Assignment Strategy is required for

preventing the centroid performance degradation due to saturation by individually resetting the guide stars while keeping the maximum number of resets per cycle limited to ensure synchronization of the frame readout between the two NIR detectors.

3.2.6. AOCS Information

The second to last step of the Acquisition algorithm is the calculation of the first AOCS information. For the selected guide stars, the previously computed centroids for both differential FFs are used. The first set of centroids serve as a reference (Acquisition lock) and are compared to the second one. By combining the deviations of the individual centroid pairs a single 3-axes pointing offset from the reference is obtained, the so-called AOCS information. It is communicated to the satellite platform. This procedure is nearly identical to the Guiding algorithm repeatedly performed during the exposure. The primary difference between AOCS information calculation during Acquisition and Guiding is the set of centroids used as a reference, as described below.

Centroid Calculation

The calculation of the individual centroid performed for both differential FFs is identical to the previously utilized ARIEL version described above. This is, an IWC step is combined with several IWCoG cycles.

In light of the similarities between cosmics and stars, due to the small PSF, the centroid validation described in Section 1.4.2 is modified. The new rules/steps are evaluated on the central 5×5 px around the centroid and are as follows:

- Weakened source extraction cosmic removal (neighbor pixel ≥ 2 above $\boldsymbol{\sigma} \times$ background or < 5 with slope > 100)
- Image not constant (minimum $\neq$ maximum)
- Feature not too sharp (central px $<$ 60% of signal)
- Clear peak visible (central px $>$ mean)
- The Pearson correlation coefficient between signal and weight Gaussian is large ($\text{pearson}_x \cdot \text{pearson}_y >$ Pearson Limit)

Centroid Combination

After the centroiding algorithm has provided precise positions for all the guide stars, the movement of the telescope's Line of Sight (LoS) relative to the reference needs to be determined and sent to the Attitude and Orbit Control System (AOCS) for correction.

To accomplish this, the movement of the telescopes needs to be split into its two components. First, the drift or across LoS movement, that keeps the relative position of the guide stars to one another intact. Second, the rotation or along LoS movement that changes the relative position of the guide stars.

The different steps performed are sketched in Figure 3.3. The first step calculates the relative position of each guide star as viewed by every other guide star in the new image and in the reference (Acquisition lock) (see Figure 3.3a). The difference in relative position between new image and reference is then averaged on a per-star basis (using the deviation from the mean shift as weights) to obtain an estimate of the star's position if no rotation had occurred. The different non-rotated position guesses are effectively obtained by tracing from the new position back along the reference relative positions as drawn in Figure 3.3c. Comparing the averaged estimates with the reference positions, gives a first approximation for the shift occurred (see Figure 3.3d). The shift approximation is then subtracted from the found movement of the stars to recover the pure rotational component of the star's position change on the detector (see Figure 3.3e). From this, the rotation angle per star is calculated by simple geometry using the approximate location of the rotation axis provided by the user (see Figure 3.3f). The different rotation angle approximations are averaged using the deviation from the mean angle multiplied by the distance from the rotation axis as weights. The distance from the rotation axis is included, because stars farther away from the axis are moved by more pixels for the same rotation angle, which makes the rotation more noticeable.

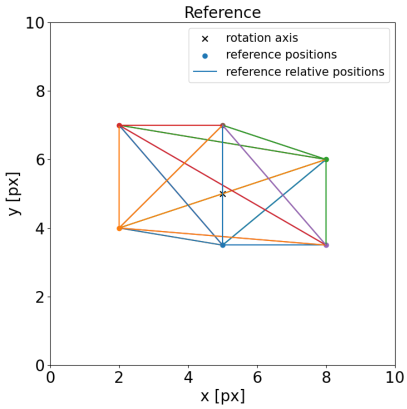

(a) Reference (Acquisition lock)

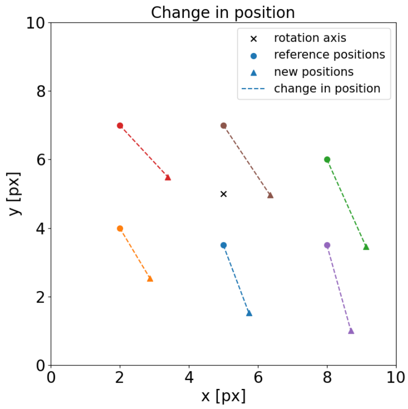

(b) Change in positions

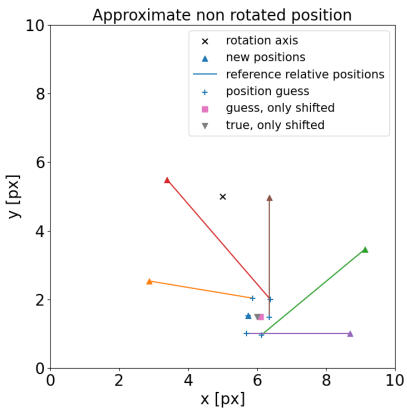

(c) Guess for non-rotated position

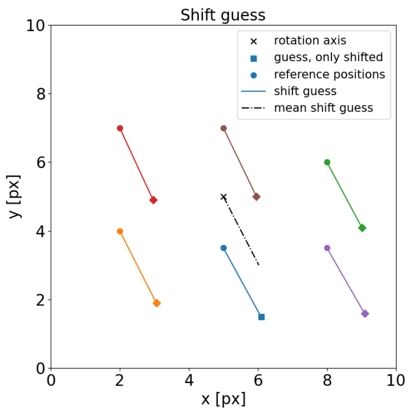

(d) Guess for shift movement

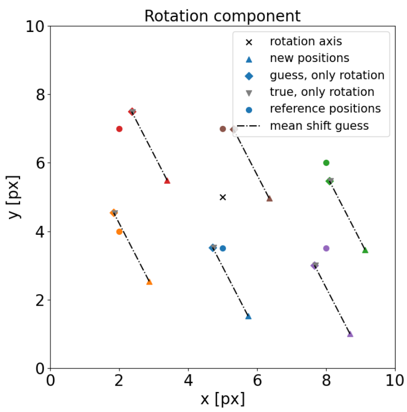

(e) Pure rotation component

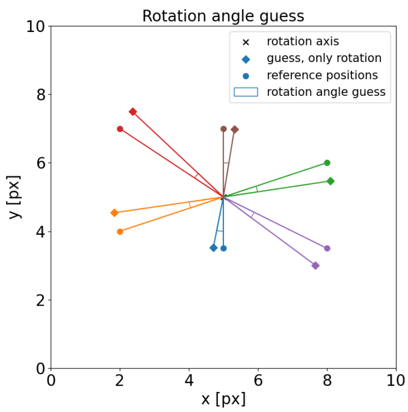

(f) Guess for rotation angle

Figure 3.3.: Schematic description showing the procedure calculating the shift and rotation angle guesses

In order to refine the movement estimates further, the process described above is repeated iteratively, where the rotation angle estimate is used to sequentially de-rotate the guide star positions from the current image relative to the reference one. The final estimate for the along LoS rotation angle is the sum of the angles found during the iterations. The across LoS movement is measured after de-rotating the new positions by the final angle estimate.

The recovered angles (Euler angles) can then be optionally converted into a quaternion prior to transmission to the AOCS.

Quaternion Conversion

The required format of the AOCS information is presently not yet defined. The two options are: Euler angles or a quaternion. In case of Euler angles, no further steps are needed after the centroid combination. In case a quaternion is required, the Euler angles are converted via a set of already prepared functions using the small angle intermediate DCM step method taken from Großekatthöfer and Yoon (2012) and described in detail above.

In the overall ARRAKIHS algorithm

the individual centroid calculations follow the implementation from ARIEL, but they are then combined into a single AOCS information by splitting the impact of drift and rotation via the changes in relative position of the guide stars.

3.2.7. Acquisition Quality

The last step of the Acquisition is the calculation of a quality estimator for the Acquisition Lock found. While the number of guide stars is the main factor determining the precision of the AOCS information, this Acquisition quality q_{acq} is intended to provide some additional insight.

The Acquisition Quality q_{acq} is calculated via Equation (3.2), where n_{gs} is the number of guide stars found, $q_{\mathrm{gs},i}$ is the guide star quality of the i-th guide star, dist_i is the distance of the i-th guide star from the rotation axis and dim is the size of the image (2048 px). The number of guide stars found n_{gs} is included in the calculation so that the single quality value can also represent the decrease in error with increasing n_{gs}. The distance from the rotation axis dist_i is included once more due to its impact on the along LoS rotation as described above.

$$q_{\mathrm{acq}} = n_{gs} \cdot \frac{\sum_{i=1}^{n_{gs}} q_{\mathrm{gs},i} \cdot \mathrm{dist}_i/\mathrm{dim}/2}{\sum_{i=1}^{n_{gs}} \mathrm{dist}_i/\mathrm{dim}/2} \tag{3.2}$$

A quality parameter for the Acquisition has been formulated.

3.2.8. Acquisition Lock

During development, the question was raised, which of the two sets of centroids obtained by the Acquisition should be used as the reference (Acquisition lock) for the Guiding. The pros and cons of the two choices are discussed below.

First Centroids as Acquisition Lock

Pros:

- The first AOCS information provided at the end of Acquisition uses the same reference utilized later during Guiding.

Cons:

- The platform has had less time to settle until then, thus a larger residual drift is more likely. The readout-time-difference based relative-movement caused by the drift will be encoded in the Acquisition lock. This could have detrimental effects on the long term precision of the AOCS information during Guiding. Analyses of that effect are beyond the scope of this thesis, but will be carried out in the future.

Second Centroids as Acquisition Lock

Pros:

- The platform has had more time to settle, thus the residual drift is likely already slower. Therefore, the guide star positions in the Acquisition lock will be impacted less by the readout-time-difference based relative-movement.
- When using the second set of centroids as reference, the guiding windows are centered on them. Therefore, the guide stars are in the center of the windows at the end of Acquisition, thus the distance to the window edges are maximized. This makes it easier for the platform to keep the guide stars inside the windows during the switch-over to Guiding (see below).

Cons:

- The first AOCS information produced at the end of Acquisition will be relative to a different reference than the ones during Guiding. Regardless, the first information can still be used to get an estimator of the residual drift.

All the pros and cons mentioned here also apply to the use of the third centroid set obtained during Acquisition, when using the continuous Acquisition option (see below). Additionally, the continuous Acquisition produces two AOCS information packets relative to the first centroid set positions, meaning that the platform could already counteract some of the residual movement before the Acquisition lock centroids are calculated, thus reducing the encoded errors further.

Conclusion

In summary, using the second centroids as Acquisition lock seems to be more advantageous for the Guiding. While the different references used for AOCS information between Acquisition and Guiding will require careful handling by the platform. The reduction in the amount of relative movement encoded in the Acquisition lock cannot but be advantageous for the precision of the Guiding and therefore the quality of the science images.

The analysis concludes, that

using the second set of centroids for the Acquisition lock is the preferred option.

3.2.9. Sequencing

Another question raised by ESA during the development of the algorithms for this thesis was, how the transition from Acquisition to Guiding should be handled. One important thing to note is that the detector needs to be reset and then reconfigured after Acquisition in order to set up the regular guiding window resets.
The sequencing describes the order of frame readouts, resets and other steps performed from initialization through Acquisition to Guiding. In the following, two possible options for the sequencing are discussed. The options differ in their transition from Acquisition to Guiding and how additional Acquisition attempts (reacquisition) are performed in cases where the first one fails. First, blocked Acquisition where there is a fixed reset and possible transition to Guiding after every 3 frames. Second, continuous Acquisition where the reset is triggered by a successful Acquisition.

Both options start with resetting and reconfiguring the detector for Acquisition using the setup provided by the user. Additionally, the second NIR channel is also reset, configured (with a dummy setup) and started at the same time to keep it synchronous with the channel used. Both versions can produce at least one AOCS information relative to the positions in the first differential frame used by the successful Acquisition attempt. After a successful Acquisition both NIR channels are reset, the configuration determined by the Acquisition algorithm is loaded onto the active FGS channel, a configuration maintaining synchronicity is loaded onto the second one and all four NIR and VIS channels start the exposure simultaneously. After the second NIR readout during the exposure and every following one until the end of exposure an AOCS information relative to the Acquisition lock is produced by the FGS. The Acquisition lock can either be the guide stars' positions in the first or last differential frame used by the successful Acquisition process.

Blocked Acquisition

Blocked Acquisition uses fixed blocks of 3 FFs followed by a reset. While the reset is performed, the Acquisition algorithm finishes its remaining calculations based on D2 (second differential frame) and decides if it was successful. If it was not successful, the detector configuration remains unchanged and a new block is started. If Acquisition was successful, an AOCS information relative to the D1 positions can be provided, the

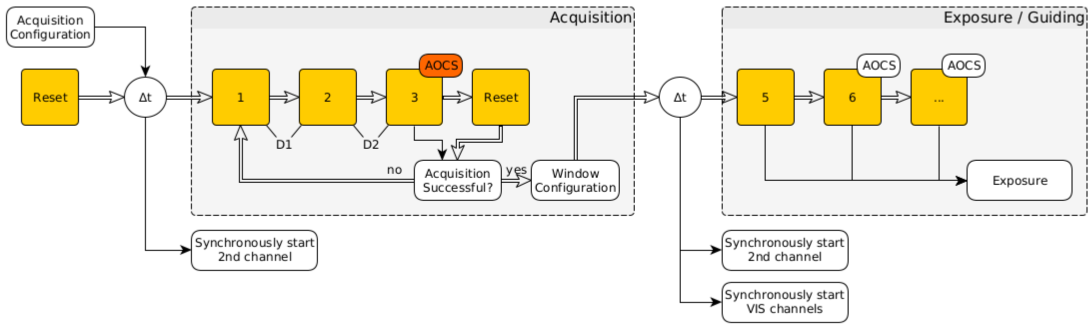

Figure 3.4.: Blocked Acquisition sequencing, where there are fixed blocks of 3 FFs and a reset. The yellow boxes represent (reset) frames, Dx represent differential frames, Δt circles represent detector reconfigurations, hollow arrows denote the sequence, thin arrows show data flow or dependencies and bubbles with AOCS mark frames after which an AOCS information is provided (in white relative to the Acquisition lock, in orange relative to the positions in the differential frame before the previous one)

detector is reconfigured with the setup calculated and the FGS switches to Guiding. A schematic for the blocked Acquisition sequence is shown in Figure 3.4.

The main advantage of blocked Acquisition is the fixed reset at the end of the 3 FFs. It allows to reach the minimal time possible between successful Acquisition and start of the exposure/Guiding, since the reset necessary for reconfiguration (setup guiding windows) is already ongoing when the success of the Acquisition is determined. In contrast to the continuous Acquisition, the reset after each block means that all blocks have the same starting conditions. This enables to use even quite bright stars as guide stars in every Acquisition attempt, if they don't saturate before the third FF.

The disadvantage of this option is the long time every additional Acquisition attempt will take (4 frames: 3 FF + reset).

Continuous Acquisition

Continuous Acquisition performs FF readouts until a successful Acquisition triggers a reset. With every new frame a new Acquisition process is started, so that up to 3 are running in parallel and after every frame following the second one a successful Acquisition might occur. If an Acquisition is successful, an AOCS information relative to the positions in the first differential frame used by the process can be provided, a reset is performed after the end of the ongoing readout at the time. After the reset, the detector is reconfigured with the setup calculated and the FGS switches to Guiding. A schematic for the continuous Acquisition sequence is show in Figure 3.5.

The main advantage of continuous Acquisition is the fast retry time. Starting after the second differential frame, i.e. every ≈1.45 seconds, a new Acquisition process could

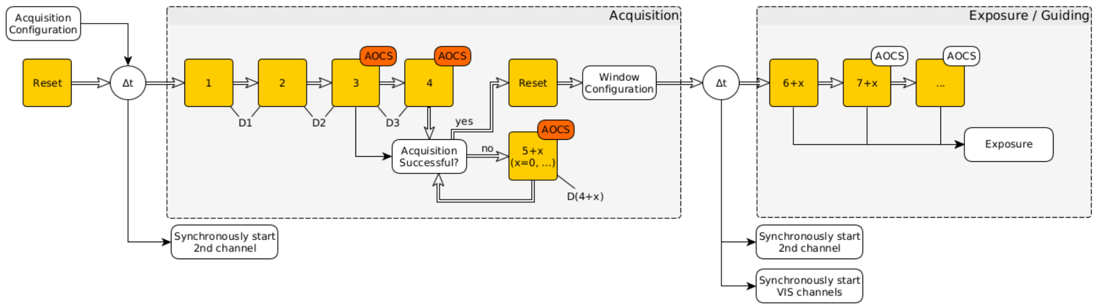

Figure 3.5.: Continuous Acquisition sequencing, where multiple Acquisition processes run in parallel and the reset is triggered by a successful one. The yellow boxes represent (reset) frames, Dx represent differential frames, Δt circles represent detector reconfigurations, hollow arrows denote the sequence, thin arrows show data flow or dependencies and bubbles with AOCS mark frames after which an AOCS information is provided (in white relative to the Acquisition lock, in orange relative to the positions in the differential frame before the previous one)

be successful and trigger the transition to the exposure/Guiding. Additionally, a second AOCS information relative to the positions in the first differential frame used can be sent before the break caused by the reset and detector reconfiguration.

The primary disadvantage of this option is the longer delay (by 1 frame) between successful Acquisition and start of exposure/Guiding, because the reconfiguration reset is only started after the end of the frame readout which is ongoing when the Acquisition finishes calculations. Additionally, the CPU usage is considerably higher, since up to 3 Acquisition processes are running in parallel. Furthermore, the maximum possible brightness for guide stars decreases with every new Acquisition attempt, because some sources may be in danger of saturating before the successful attempt and thus need to be excluded.

Some of these disadvantages could be mitigated by a hybrid version between blocked and continuous Acquisition, with fixed resets after N (>3) frames. If the successful Acquisition occurs during the reset, the extra delay is skipped. The periodic resets would also restore the brightness limit.

PDE Transition to Guiding

The transition between Acquisition and Guiding creates a gap in the produced AOCS information. If the centroids from the last AOCS information calculated during Acquisition is used to place the guiding windows, the gap is 3 frame-readout times (reset + 2 frames for first differential one) + 0.2 s[3] long. If the guide stars leave the guiding windows during this time, the calculation of the first AOCS information during Guiding will fail to find the stars. Therefore, a PDE requirement for the transition between Acquisition and Guiding is formulated here.

The centroiding locates a star in the center of its brightness distribution for the used frame, meaning that if a star for example moves with a constant direction and velocity of 4 px/frame, the centroid will be 2 px behind the star's true position at readout. Therefore, the last Acquisition frame used also needs to be taken into account when formulating the PDE requirement. In the worst case, the star is static during the last Acquisition frame and located at the edge of the central pixel and then during the gap moves on the shortest path to the nearest window edge. In this scenario, using a 16 px guiding window, the shortest path is 7 px long. Therefore, the star needs to remain within 7 px from the start of the last Acquisition frame to the end of the second Guiding frame (first differential frame). In total, this equals to a time-span of $6.0\,\text{s} = 4 \cdot 1.45\,\text{s} + 0.2\,\text{s}$ [4].

The sequencing concepts demonstrate, that

> the order of operations for the transition between Acquisition and Guiding has been considered and connected platform pointing requirements were formulated.

[3] After the detector reset the detector reconfiguration of about 0.2 s (TBC) needs to take place. The time needed for reconfiguration is unknown at the time of writing.

[4] see footnote 3

4. Algorithm Performance

In this chapter, the different performance analyses carried out for the Acquisition algorithm are described.

Unless stated otherwise, the calculations are performed for the NIR-2 band, as it originally was narrower than the NIR-1 one. Thus, the stars were fainter and therefore it was the more challenging case. During the development of this thesis, the fourth ARRAKIHS Consortium meeting took place. There, a new filter curve for NIR-1 was presented. The NIR-1 and NIR-2 bands now have the same bandwidth, but are shifted in wavelength. NIR-2 is kept as the primary band for analyses in order to retain the results produced prior to the change.

4.1. Default Parameters Used

The performance analyses shown in this chapter use the values listed in Table 4.1 as the setup for the Acquisition algorithm, unless stated otherwise.

The initial parameters were found during algorithm development. An analysis is carried out to optimize the parameters by varying individual ones and tracking the change in Acquisition performance. The analysis shows it would still be possible to further optimize some parameters towards better precision of AOCS information, but the improvement would come at the cost of reducing the number of guide stars found. In challenging cases (e.g., large residual movement), where the algorithm already finds fewer stars than usual, this would lead to an overall reduction in precision. An example of this behavior is shown in Figure 4.1 for the σ parameter.

Table 4.1.: Default Acquisition parameters used for performance analyses

Name	Description	Value	Limitations
`Bin size`	Side length of the area added to one new pixel during binning	1	int ≥ 1
$\mathtt{N_{gs}}$	Maximum number of guide stars to select if possible	25	int >2
`Exclusion limit`	Brightness cutoff for search area definition	65535/3[1]	int ≥ 1

[1] $65535 = 2^{16} - 1$, ARRAKIHS images are 16-bit unsigned and there are 3 frames readouts during Acquisition

Name	Description	Value	Limitations
Exclusion min size	Minimum number of consecutive pixels in a row above the limit for a feature to be excluded	2	int ≥ 1
Exclusion buffer	Additional space around found feature also excluded	20	int ≥ 0
Search area radius	Outer radius of the search area	940 px	int ≥ 1
Search area center	Location of the center of the outer circular boundary	(1024,1024) px	2 x int [0-2048)
Search area type	Type of the search area's shape	circle	all, circle, box, u-shaped
Search area parameters	Additional parameters for defining the search area's shape	inner radius 512 px center (1024,1024)	depends on type
σ	Level above background for source extraction	6	>0
N_{target}	Number of bright pixels considered during source extraction	1000	int ≥ 1
Maximum signal	Maximum signal before source is considered in danger of saturation	$176/169{\cdot}10^3$ NIR-1/2[2]	int ≥ 1
Neighbor region size	Size of the region searched for neighboring stars	24	int $\geq$ ROI size
w_p	Weight for guide star quality position component	1	float
$q_{p,min}$	Minimum value for position quality	1	float
$q_{p,start}$	Start of position quality slope	0	int ≥ 0
$q_{p,stop}$	End of position quality slope	0	int ≥ 0
w_b	Weight for guide star quality brightness component	1	float
w_n	Weight for guide star quality neighbor component	1	float
ROI size	Size of area for initial centroid calculation	16	int $\geq$ refined ROI size
refined ROI size	Size of area for iterative centroid calculation	8	int ≥ 5 [3]

[2] The values represent a worst-case scenario. The over-sampled PSFs are moved on sub-pixel scale to find the configurations where the least and most amount of light is concentrated in the central pixel. Afterwards, the signal which saturates the central pixels in the "concentrated" case is calculated and applied to the "diffuse" case. The signal observed under diffuse conditions is used as the limit.

[3] Centroid validation checks central 5 x 5 px

Name	Description	Value	Limitations
$\texttt{FWHM}_{x/y}$	FWHM of the weight function used by the IWCoG in x/y-axis	25	float >0
`Iterations`	Iteration count for IWCoG	7	int ≥ 1
`Pearson limit`	Minimum value of Pearson correlation coefficient for centroid validation	0.3	float >0
`Overlap buffer`	Additional buffer distance between potential guiding windows for overlap prevention	0	int ≥ 0
`Reset budget`	Maximum number of guiding window resets allowed per readout cycle	2	int ≥ 1
`Exposure time`	Time per readout cycle	1.45 s	float >0
`Euler iterations`	Number of iterations for Euler angle calculation	7	int ≥ 1
`Rotation axis x/y`	x/y coordinate of the rotation axis	1024	int 0-2048 (detector dimension)

4.2. Acquisition

4.2.1. Number of Found Stars

In order to investigate the ability of the Acquisition algorithm to find a sufficient number of guide stars for the galaxies in the ARRAKIHS target pool (Consortium, 2025), a simulated dataset containing the required one raw FF and two differential ones for all 240 galaxies from the target pool was created per NIR channel with the galaxies centered in the image. For each of the galaxies the Acquisition algorithm is instructed to attempt to find up to 50 guide stars inside the FoV excluding the inner 512 pixels (circular shaped region). The histogram of the number of guide stars found in NIR2 is shown in Figure 4.2. For all galaxies, more than 25 guide stars are found. As described in the section about AOCS information precision, 25 guide stars is approximately the number where the AOCS information fulfills its requirements. The centroids of the stars found are compared with the true positions from the dataset used and a deviation of less than one pixel is considered to be a correct detection. Only 8 out of 11890 guide stars found are detected incorrectly, with 7 of those due to cosmics within or at the edge of the PSF on the second differential FF. The last incorrect detection origins from a very close double star. This low number of incorrect detections also verifies the reliable functionality of the centroid validation.

Guiding Window Reset Slot Assignment Strategy Performance

A further crucial component to verify is the reset slot assignment. For the same setup as described above and a maximum of two resets per cycle, the number of candidates for

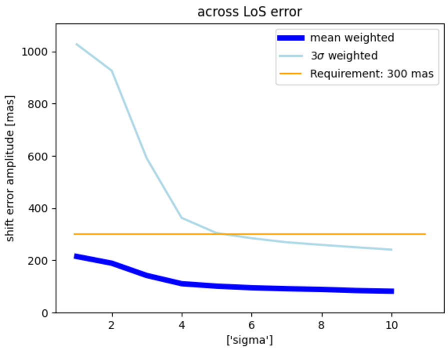

(a) Across LoS error for 25 guide stars and different σ

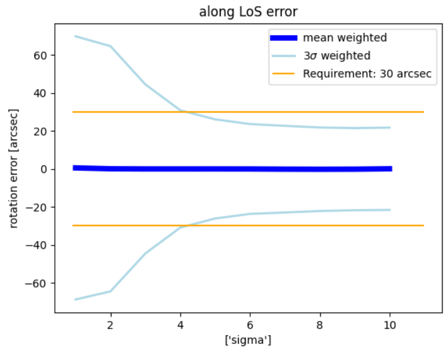

(b) Along LoS error for 25 guide stars and different σ

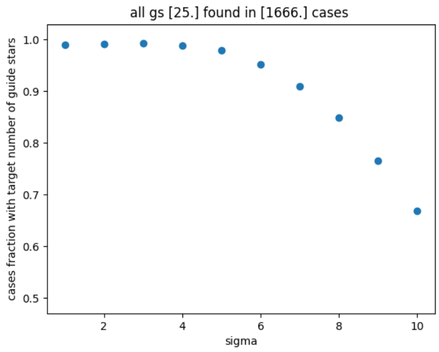

(c) Fraction of cases with 25 guide stars for different σ

Figure 4.1.: Parameter optimization for σ

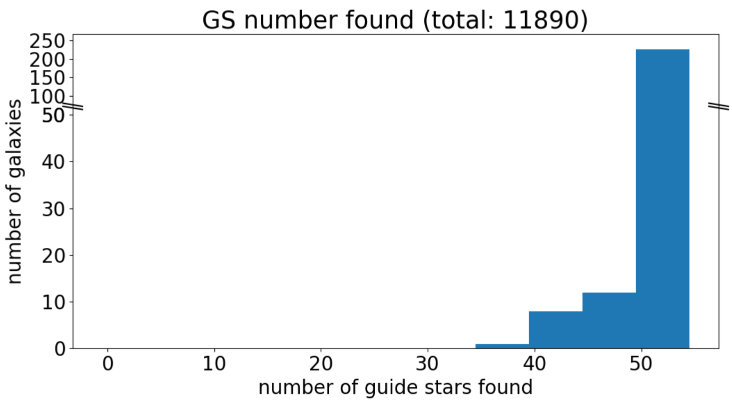

Figure 4.2.: Number of guide stars found in NIR2 for all 240 galaxies from the target pool when the galaxy is centered and selection region is limited to the annulus with inner radius of 512 pixels

NIR2 that could be assigned to the schedule by the guiding window reset slot assignment strategy is provided in Figure 4.3. By comparison with Figure 4.2 it becomes clear that the strategy is capable of assigning sufficient (≥ 25) guide stars in all cases where there are sufficient stars available in the first place. One important thing to note is that nearly all stars are assigned with their maximum possible period. This means that the variation of the phase is sufficient to resolve most schedule conflicts. Therefore, the used assignment strategy is capable of efficiently utilizing the available reset budget. If the period had to be shortened, the star would experience more resets than necessary to prevent saturation during the exposure time. Another advantage of the smallest number of resets possible per star is, that, depending on the star's location on the detector, less signal is observed in the first frame after reset. This reduction in signal can degrade the individual centroid performance or even prevent the calculated centroid from passing its validation for very weak stars. Thus, the quality of the combined AOCS information is negatively affected, too. The number of two resets per cycle is chosen to demonstrate that the algorithm can successfully handle very restrictive cases. If the number of resets per cycle is increased, more stars will be assigned with their maximum period. Additionally, less schedule conflicts will occur overall, which will also speed up the assignment process.

The NIR2 analysis is shown here (Figure 4.3) to allow direct comparison with Figure 4.2.

Combining the results in Figure 4.2 and 4.3 shows, that

the Acquisition algorithm can find and assign sufficient guide stars to successfully calculate the AOCS information for all galaxies in the ARRAKIHS target pool.

4.2.2. Acquisition Robustness

Wrt Drift

In order to determine the maximum drift tolerable before the error of the first AOCS information starts to increase or the algorithm completely fails, a simulated dataset based on multiple galaxies[4] is created. For each of the galaxies, image sets are produced with increasing drift parallel and diagonally to the detector axes. The Acquisition algorithm is then tasked with selecting up to 25 guide stars if possible and the drift found is compared with its true value. An example of the different drift directions is shown in Figure 4.4.

The evolution of the across LoS error is shown in Figure 4.5. At about 4 px per 1.45 seconds the quality of the estimate starts to degrade and at approximately 5 px per 1.45 seconds the mean estimate no longer fulfills the 300 mas requirement. The error continues to increase near linearly beyond that, with each of the estimates being based on a decreasing number of guide stars, as demonstrated in Figure 4.6. The decrease in the number of guide stars found is caused by the signal being spread out over more pixels and eventually dropping below the limit used for background distinction. With 5.3 px per 1.45 seconds or more the guide stars move outside the 16 px guiding windows

[4]Simulated galaxies: NGC1232, NGC1433, NGC1448, NGC1515, NGC4051, NGC4800, NGC4826, NGC5377

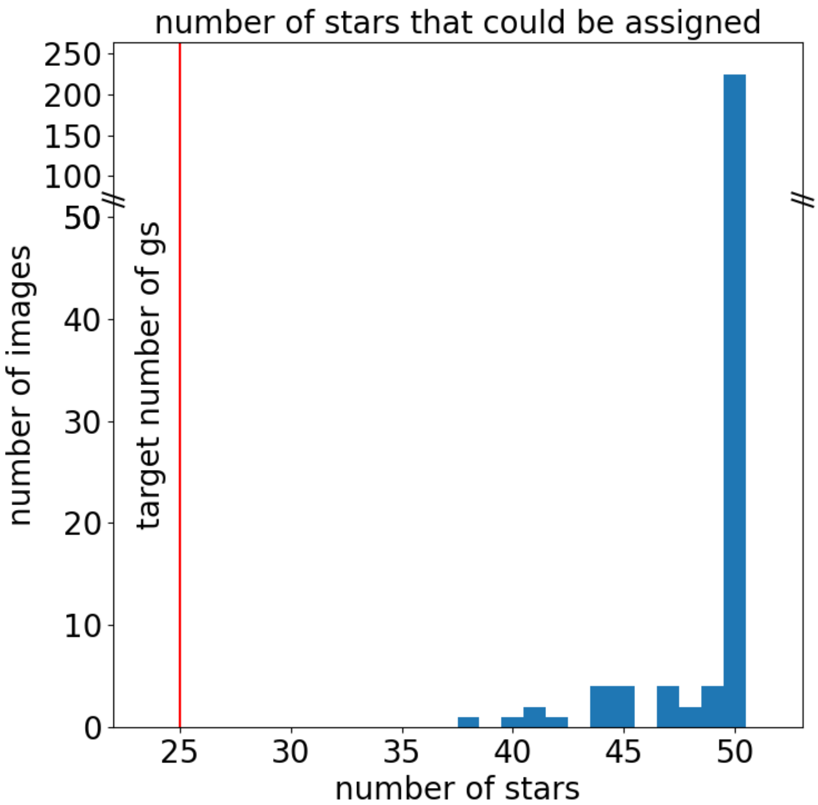

Figure 4.3.: Histogram of the maximum number of guide stars for NIR2 that could be assigned by the guiding window reset slot assignment strategy to the schedule. All cases to the right of the red line could assign more stars than needed (25), thus not all candidates would be selected as guide stars

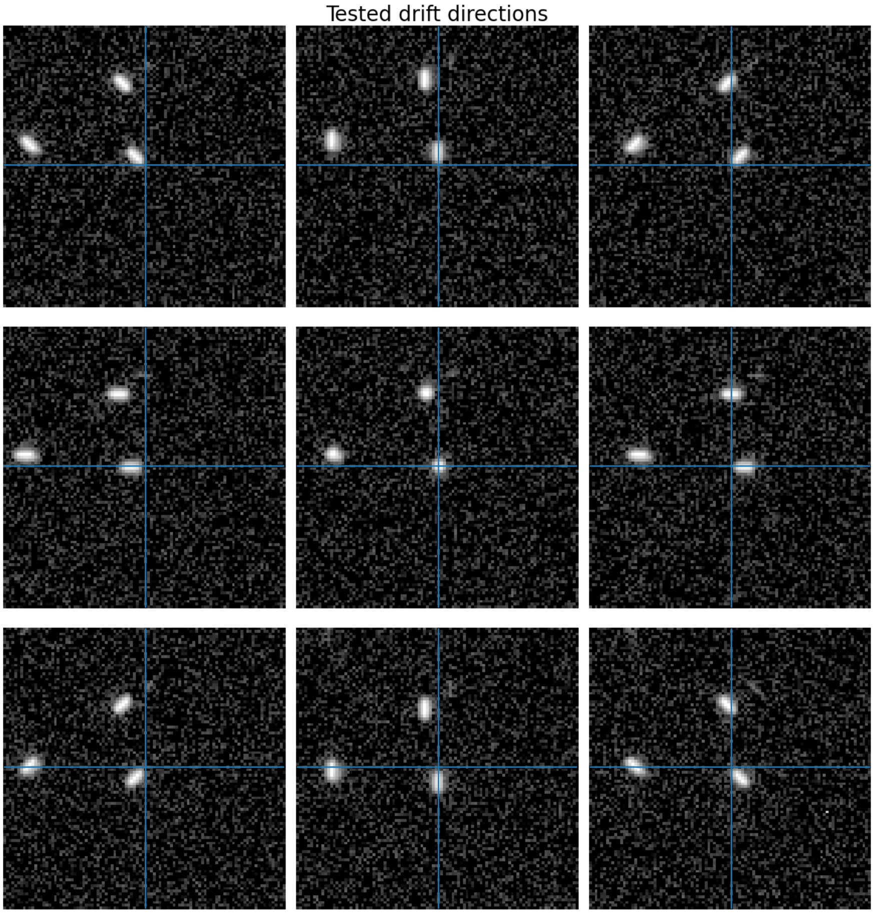

Figure 4.4.: Demonstration of how the different drift directions influence a group of three stars found in the field of NGC1515. The shift amplitude is the same at 5 px / 1.45 s, with the exception of the central image where there is no drift

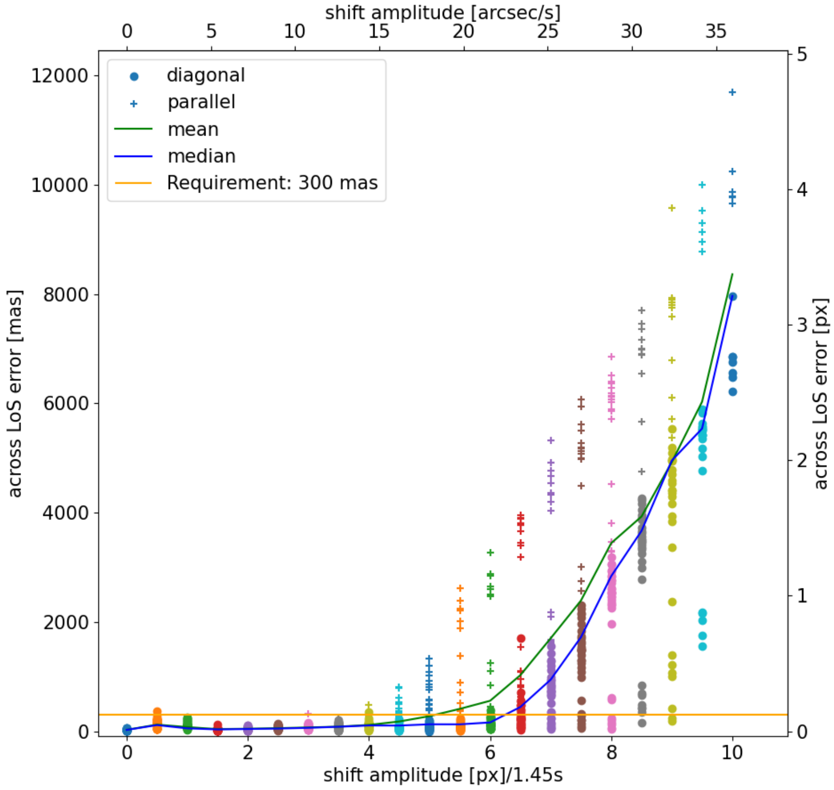

Figure 4.5.: Evolution of across LoS error with increasing drift while the Acquisition tries to find up to 25 guide stars

before the end of the last readout depending on the angle of the drift relative to the detector axes and only a part of the stars' image's tail is still observed. This causes the second centroid to incorrectly estimate the star's position closer to the first one and thus causes the linear error increase. Additionally, this effect also explains why the parallel test drift cases start to show worse performance than the diagonal ones, because the diagonal distance to the window corners is longer by a factor of $\sqrt{2}$. Furthermore, the same effect is also responsible for the few outlying data points showing better performance for both the diagonal and parallel cases. Due to the default `ROI size` of 16 px being event the windows can not be placed symmetrically around the pixel containing the first centroid. Thus the distance (parallel and diagonal) from window center to edge is longer for some test cases and the linear error increase sets in only at higher shift amplitudes for those.

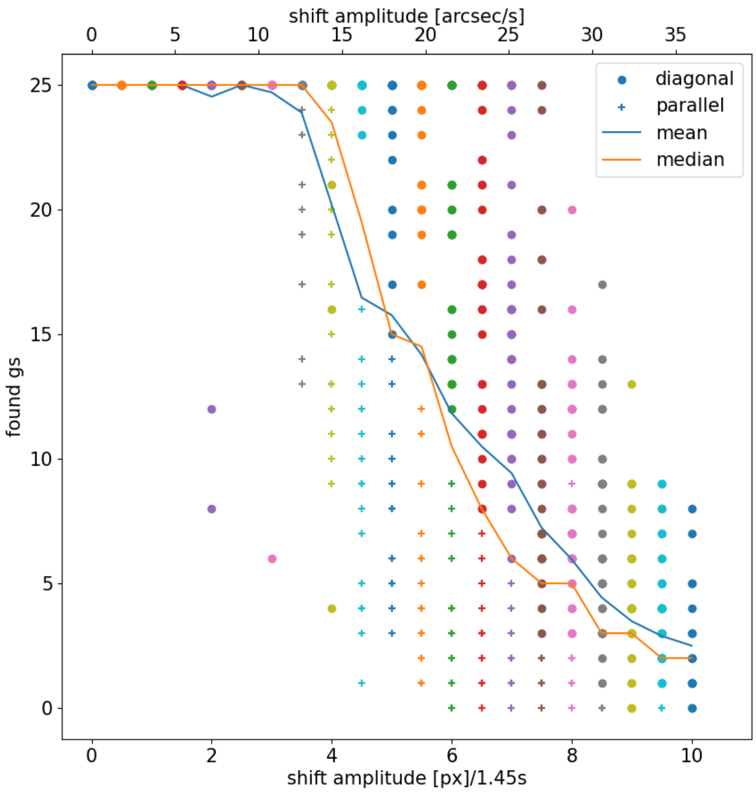

Figure 4.6.: Evolution of the found guide star number with increasing drift while the Acquisition tries to find up to 25 guide stars

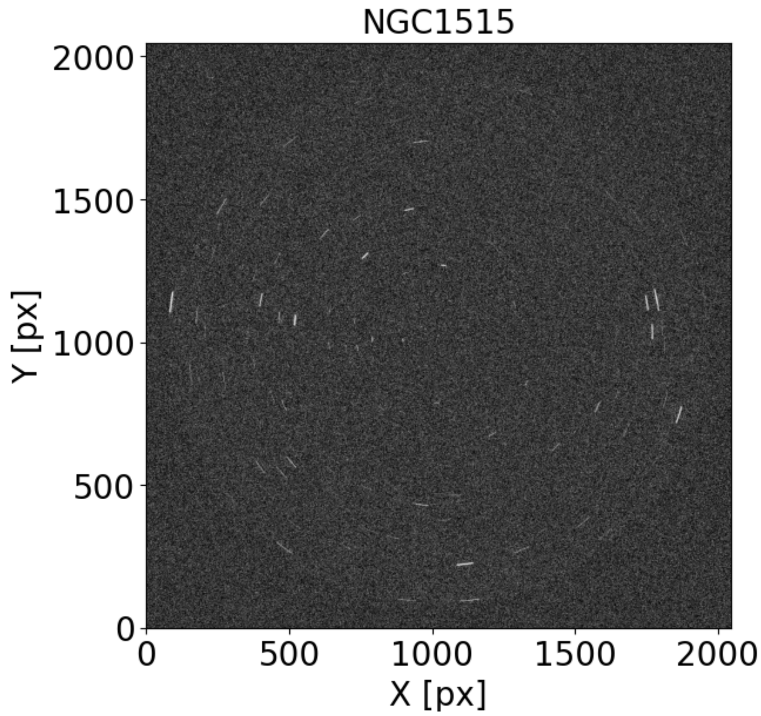

Figure 4.7.: Differential image of NGC1515 for a rotation rate of 10 000″/s

Wrt Rotation

In order to determine the maximum rotation rate possible before the error of the first AOCS information starts to increase or the algorithm completely fails, a simulated dataset based on multiple galaxies[5] is created. For each of the galaxies, image sets with increasing rotation rate are produced. The Acquisition algorithm is then tasked with selecting up to 25 guide stars if possible and the error of the rotation rate found is recorded. An example for a high rotation rate is show in Figure 4.7.

The evolution of the along LoS error is shown in Figure 4.8. At about 100 arcsec per 1.45 seconds the estimate starts to degrade and at approximately 1300 arcsec per 1.45 second the median estimate no longer fulfills the 30 arcsec requirement. Similar to the robustness wrt drift, the error appears to linearly increase beyond that point (not shown) and the estimates are based on a rapidly decreasing number of guide stars due to the declining signal-to-noise ratio.

[5]Simulated galaxies: NGC1232, NGC1433, NGC1448, NGC1515, NGC4051, NGC4800, NGC4826, NGC5377

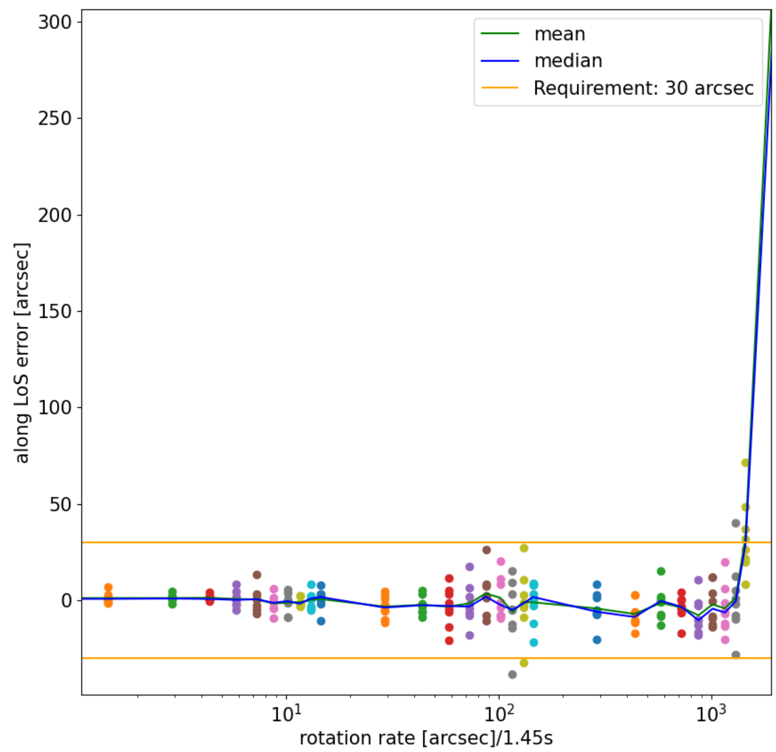

Figure 4.8.: Evolution of along LoS error with increasing rotation rate while the Acquisition tries to find up to 25 guide stars. The few data points beyond a rotation rate of 1500 arcsec per 1.45 second are not shown since their error is far beyond the 30 arcsec requirement, due to the estimations being based on low single digit number of guide stars.

Worst Case

As mentioned in the previous two sections, the main mechanism causing a decrease in precision at higher drift/rotation rates is the drop in guide stars found (see Figure 4.6) caused by the decline in signal-to-noise ratio as a result of the stars signal being spread out over more pixels due to the movement. Additionally, jitter (as described below) has the same effect, especially at higher frequencies. In order to formulate a RPE requirement which ensures that sufficient guide stars are found, a worst case analysis is carried out. In this case, the jitter (+ drift & rotation) spreads the signal of a star rotationally symmetric (signal split over maximum number of pixel). A Gaussian with different σ is used to represent this. As shown in the Acquisition Performance analysis, the Acquisition is capable of finding 50 guide stars in nearly all cases when no movement is present ($\sigma = 0$). The AOCS precision analysis shows that about 25 guide stars are necessary to fulfill the precision requirements. Therefore, the limit is a Gaussian with σ_{limit} where the number of guide stars found

$$N(\sigma_{\text{limit}}) = \frac{1}{2} \cdot N(\sigma = 0)$$

In order to simulate this, signals of 1000 guide stars found in the Acquisition Performance analysis are randomly drawn using the $\log_{10}(\text{signal})$ as weights [$\log_{10}(\text{signal})$ is used in the brightness component of the guide star quality q_b]. For each of the 1000 stars, small (31×31 px) images are simulated with the stars in the center and the PSF is convolved with Gaussians of increasing σ. The images include all detector properties and effects used for the other analyses except cosmics, because cosmics do not contribute to the star's signal-to-noise ratio. An example of how a star's signal is affected by the increasing σ is shown in Figure 4.9. For each image, the Acquisition algorithm is tasked with finding the star. The default configuration is used except for the brightest pixel count, which is reduced from 1000 to 100 due to the smaller image size (faster calculation). The evolution of the number of stars detected is displayed in Figure 4.10. Up to a σ of about 0.75 px nearly all stars are successfully found. The initial small increase in detections is caused by the star's signal being spread out to a few more pixels and thus it becomes easier to differentiate it from a cosmic (clearer signal in neighbor pixels). After a σ of about 0.75 px the detection count linearly decreases and reaches zero for a σ of 2.5 px. The σ_{limit} is calculated via linear interpolation of the neighboring data points and found to be about 1.58 px. A σ of 1.58 px translates to 4.74 px or 11.75 arcsec at 3σ.

By joining the preceding three analyses,

> the cutoff points were identified where the impact of (combined) residual drift, rotation and jitter degrade the algorithm's performance beyond acceptable limits.

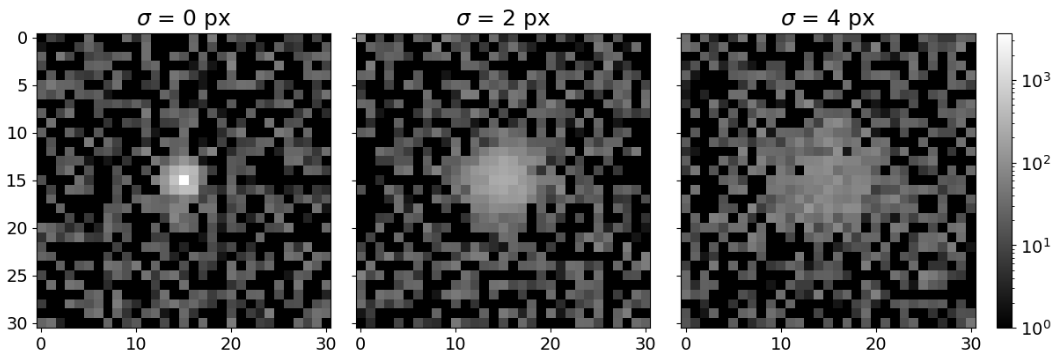

Figure 4.9.: Example of a star with a signal of 10000 photons/s and a PSF convolved with Gaussians of different σ

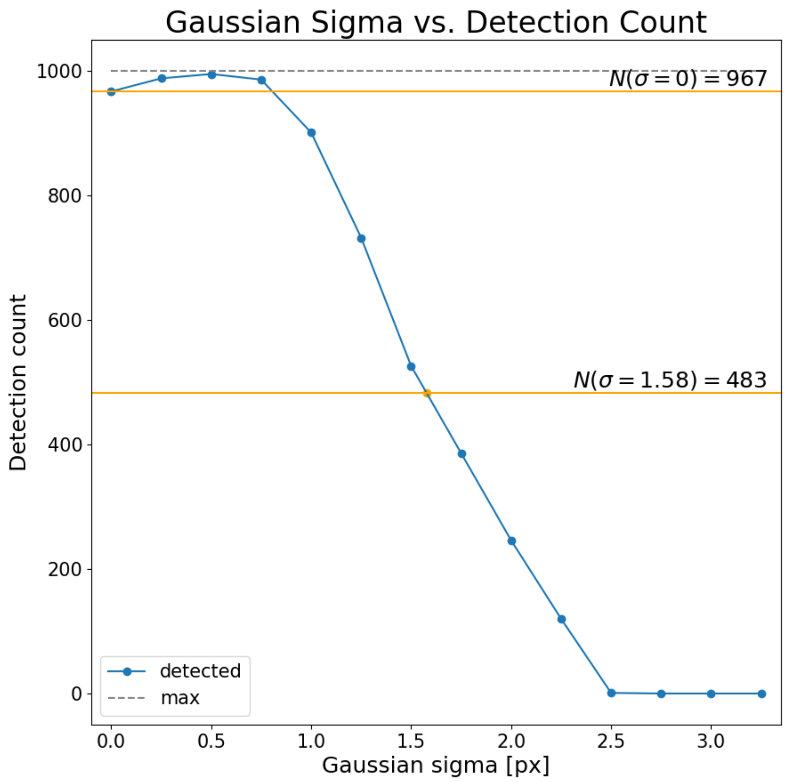

Figure 4.10.: Number of stars detected for increasing Gaussian σ. The σ_{limit} is found by $N(\sigma_{\text{limit}}) = \frac{1}{2} \cdot N(\sigma = 0)$

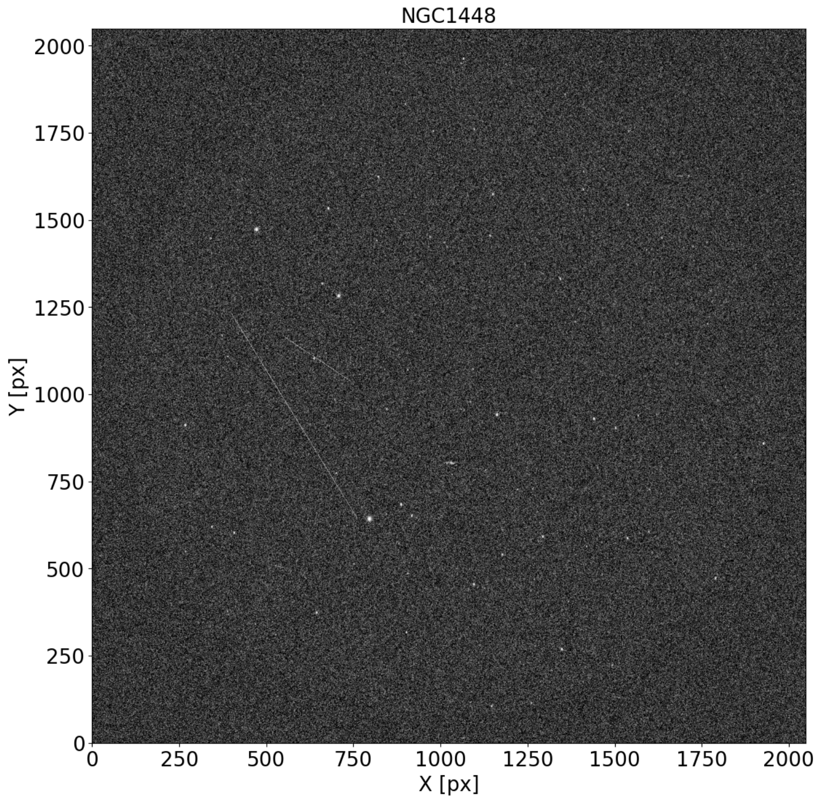

Figure 4.11.: Simulated differential frame for NGC1448 with moderate movement of the stars in the y direction

4.3. AOCS Information

4.3.1. Precision Requirements

In order to test the combined centroid performance, a simulated dataset based on 12 galaxies[6] was created. For each of the galaxies the dataset contains 200 image sets[7] with different positions and rotations of the field and varying satellite rotation rates (all 3 axes). An example of a differential frame used for the analysis is shown in Figure 4.11.

In light of the results from the Acquisition robustness analysis shown above, the simulated cases used for the analysis here are limited to those with a combined movement

[6] Simulated galaxies: NGC1232, NGC1433, NGC1448, NGC1515, NGC1527, NGC1559, NGC3556, NGC4051, NGC4800, NGC4826, NGC5377, NGC6207

[7] 1, 2−1, 3−2 frames needed for Acquisition

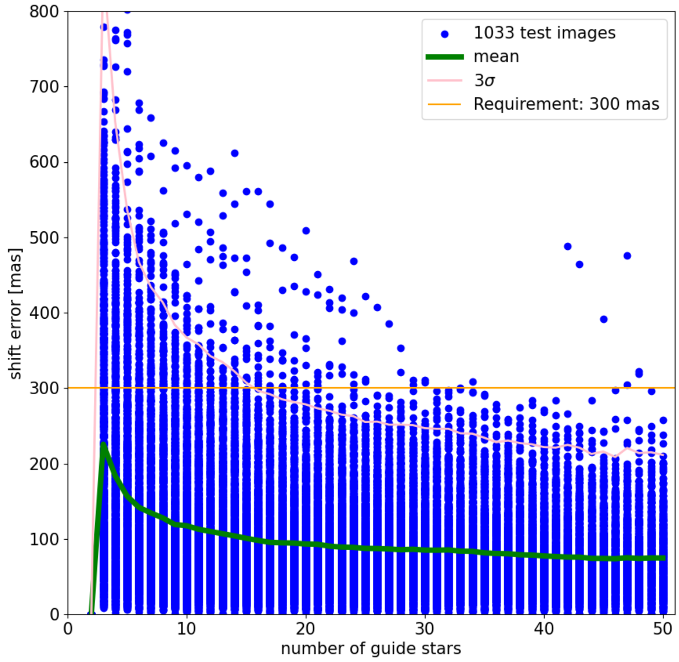

Figure 4.12.: Evolution of the satellite movement estimation error across the LoS with increasing number of guide stars

amplitude amp_{comb} of less than 3.6 px. amp_{comb} is calculated via Equation (4.1), where amp_{shift} is the amplitude of the shift across the LoS in pixel per second and amp_{rot} is the rotation amplitude in arcsec per second.

$$amp_{comb} = amp_{shift} + 1024 \cdot \sin \frac{amp_{rot}}{60^2} \tag{4.1}$$

This selection reduces the number of image sets to 1033. This is done in order to ensure that the results obtained here are not driven by a lack of guide stars found.

Once more, the Acquisition algorithm is instructed to find up to 50 guide stars. The movement error found is then re-computed multiple times by decreasing the number of guide stars used in the calculations. The stars with the lowest quality are excluded first. The following images show the evolution of the movement error with the blue dots representing individual results, the green line as the mean and the pink line as the 3σ envelope. The orange line(s) show the quality demanded by the requirements. The 3σ envelope of the across LoS error needs to be below 300 mas and the along LoS error below 30 arcsec, respectively. Figure 4.12 shows the development of the across LoS error and Figure 4.13 shows the along LoS error, respectively. For both components, 25 guide stars safely fulfill the requirements.

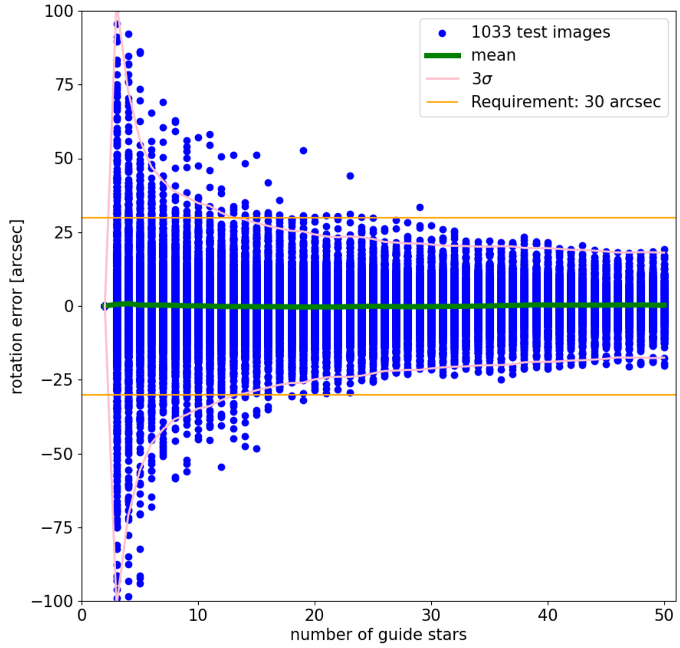

Figure 4.13.: Evolution of the satellite movement estimation error along the LoS with increasing number of guide stars

One of the most important results of this thesis is that,

the calculated AOCS information fulfills its precision requirements under nominal kinematic conditions.

4.3.2. Acquisition Quality

As described above, the number of guide stars is the main factor in AOCS information precision and the Acquisition quality is intended to provide additional insight. To verify this functionality, the same data set used for the AOCS information precision analysis is used again. The Acquisition quality is plotted against the across LoS error and the amplitude of the along LoS error. The amplitude is used for the along LoS error, because the error itself is scattered symmetrically around zero (see Figure 4.13).

First, the quality is plotted against the error for the case of 25 guide stars and a linear fit is performed to demonstrate the correlation. As shown in Figures 4.14a and 4.14b a correlation can be found, but it is not very strong (error of the slope parameter only about 1.5 to 2.5 times smaller than the best fit value). Due to the inclusion of the distance from the rotation axis in the Acquisition quality, the fit for the along LoS error is more certain.

The behavior over a range of guide star numbers is given in Figures 4.14c and 4.14d. The Figures demonstrate that the Acquisition quality is successful in capturing the trend of decreasing error with increasing number of guide stars.

The chosen approach for the Acquisition quality has been validated, because
a correlation between the AOCS information precision and the Acquisition quality parameter has been found.

4.3.3. Effect of Jitter

The NIR channels used for Guiding have a sampling period of ∼1.45 s per frame, resulting in up to ∼1.45 s between the read out of the different guide stars. When the spacecraft experiences jitter, the various guide stars will probe different parts of the jitter history. If the jitter has a short period, it will deform the Point Spread Function (PSF), which reduces the centroid and thus also afflict the AOCS information precision. However, when the period's magnitude is comparable to the frame time's one, the jitter will individually offset the position of the guide stars. The centroid combination may then incorrectly conclude this to be caused by an actual shift or rotation of the LoS.

In order to investigate the influence of long period jitters and the dependence of the introduced error on guide star distribution across the detector, simulations with the same set of mean motion, but different jitter periods and amplitudes are performed. The jitter included is perpendicular to the readout direction and is sine-shaped with a single frequency. For each simulation, the Acquisition is run with a limit of 25 guide stars. Heatmaps of the across and along LoS error in dependence of jitter period and amplitude are created. This is done for four different distributions of the guide stars. A demonstration image showing the difference between long and short period jitter is given in Figure 4.15.

The first case investigates an even distribution of guide stars across the detector. Here, the position based guide star quality component is constant, meaning the guide stars are selected based on the brightness and neighbor criteria only. The results are shown in Figure 4.16, the across LoS error being on the left side and the along LoS error on the right. The bottom row shows the same plots as the top one, but the color range's upper limit are the precision requirements. As expected, a larger jitter amplitude causes larger errors (lower Signal to Noise Ratio (SNR) and thus also fewer guide stars). A jitter frequency of 0.5 frame readout times produces the worst results, because the jitter offsets the guide stars in opposite directions on the two frames used for centroid calculation. Additionally, at a frequency of 1 frame readout time (or any other natural number) the error is considerably lower, because the stars experience the same jitter offset on both frames. The centroid combination then does not notice the jitter since the relative positions are the same. Furthermore, the error decreases with increasing jitter frequency as the individual oscillations become averaged out to a smearing of the PSF. At this point the smearing from the jitter combines with the one from the mean motion of the satellite and the error behaves similarly to the one described during the Acquisition robustness analysis above. This causes most of the data points with a jitter amplitude of > 1.5 px (3 px smear extend) to violate the precision requirements, as the used simulations

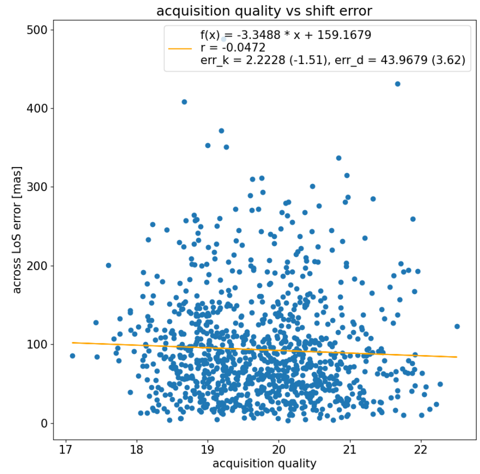

(a) Across LoS error for 25 guide stars

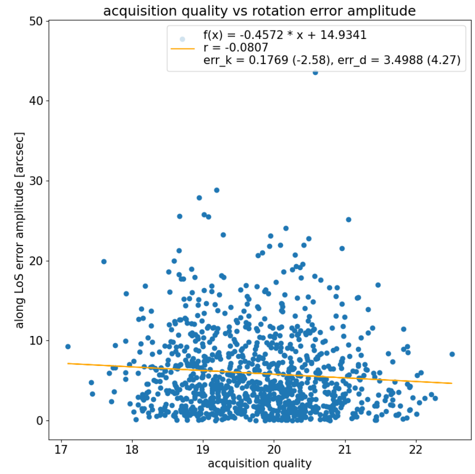

(b) Along LoS error for 25 guide stars

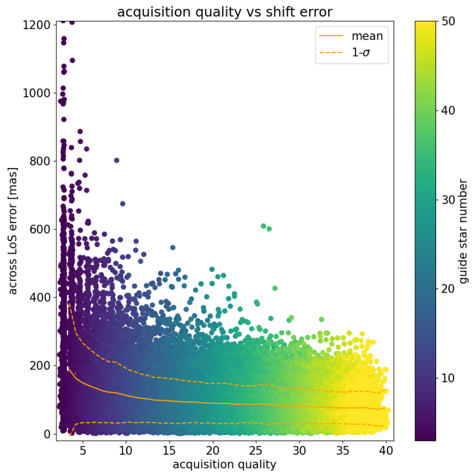

(c) Across LoS error for up to 50 guide stars

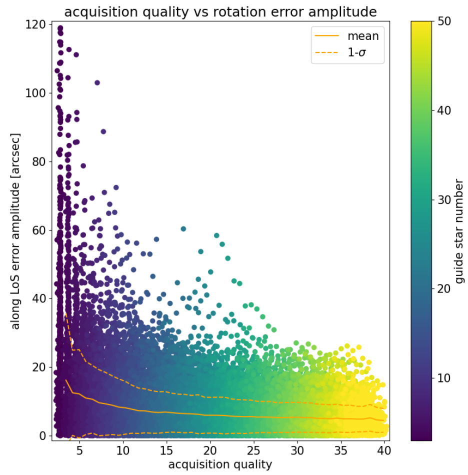

(d) Along LoS error for up to 50 guide stars

Figure 4.14.: Correlation between the Acquisition quality and across and along LoS error

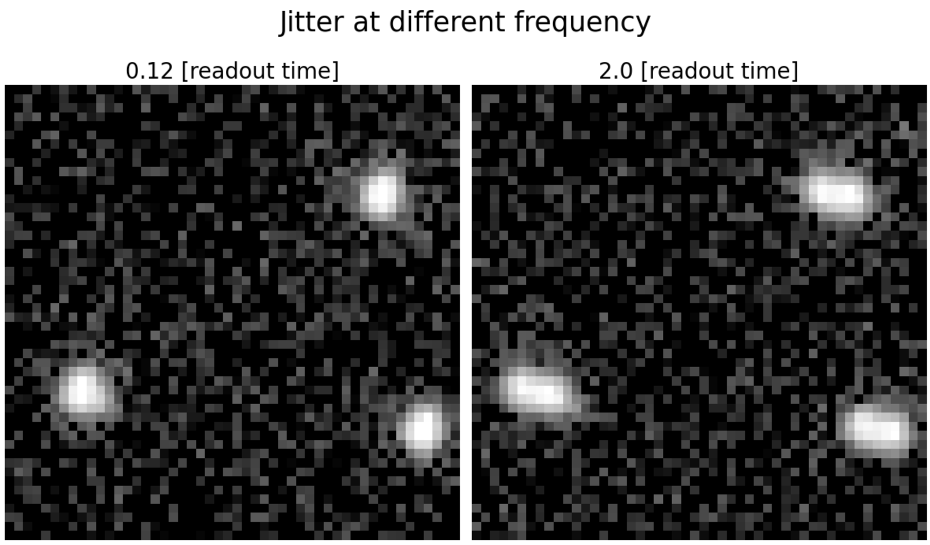

Figure 4.15.: Demonstration of the difference between long and short period jitter with an amplitude of 2 px on group of three stars found in the field of NGC1515. In both cases there is a identical nearly vertical drift movement. On the left, the jitter frequency is several times lower than the readout one, thus the influence of the jitter is hard to distinguish from the drift when observing a single image alone. In contrast on the right, the jitter frequency is twice the readout one and the stars light is clearly stretched perpendicular to the readout/drift direction.

also have a shift with > 1 px and rotation of $\sim$80 arcsec per Full Frame (FF).

For the next case, the guide star distribution is weighted in favor of the image bottom, meaning that the position based guide star quality component linearly increases from the detector's top to the bottom from 0 to 1. As a result, nearly all the stars are selected from the bottom half of the detector. Similar plots as for the previous case are shown in Figure 4.17. While the error found is comparable to the previous case on the high end, the number of jitter combinations where the requirements are fulfilled decreases significantly. The data points with a jitter amplitude of > 1.5 px have the same issue as before, but now only a few frequencies fulfill the requirements at low amplitudes ($<$1 px), whereas nearly all did previously. This is caused by a combination of effects. First, the average brightness/individual centroid precision is lower now, because bright stars previously selected are ignored due to their location. Second, since the guide stars are concentrated at the bottom, more of them experience a similar offset due to the jitter. Therefore, when the non-rotated positions and shifts are averaged during centroid combination, the result will be biased towards the direction of the jitter offset.

The third case restricts the guide stars to the bottom half of the image by jumping the position based quality component from -4 to 1 in the middle of the image. The setup used guarantees that any star in the image's upper half will have a negative quality, resulting in automatic rejection of the guide star candidate. The plots for this case are displayed in Figure 4.18. The results shown are similar to the even distribution over the whole detector, but the average errors are a bit higher. Once again, this is caused by the decrease in average guide star brightness, now simply due to the more limited search area. The similar offsets are a factor again, but less pronounced since the guide stars are at least more evenly distributed in the detector's bottom half.

At last, the equivalent mechanism of case three is used to restrict guide stars to the bottom quarter of the image. As can be seen in Figure 4.19 the error now exceeds the requirements in nearly all cases. The effects described above once again contribute to this, but the main factor here is the decreased number of guide stars found due to the smaller area allowed. For large jitter amplitudes, there now are some frequencies where insufficient numbers of guide stars are found to perform AOCS information calculation for all simulated cases.

In summary, from the perspective of jitter

a more even distribution of the guide stars across the detector is preferable to mitigate the larger impact of lower frequency jitters.

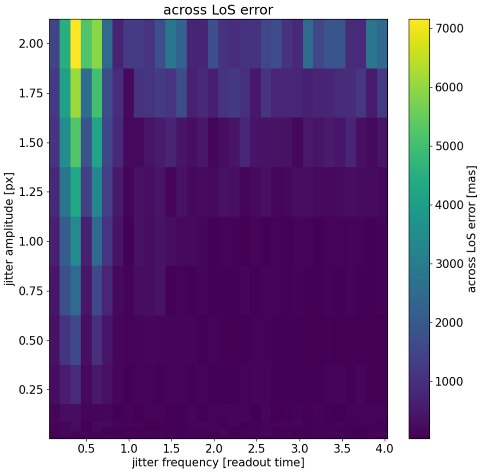

(a) Across LoS error, full value range

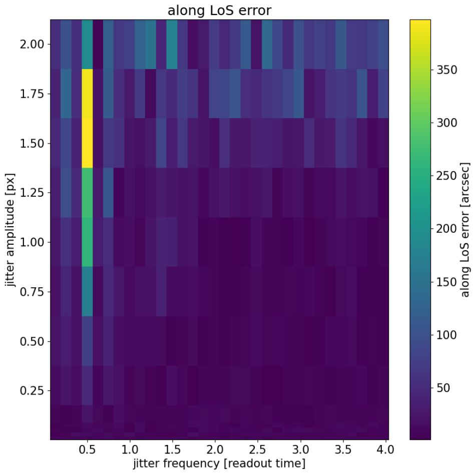

(b) Along LoS error, full value range

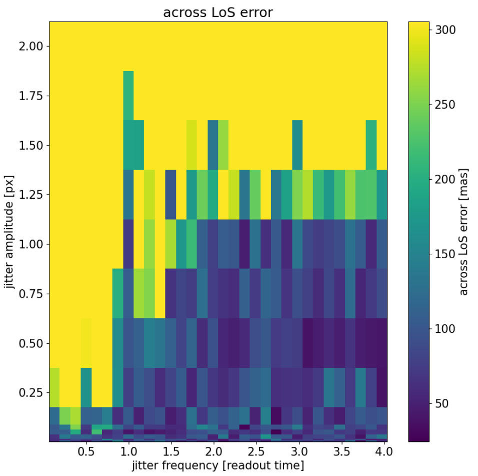

(c) Across LoS error, color range limited to requirement (300 mas)

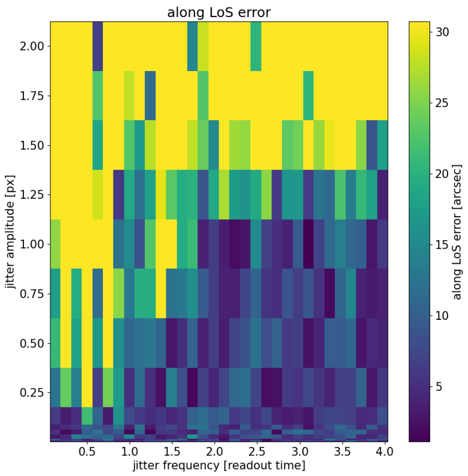

(d) Along LoS error, color range limited to requirement (30 arcsec)

Figure 4.16.: AOCS information error with different sine jitter amplitude and period for 25 evenly distributed guide stars selected from the entire detector

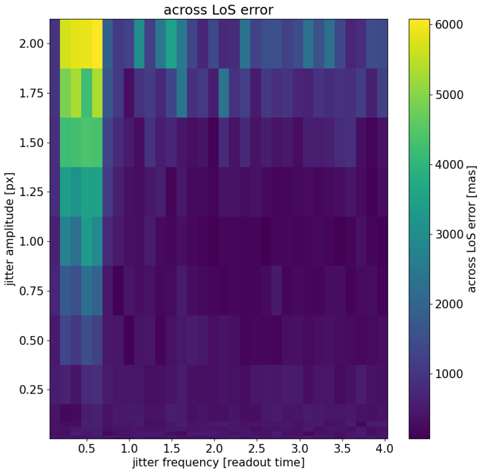

(a) Across LoS error, full value range

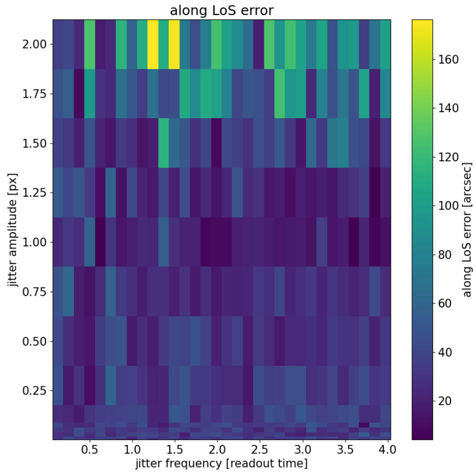

(b) Along LoS error, full value range

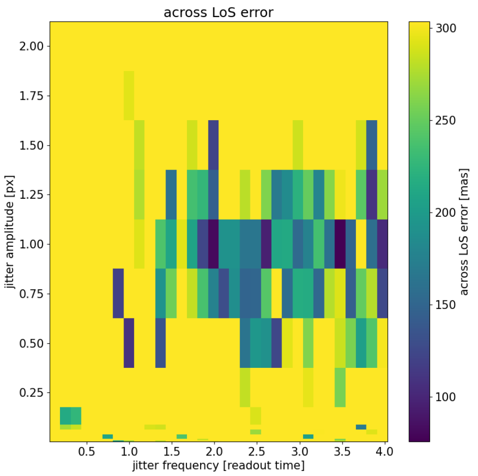

(c) Across LoS error, color range limited to requirement (300 mas)

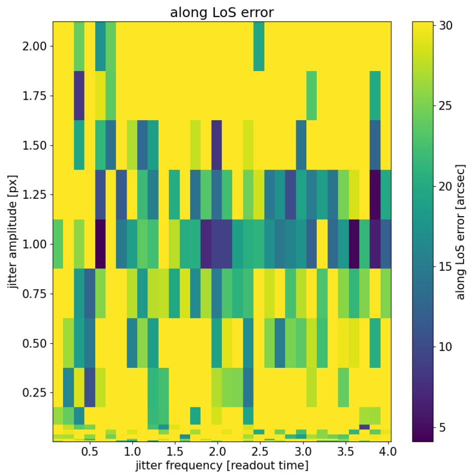

(d) Along LoS error, color range limited to requirement (30 arcsec)

Figure 4.17.: AOCS information error with different sine jitter amplitude and period for 25 guide stars preferentially selected from detector bottom

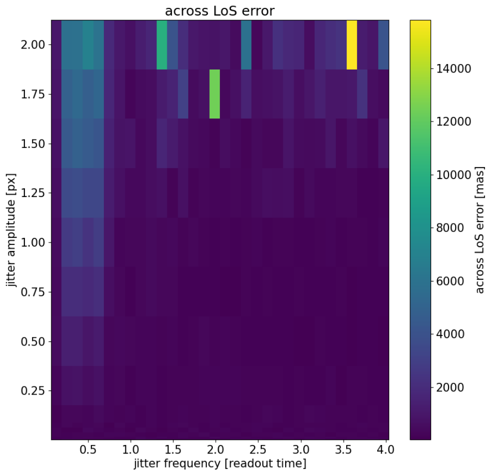

(a) Across LoS error, full value range

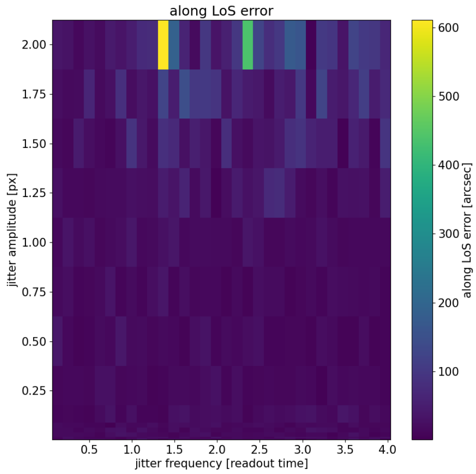

(b) Along LoS error, full value range

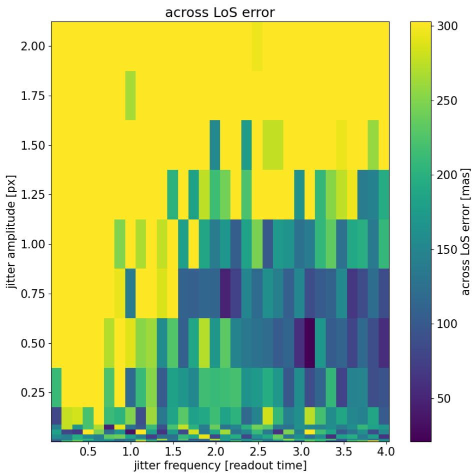

(c) Across LoS error, color range limited to requirement (300 mas)

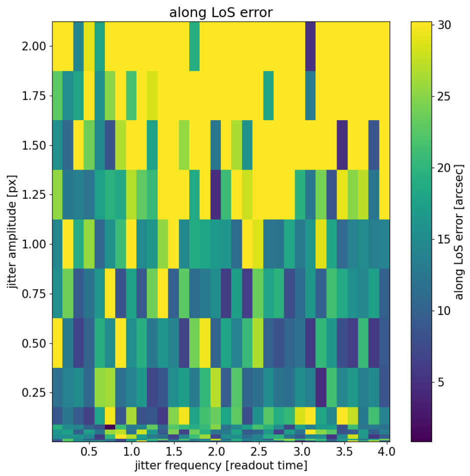

(d) Along LoS error, color range limited to requirement (30 arcsec)

Figure 4.18.: AOCS information error with different sine jitter amplitude and period for 25 evenly distributed guide stars selected from lower detector half

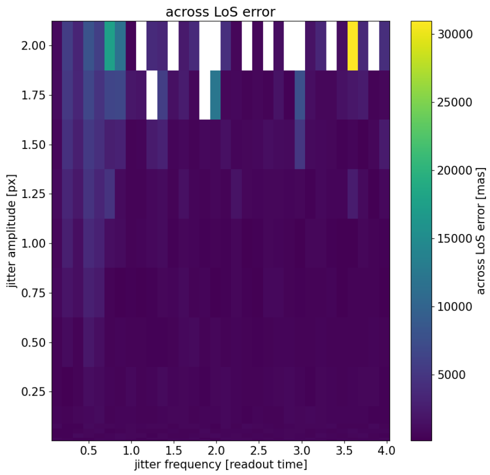

(a) Across LoS error, full value range

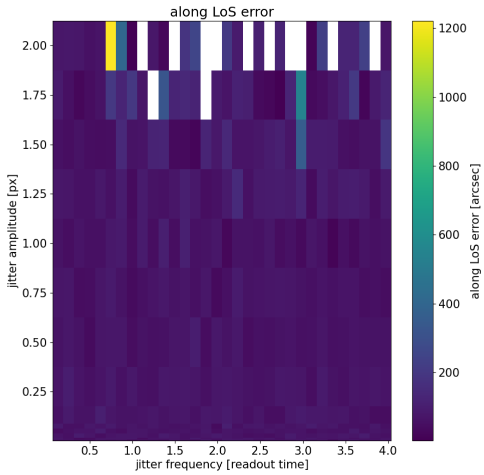

(b) Along LoS error, full value range

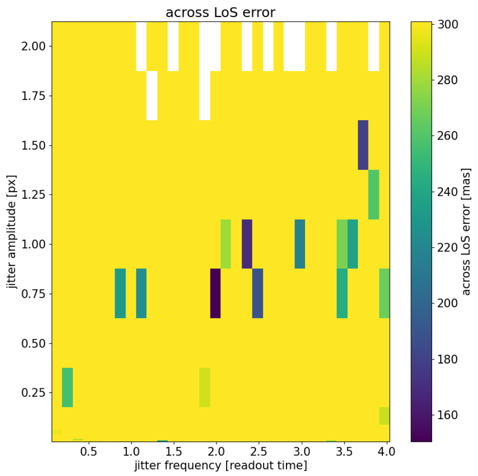

(c) Across LoS error, color range limited to requirement (300 mas)

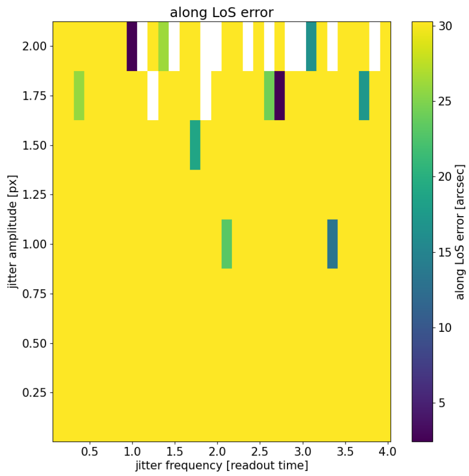

(d) Along LoS error, color range limited to requirement (30 arcsec)

Figure 4.19.: AOCS information error with different sine jitter amplitude and period for up to 25 evenly distributed guide stars selected from lower detector quarter

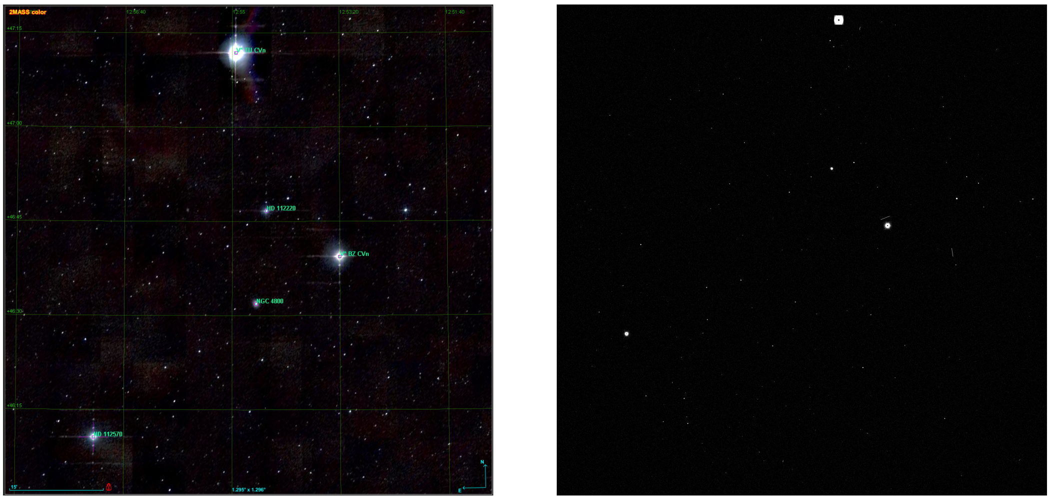

(a) 2MASS image from Aladin of NGC4800 with the bright stars labeled

(b) ARRAKIHS Simulator image of the surroundings of NGC4800

Figure 4.20.: Image of the surroundings of NGC4800 including the bright foreground stars.

4.3.4. Challenging Conditions

In the following, the performance of the Acquisition algorithm is shown for different challenging conditions. The cases of very bright stars inside the FoV and crowded region were initially identified during development and prompted adjustments to the algorithm.

Very Bright Stars Inside the FoV

The galaxy NGC4800 is part of the ARRAKIHS target pool (Consortium, 2025). As shown in Figure 4.20 there are four very bright foreground stars within the FoV.

With the initial implementation of the source extraction (not described in this thesis), the pixels in the flanks of these stars' PSFs took up the vast majority of the bright pixel count. As a result, only very few other stars were found and the AOCS information precision was accordingly bad. This led to the addition of the exclusion regions step during search area definition and the local maximum rule during bright pixel identification.

As can be seen in Figure 4.21 the modifications to the source extraction are successful in enabling the detection of many stars despite bright objects within the FoV and the precision is no longer afflicted.

Crowded Region

Near the galaxy NGC6207, which is part of the target pool (Consortium, 2025), the Hercules globular cluster (M13) is located and thus within the FoV as shown in 4.22.

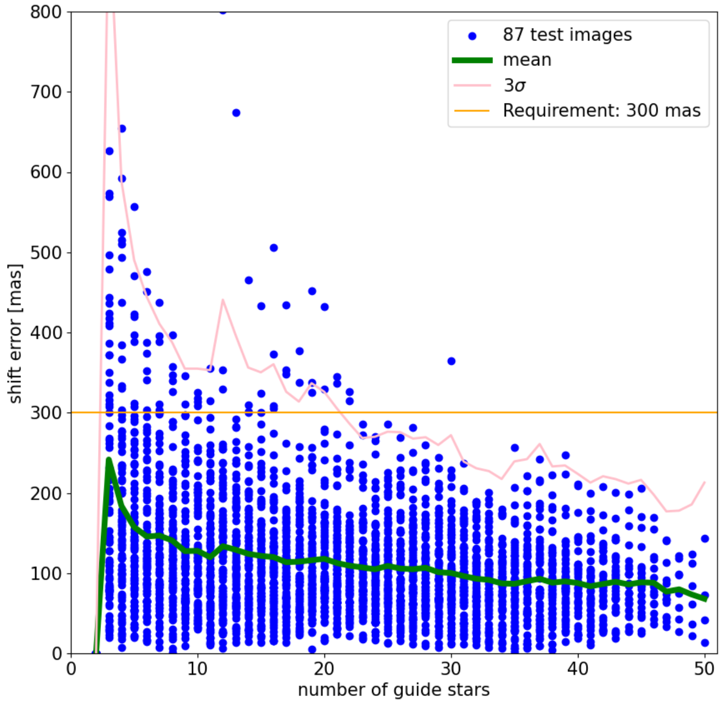

Figure 4.21.: Across LoS error evolution with guide star number for NGC4800, showing that sufficient stars can be found now

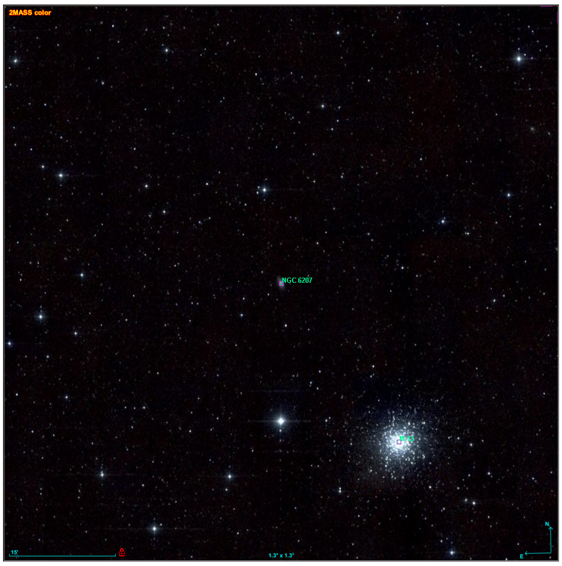

Figure 4.22.: Aladin image of the FoV for NGC6207 with the globular cluster M13 visible

Due to the large number of stars in the cluster, many of the guide star candidates are found there. Additionally, due to the high star density in the region of the cluster, it is common that additional stars are inside of or nearby the ROI of the guide stars. If a second star has comparable brightness to the actual candidate, it happens that the IWC step of the centroid calculation jumps to the different one, thus introducing a very large error in the AOCS information. In order to prevent this, the rules rejecting guide star candidates with second sources of half/equal brightness inside/nearby the ROI were implemented.

The adopted rules are capable of resolving this issue. While Figure 4.23a shows that many guide stars are still selected in the area of the cluster, they are now predominantly in the less dense outskirts. The few stars selected close to the cluster center have sufficiently higher signal to ensure correct detection by the IWC step. Additionally, Figure 4.23b demonstrates that the AOCS information precision requirement is now fulfilled with the standard 25 guide stars.

Many Hot Pixels

One open question is the performance of the algorithm in the presence of many hot pixels. To test this, a data set is created with increasing hot pixel fraction for eight galaxies[8] and five rotation rate sets. Images showing the impact of the increasing hot pixel fraction are shown in Figure 4.24.

[8] Simulated galaxies: NGC1232, NGC1433, NGC1448, NGC1515, NGC4051, NGC4800, NGC4826, NGC5377

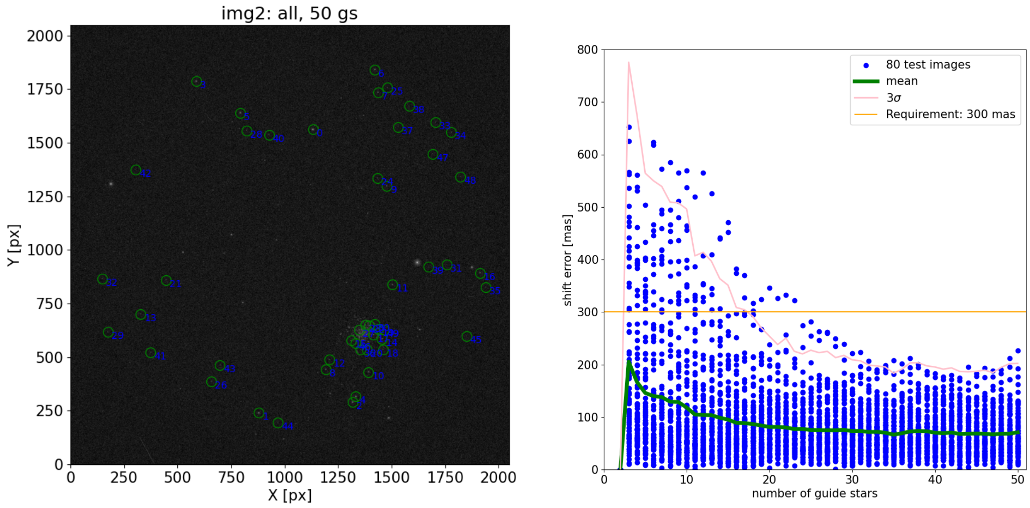

(a) Selected guide stars shown on second differential image for NGC6207

(b) Across LoS error for NGC6207

Figure 4.23.: Acquisition performance analysis for NGC6207

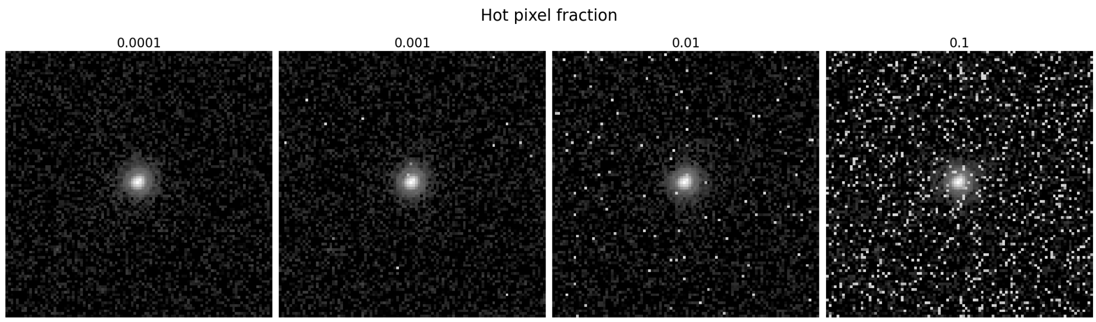

Figure 4.24.: Cutout of differential images for NGC1515 showing a bright star with the hot pixel fraction increasing from 10^{-4} to 0.1

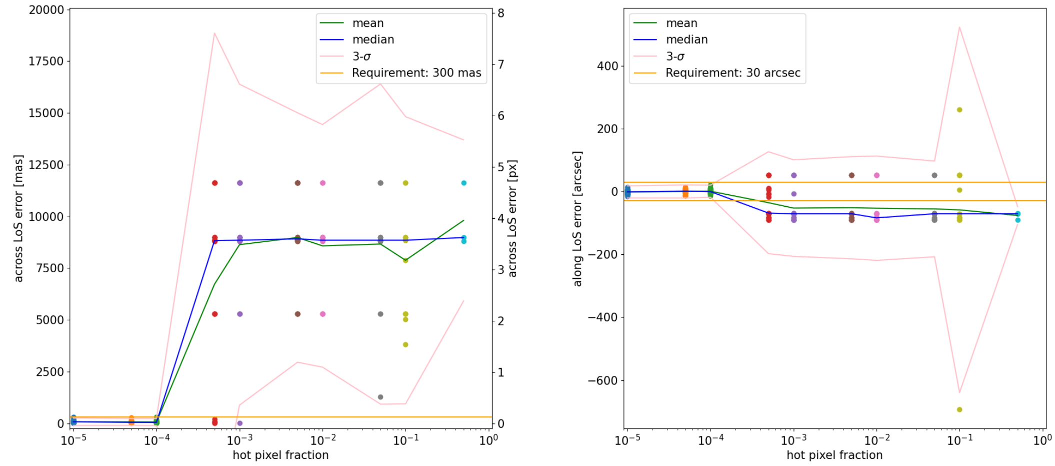

(a) Across LoS error evolution with hot pixel fraction

(b) Along LoS error evolution with hot pixel fraction

Figure 4.25.: Across and along LoS error with increasing hot pixel fraction for the standard Acquisition setup

The along and across LoS error with the standard Acquisition setup is measured, as seen in Figure 4.25. At a hot pixel fraction of 0.05% and above, the algorithm fails to find sufficient stars to perform any calculations (minimum of 2 needed) in nearly all cases. The cutoff point is as expected, because $0.0005 \cdot 2048^2 \approx 2100$, which is more than twice the number of bright pixels considered during source extraction. This is due to a large portion of those bright pixels being taken up by the hot pixels. The problem is compounded by failed centroid validations, caused by the IWC being drawn to the hot pixels as well. As a result, only very bright stars are occasionally found.

The analysis shown does not include any attempts to mitigate the hot pixels. Onboard the satellite, a hot pixel mask will be available. Using the mask, the simplest mitigation approach is to set the values of the known hot pixels to zero in both the raw and the two differential FFs. The thus considerably improved performance can be seen in Figure 4.26. The error now starts violating the requirements at 1% hot pixel fraction (20 times previous). The increase in error now is more gradual, too, and no longer caused by a lack of guide stars found, but by a decrease in centroid precision due to the holes in the data.

While the hot pixel mitigation technique used here is capable of providing satisfactory improvements for the precision of the Acquisition's AOCS information, analyses to be carried out in the future will need to verify if this is also the case for the Guiding. There the risk exists, that a guide stars moves close to or onto a hot pixel, thus disrupting the centroids. If the same thing happens during Acquisition, the star is simply not chosen as

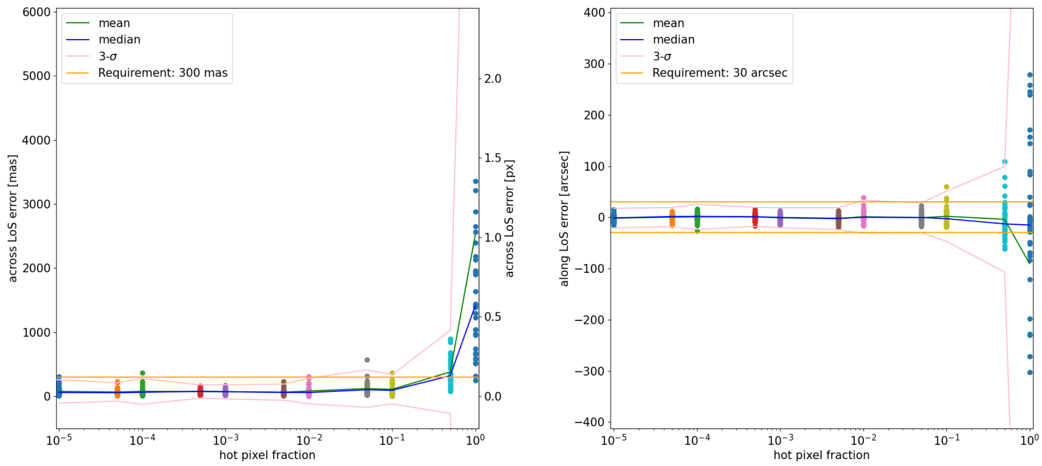

(a) Across LoS error evolution with hot pixel fraction

(b) Along LoS error evolution with hot pixel fraction

Figure 4.26.: Across and along LoS error with increasing hot pixel fraction when setting hot pixels to zero using a hot pixel mask

a guide star.

Another approach for correction of the hot pixels would be the application of a median filter. In the case of ARRAKIHS a median filter cannot be easily applied, because of the small size of the PSF. The filter would remove large portions of the signal. Additionally, applying a median filter to the entire area of a FF is prohibitively expansive computation wise.

One last thing to note is the difference between configured hot pixel fraction and the image's actual one. The hot pixel fractions shown in the plots above are the values configured for the simulator. The simulator calculates the maximum number of hot pixels from the image size and the provided fraction and then places them by performing that many random pixel selections. The selected pixels get the additional hot pixel signal assigned to them. The algorithm does not repeat the pixel selection if the pixel is already a hot pixel. Therefore, for very large hot pixel fractions, the number of actual hot pixels is lower than configured. The ratio between the configured and true hot pixel fractions is shown in Figure 4.27. The Figure shows that up to a hot pixel fraction of 10%, more than 95% of the configured hot pixels are actually placed. The ratio then decreases to less than 65% for 100% hot pixel fraction.

Since the number of hot pixels increases over a detector's lifetime, this point may need to be revisited, once more information about the detectors' predicted end of life conditions

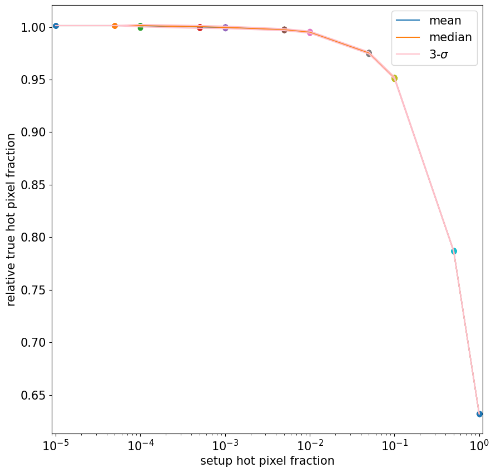

Figure 4.27.: Ratio of true to configured hot pixel fraction

for ARRAKIHS becomes available.

Rotation Axis Position Error

Another potential error source for the AOCS information is the difference between the user-configured and actual rotation axis location. To test this, the Acquisition algorithm is run repeatedly on the same data set used for the AOCS information precision analysis, while the configured location of the rotation axis is varied by up to 40 px per axis. The across and along LoS error, including the 3σ envelope, are evaluated for 25 guide stars and shown in Figure 4.28. The across LoS measurement starts to violate the requirements for a location error of greater than 45 px. The along LoS measurement's 3σ envelope increases by less than a percent over the entire range tested.

This behavior is caused by a combination of factors. First, the default configuration uses an inner circular boundary of 512 px, as a result the distance from rotation axis to the stars is large compared to the rotation axis location error. Therefore, the error in rotation angle is small[9]. Additionally, the angle errors for stars on opposite sides of the rotation axis have inverse signs. As a result, the angle averaging step during centroid combination removes a large part of the error. The combined impact of these two effects causes the along LoS measurement to be only minimally impacted only by the rotation axis position error.

[9] For an axis location error of 40 px in one axis and a star on the inner 512 px boundary, the angle error is less than 8%

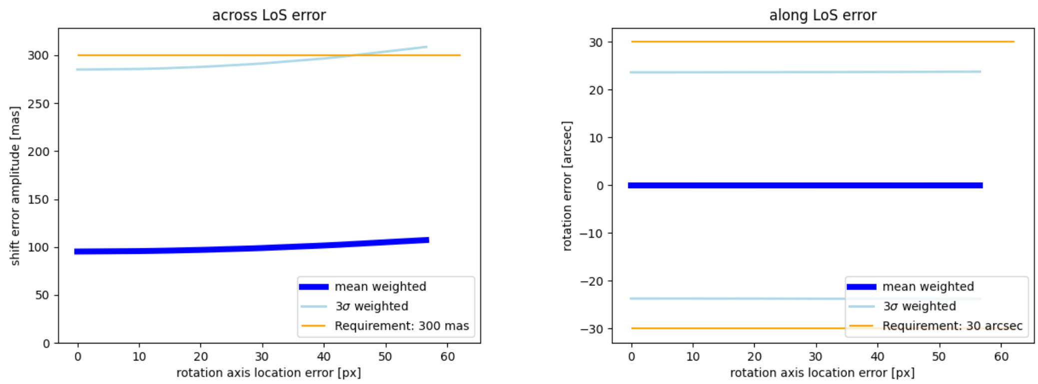

(a) Across LoS error

(b) Along LoS error

Figure 4.28.: Evolution of AOCS information error for 25 guide star with rotation axis position error

The across LoS measurement is impacted more, because the AOCS information calculation uses the final along LoS rotation angle guess to de-rotate the new positions using the given rotation axis. The incorrect rotation axis causes all stars to be offset by the same distance and direction. This offset is then included in the across LoS guess.

The analyses show that,

the developed algorithm is successful under challenging conditions identified during the development process.

4.4. Requirements for the Platform

By combining the results of all the analyses performed in this thesis, requirements for the platform can be formulated in order to exclude scenarios where the Acquisition is incapable of fulfilling its requirements.

One additional aspect not yet covered by the analyses it the combination of the across and along LoS components. In the worst case a star is located at the edge of the FoV (maximum along LoS deviation for same angle θ) such that both contributions move it in the exact same direction. Thus the total deviation $D_{\text{total, worst case}}$ of the star can be calculated from the across LoS one D_{across} (by combining the x and y axis components D_x and D_y) and the along LoS one $D_{\text{along, FoV edge}}(\theta)$ via Equation (4.2).

$$D_{\text{total, worst case}} \leq D_{\text{across}} + D_{\text{along, FoV edge}}(\theta) = \sqrt{D_x^2 + D_y^2} + D_{\text{along, FoV edge}}(\theta) \quad (4.2)$$

To ensure that the Acquisition is successful regardless of the exact layout of the used guide stars, the across LoS requirements are corrected by the determined along LoS ones under the worst case assumptions. The new across requirement $\mu_{\text{across, corrected}}$ is calculated from the original one μ_{across} and the along one μ_{along} following the derivation in Equation (4.5).

$$\mu_{\text{across}}["] = \mu_{\text{across, corrected}}["] + R_{\text{FoV}}[\text{px}] \cdot \sin(\frac{\mu_{\text{along}}["]}{60^2} \cdot \frac{\pi}{180}) \cdot \text{plate scale } ["/\text{px}] \quad (4.3)$$

$$\mu_{\text{across}}["] = \mu_{\text{across, corrected}}["] + \frac{\mu_{\text{along}}["]}{88} \text{ (small angle approximation)} \quad (4.4)$$

$$\mu_{\text{across, corrected}} = \mu_{\text{across}} - \frac{\mu_{\text{along}}}{88} \quad (4.5)$$

In Section PDE Transition to Guiding no PDE along LoS was formulated. After discussion with other consortium and ESA members (team members, 2025), it was decided to also use the PDE along LoS during Acquisition for the transition, because the satellite platform will already need to fulfill the requirement during Acquisition without assistance of the FGS and thus represents no additional constraint.

Lastly a approximately 10 percent margin is applied to all requirements to ensure they remain valid during the further development process of ARRAKIHS.

The requirements are summarized in Table 4.2.

Table 4.2.: Overview of the calculations for the requirements intended for the satellite platform to ensure that Acquisition is successful

Requirement	Initial ["]	Corrected ["]	Margined ["]	Reference
PDE across LoS during Acquisition half-cone angle over 1.45 s	9.92	8.78	7.5	see wrt Drift
PDE along LoS during Acquisition half-cone angle over 1.45 s	100	100	90	see wrt Rotation
RPE across LoS during Acquisition half-cone angle over 1.45 s at 3σ	11.75	11.75	10.5	see worst Case
PDE across LoS transition to Guiding half-cone angle over 6.0 s	17.36	16.22	14.0	see PDE Transition to Guiding
PDE along LoS transition to Guiding half-cone angle over 6.0 s	-	100	90	see above

Pointing requirements for the satellite platform intended to ensure successful Acquisition could be formulated.

4.5. Timing

One important point still left to verify is, whether the algorithms developed during this thesis are actually capable of completing their calculations on time, when using representative hardware. The hardening of satellite's computer hardware against radiation, causes it to be significantly slower than non-hardened contemporary hardware. For example, the GR740 processor to be used by ARRAKIHS is planned to be operated at 250 MHz (team members, 2025), while the laptop used for large parts of this thesis operates at 2.1 GHz. Additionally, longer RAM access times contribute to the slowdown, too.

During testing, the algorithm is considered sufficiently fast if the calculation of the AOCS information (last step) completes before the end of the readout of the fourth FF ($\approx 4 \cdot 1.45\,\mathrm{s} = 5.8\,\mathrm{s}$). As described in Sequencing, the algorithm needs to finish before the end of the fourth frame/reset in order to allow switching to Guiding without an additional delay of one readout cycle.

The algorithm execution time analysis is performed on a GR740 evaluation board [a GR740 will be used on ARRAKIHS (team members, 2025)]. The processor is set up with the same frequency and memory configuration as currently planned for ARRAKIHS. Therefore, the setup very closely represents the performance of the actual hardware to be used. The Acquisition algorithm and the three images (1st raw and 2 differential FFs) are compiled into one executable and uploaded to the hardware. The total execution time copying the images from their static arrays, needed for compiling, into arrays, usable for calculation, is not included in the execution time analysis, because this step will not occur on the satellite. There, the images will be read from the detectors. Additionally, the time measured for the calculation and printing of the execution is also subtracted for each step.

In the worst case, calculations can only start after the complete frame has been readout. A runtime analysis for this case is shown in Figure 4.29. Phase 0 are steps related to the first raw FF, Phase 1 and 2 are steps related to the first and second differential FFs and Phase 3 is the AOCS information calculation. As can be seen in the Figure, the majority of calculation time is used by the source extraction, especially the image binning (bin)[10], bright pixel search (brpx), candidate determination (cand) and quality calculation (qual). The centroid calculations (phase1 and ph2ref) take little time, as expected. Even in the worst case, the algorithm finishes in time (about halfway through the fourth frame/reset).

On the actual satellite's hardware, image rows will become available as soon as they are read out, therefore steps like the exclusion area definition (exc_def), binning (bin),

[10] Due to the small size of the PSF the binning factor used for all analyses in this thesis is one (no binning). Despite this, the binning cannot be skipped, because the binned image array is 32-bit instead of 16-bit like the images and therefore the further calculations expect a 32-bit array. The reason for the 32-bit format is that the binning is done via addition not averaging in order to preserve the signal, which is needed for brightness determination during reset slot assignment.

bright pixel search (brpx) and centroiding (ph2ref)[11] could be carried out as soon as the data becomes available. A modified execution time analysis with this in mind is shown in Figure 4.30. The execution times from the worst case analysis were shifted so that the parallelize-able steps mentioned finish together with the frame readout. Additionally, it is assumed that bin and brpx can be carried out in parallel, because there are multiple CPU cores and no science data processing is ongoing during the Acquisition. As can be seen in the Figure, the calculations now finish more than half a second earlier. Depending on the layout of the guide stars on the detector, the Phase 2 centroiding step (ph2ref) could actually finish before the readout of the second differential FF is complete.

In both scenarios presented, the Acquisition algorithm finishes its calculations safely in time. Additionally, the implementation of the algorithms developed during this thesis is not yet optimized for the GR740, since the focus of this thesis is the correct functionality of the algorithms, so any other performance tests except this timing one have been carried out on a laptop or server. Therefore, the execution time shown here should be considered as an upper limit, with future developments expected to significantly reduce it.

As demonstrated on representative hardware,

> the execution time of the algorithms developed is fast enough even under worst case conditions.

[11] The exact timing for the centroiding will depend on the location of the guide star candidates.

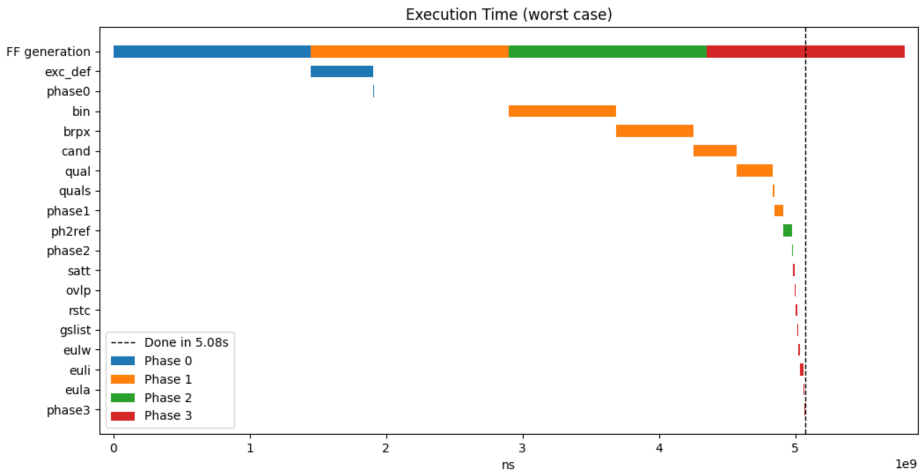

Figure 4.29.: Execution time analysis for the worst case when calculations can only start after the frame readout is finished.

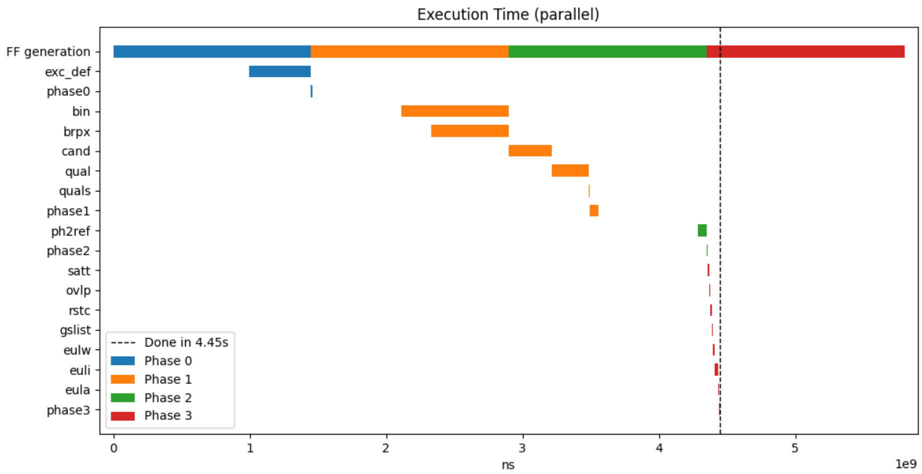

Figure 4.30.: Execution time analysis for the scenario when calculations are carried out in parallel as soon as the image rows become available.

5. Conclusion

In the scope of this thesis, the current development status of the Acquisition algorithm for the FGS of ARRAKIHS has been presented. The performance analyses showed that the implementation is capable of achieving the precision requirements given for a wide range of kinematic conditions. Additionally, four pointing requirements for the spacecraft platform have been formulated, which should ensure successful Acquisition.

The Acquisition takes one raw and two differential FFs as input. From the first differential one, star candidate positions are extracted using an approach similar to Bertin and Arnouts (1996). For both differential frames and all candidates, centroids are calculated identically to the approach from ARIEL by combining an IWC with iterative IWCoG steps. The remaining cosmic contamination after source extraction has been shown to be successfully removed by using the centroid validation to only select stars with valid centroids in both differential frames. After the final guide stars are selected, their two sets of centroids are combined into a single 3-axis AOCS information. The developed approach of splitting the satellite's rotation into along and across LoS by considering the change in relative position of the stars and refining the results iteratively has proven quite effective.

The Acquisition performance has been tested for various conditions. The ability to find sufficient guide stars to fulfill the AOCS information precision requirements has been shown for a wide range of residual motions. The points where the Acquisition starts to fail have been identified and pointing requirements for the platform have been formulated to prevent their occurrence.

The execution time of the current implementation has also been tested on representative hardware. The algorithm has been shown to be sufficiently fast even when starting calculations only after the whole frame has been readout and using only a single core.

One last point to note is that the implementation presented in this thesis is not the final version to be actually used on ARRAKIHS. With a planned launch in 2030, there will be further improvements. Several potential changes already envisioned are mentioned below:

- The Simulator developed during this thesis, while presently sufficient, will need to be expanded to facilitate the extensive Guiding simulations to be conducted. The current version is not sufficiently customizable and not all variables are stored in configuration files. Important features that are currently missing are the ability to only simulate the guiding windows and also include their reset cycles.

- At present, the maximum number of window resets allowed per readout cycle is still undefined. Thus, the analyses were carried out with a pessimistic value of 2. Should it turn out that the actual number is considerably higher, the current relatively complex reset slot assignment approach could be replaced with a simpler version.
- The current implementation does not attempt to subtract the relative shift of the guide stars caused by the residual drift that is encoded in the Acquisition lock. If long term Guiding simulations show this to be problematic, an additional step propagating the reference position based on the movement found between the first differential FF and the second one could be added.
- The actual power spectrum of the jitter is currently unknown. Once it becomes available, the influence of jitter analysis will need to be revisited. Depending on the findings of this analysis, the position component of the guide star quality may need to be upgraded from the current simple linear function to something more complex.

Bibliography

ARRAKIHS Consortium. Organization - ARRAKIHS Mission, 2025. URL https://www.arrakihs-mission.eu/organization/. accessed 09.08.2025.

ARRAKIHS Project Team. ESA-ARK-MIS-RS-001, ARRAKIHS Mission Requirement Document, 09 2024a.

ARRAKIHS Project Team. ESA-ARK-SYS-RS-001, ARRAKIHS Payload Interface Requirement Document, 04 2024b.

Astropy Collaboration, T. P. Robitaille, E. J. Tollerud, P. Greenfield, M. Droettboom, E. Bray, T. Aldcroft, M. Davis, A. Ginsburg, A. M. Price-Whelan, W. E. Kerzendorf, A. Conley, N. Crighton, K. Barbary, D. Muna, H. Ferguson, F. Grollier, M. M. Parikh, P. H. Nair, H. M. Unther, C. Deil, J. Woillez, S. Conseil, R. Kramer, J. E. H. Turner, L. Singer, R. Fox, B. A. Weaver, V. Zabalza, Z. I. Edwards, K. Azalee Bostroem, D. J. Burke, A. R. Casey, S. M. Crawford, N. Dencheva, J. Ely, T. Jenness, K. Labrie, P. L. Lim, F. Pierfederici, A. Pontzen, A. Ptak, B. Refsdal, M. Servillat, and O. Streicher. Astropy: A community Python package for astronomy. *A&A*, 558:A33, October 2013. doi: 10.1051/0004-6361/201322068.

Astropy Collaboration, A. M. Price-Whelan, B. M. Sipőcz, H. M. Günther, P. L. Lim, S. M. Crawford, S. Conseil, D. L. Shupe, M. W. Craig, N. Dencheva, A. Ginsburg, J. T. Vand erPlas, L. D. Bradley, D. Pérez-Suárez, M. de Val-Borro, T. L. Aldcroft, K. L. Cruz, T. P. Robitaille, E. J. Tollerud, C. Ardelean, T. Babej, Y. P. Bach, M. Bachetti, A. V. Bakanov, S. P. Bamford, G. Barentsen, P. Barmby, A. Baumbach, K. L. Berry, F. Biscani, M. Boquien, K. A. Bostroem, L. G. Bouma, G. B. Brammer, E. M. Bray, H. Breytenbach, H. Buddelmeijer, D. J. Burke, G. Calderone, J. L. Cano Rodríguez, M. Cara, J. V. M. Cardoso, S. Cheedella, Y. Copin, L. Corrales, D. Crichton, D. D'Avella, C. Deil, É. Depagne, J. P. Dietrich, A. Donath, M. Droettboom, N. Earl, T. Erben, S. Fabbro, L. A. Ferreira, T. Finethy, R. T. Fox, L. H. Garrison, S. L. J. Gibbons, D. A. Goldstein, R. Gommers, J. P. Greco, P. Greenfield, A. M. Groener, F. Grollier, A. Hagen, P. Hirst, D. Homeier, A. J. Horton, G. Hosseinzadeh, L. Hu, J. S. Hunkeler, Ž. Ivezić, A. Jain, T. Jenness, G. Kanarek, S. Kendrew, N. S. Kern, W. E. Kerzendorf, A. Khvalko, J. King, D. Kirkby, A. M. Kulkarni, A. Kumar, A. Lee, D. Lenz, S. P. Littlefair, Z. Ma, D. M. Macleod, M. Mastropietro, C. McCully, S. Montagnac, B. M. Morris, M. Mueller, S. J. Mumford, D. Muna, N. A. Murphy, S. Nelson, G. H. Nguyen, J. P. Ninan, M. Nöthe, S. Ogaz, S. Oh, J. K. Parejko, N. Parley, S. Pascual, R. Patil, A. A. Patil, A. L. Plunkett, J. X. Prochaska, T. Rastogi, V. Reddy Janga, J. Sabater, P. Sakurikar, M. Seifert, L. E. Sherbert, H. Sherwood-Taylor, A. Y. Shih, J. Sick, M. T.

Silbiger, S. Singanamalla, L. P. Singer, P. H. Sladen, K. A. Sooley, S. Sornarajah, O. Streicher, P. Teuben, S. W. Thomas, G. R. Tremblay, J. E. H. Turner, V. Terrón, M. H. van Kerkwijk, A. de la Vega, L. L. Watkins, B. A. Weaver, J. B. Whitmore, J. Woillez, V. Zabalza, and Astropy Contributors. The Astropy Project: Building an Open-science Project and Status of the v2.0 Core Package. *AJ*, 156(3):123, September 2018. doi: 10.3847/1538-3881/aabc4f.

Astropy Collaboration, Adrian M. Price-Whelan, Pey Lian Lim, Nicholas Earl, Nathaniel Starkman, Larry Bradley, David L. Shupe, Aarya A. Patil, Lia Corrales, C. E. Brasseur, Maximilian N"othe, Axel Donath, Erik Tollerud, Brett M. Morris, Adam Ginsburg, Eero Vaher, Benjamin A. Weaver, James Tocknell, William Jamieson, Marten H. van Kerkwijk, Thomas P. Robitaille, Bruce Merry, Matteo Bachetti, H. Moritz G"unther, Thomas L. Aldcroft, Jaime A. Alvarado-Montes, Anne M. Archibald, Attila B'odi, Shreyas Bapat, Geert Barentsen, Juanjo Baz'an, Manish Biswas, M'ed'eric Boquien, D. J. Burke, Daria Cara, Mihai Cara, Kyle E. Conroy, Simon Conseil, Matthew W. Craig, Robert M. Cross, Kelle L. Cruz, Francesco D'Eugenio, Nadia Dencheva, Hadrien A. R. Devillepoix, J"org P. Dietrich, Arthur Davis Eigenbrot, Thomas Erben, Leonardo Ferreira, Daniel Foreman-Mackey, Ryan Fox, Nabil Freij, Suyog Garg, Robel Geda, Lauren Glattly, Yash Gondhalekar, Karl D. Gordon, David Grant, Perry Greenfield, Austen M. Groener, Steve Guest, Sebastian Gurovich, Rasmus Handberg, Akeem Hart, Zac Hatfield-Dodds, Derek Homeier, Griffin Hosseinzadeh, Tim Jenness, Craig K. Jones, Prajwel Joseph, J. Bryce Kalmbach, Emir Karamehmetoglu, Mikolaj Kaluszy'nski, Michael S. P. Kelley, Nicholas Kern, Wolfgang E. Kerzendorf, Eric W. Koch, Shankar Kulumani, Antony Lee, Chun Ly, Zhiyuan Ma, Conor MacBride, Jakob M. Maljaars, Demitri Muna, N. A. Murphy, Henrik Norman, Richard O'Steen, Kyle A. Oman, Camilla Pacifici, Sergio Pascual, J. Pascual-Granado, Rohit R. Patil, Gabriel I. Perren, Timothy E. Pickering, Tanuj Rastogi, Benjamin R. Roulston, Daniel F. Ryan, Eli S. Rykoff, Jose Sabater, Parikshit Sakurikar, Jes'us Salgado, Aniket Sanghi, Nicholas Saunders, Volodymyr Savchenko, Ludwig Schwardt, Michael Seifert-Eckert, Albert Y. Shih, Anany Shrey Jain, Gyanendra Shukla, Jonathan Sick, Chris Simpson, Sudheesh Singanamalla, Leo P. Singer, Jaladh Singhal, Manodeep Sinha, Brigitta M. SipHocz, Lee R. Spitler, David Stansby, Ole Streicher, Jani Šumak, John D. Swinbank, Dan S. Taranu, Nikita Tewary, Grant R. Tremblay, Miguel de Val-Borro, Samuel J. Van Kooten, Zlatan Vasovi'c, Shresth Verma, Jos'e Vin'icius de Miranda Cardoso, Peter K. G. Williams, Tom J. Wilson, Benjamin Winkel, W. M. Wood-Vasey, Rui Xue, Peter Yoachim, Chen Zhang, Andrea Zonca, and Astropy Project Contributors. The Astropy Project: Sustaining and Growing a Community-oriented Open-source Project and the Latest Major Release (v5.0) of the Core Package. *ApJ*, 935(2):167, August 2022. doi: 10.3847/1538-4357/ac7c74.

Matthieu Baumann, Thomas Boch, François-Xavier Pineau, Pierre Fernique, Caroline Bot, and Mark Allen. Aladin Lite v3: Behind the Scenes of a Major Overhaul. In Jose Enrique Ruiz, Francesco Pierfedereci, and Peter Teuben, editors, *Astronomical*

Data Analysis Software and Systems XXX, volume 532 of *Astronomical Society of the Pacific Conference Series*, page 7, July 2022.

S. Behnel, R. Bradshaw, C. Citro, L. Dalcin, D.S. Seljebotn, and K. Smith. Cython: The best of both worlds. *Computing in Science Engineering*, 13(2):31 –39, march-april 2011. ISSN 1521-9615. doi: 10.1109/MCSE.2010.118.

E. Bertin and S. Arnouts. SExtractor: Software for source extraction. *Astronomy and Astrophysics Supplement Series*, 117:393–404, June 1996. ISSN 0365-01380004-6361. doi: 10.1051/aas:1996164. URL https://ui.adsabs.harvard.edu/abs/1996A&AS..117..393B. ADS Bibcode: 1996A&AS..117..393B.

T. Boch and P. Fernique. Aladin Lite: Embed your Sky in the Browser. In N. Manset and P. Forshay, editors, *Astronomical Data Analysis Software and Systems XXIII*, volume 485 of *Astronomical Society of the Pacific Conference Series*, page 277, May 2014.

F. Bonnarel, P. Fernique, O. Bienaymé, D. Egret, F. Genova, M. Louys, F. Ochsenbein, M. Wenger, and J. G. Bartlett. The ALADIN interactive sky atlas. A reference tool for identification of astronomical sources. *A&AS*, 143:33–40, April 2000. doi: 10.1051/aas:2000331.

ARRAKIHS Mission Consortium. Noise Budget, ARK-JST-SUR-AN-001, 12 2024. I4R0.

ARRAKIHS Mission Consortium. The ARRAKIHS Target Pool, ARK-JST-SUR-LI-001-I1R0, 03 2025.

ESA. Esa's new fast mission is arrakihs. https://www.cosmos.esa.int/web/call-for-missions-2021/selection-of-f2, 11 2022.

ESA. Euclid. https://www.esa.int/Science_Exploration/Space_Science/Euclid, 07 2023.

ESA. Cheops. https://www.esa.int/Science_Exploration/Space_Science/Cheops, date unkown.

ESSB-HB-E-003 Working Group. ESA pointing error engineering handbook, ESSB-HB-E-003, July 2011. I1R0.

European Cooperation for Space Standardization. *ECSS-E-ST-60-10C – Control performance*, November 2008.

C. Granabetter and R. Zoufal. ARRAKIHS IASW Software Requirements Specification, ARK-UVIE-ASW-SRS-001, March 2025. I1R2.

Karsten Großekatthöfer and Zizung Yoon. Introduction into quaternions for spacecraft attitude representation. Technical report, Technical University of Berlin Department of Astronautics and Aeronautics, Berlin, Germany, May 2012. URL https://argos.vu/wp-content/uploads/2017/01/Quaternions-1.pdf.

Prof. Rafael Guzmán. *ARRAKIHS Phase 2 Proposal*, 02 2022.

J. D. Hunter. Matplotlib: A 2d graphics environment. *Computing in Science & Engineering*, 9(3):90–95, 2007. doi: 10.1109/MCSE.2007.55.

IPAC. The Two Micron All Sky Survey at IPAC, 2006. URL https://www.ipac.caltech.edu/2mass/overview/about2mass.html. accessed 09.10.2025.

C. R. Kitchin. *Astrophysical Techniques*. CRC Press, 2020. doi: 10.1201/9780429491139.

Bogna Kubik, Remi Barbier, Eric Chabanat, Arnaud Chapon, Jean-Claude Clemens, Anne Ealet, Sylvain Ferriol, William Gillard, Aurelia Secroun, Benoit Serra, Gerard Smadja, and André Tilquin. A New Signal Estimator from the NIR Detectors of the Euclid Mission. *PASP*, 128(968):104504, October 2016. doi: 10.1088/1538-3873/128/968/104504.

Kin Lane. Intro to APIs: History of APIs, October 2019. URL https://blog.postman.com/intro-to-apis-history-of-apis/.

Carl C. Liebe. Pattern recognition of star constellations for spacecraft applications. *IEEE Aerospace and Electronic Systems Magazine*, 7(6):34–41, June 1992.

P. Loeschl, R. Ferstl, F. Kerschbaum, and R. Ottensamer. On-board target acquisition for CHEOPS. In Gianluca Chiozzi and Juan C. Guzman, editors, *Software and Cyberinfrastructure for Astronomy IV*, volume 9913 of *Society of Photo-Optical Instrumentation Engineers (SPIE) Conference Series*, page 99132W, July 2016. doi: 10.1117/12.2232726.

Philipp Löschl. Target Acquisition for Space Applications. Master thesis, University of Vienna, 2018.

Marty McCoy. James Webb Space Telescope. https://science.nasa.gov/mission/webb/, 09 2025.

Brian McLean. Guide Star Catalog (GSC) - MAST Data Holdings - MAST, October 2024. URL https://outerspace.stsci.edu/pages/viewpage.action?pageId=176435489.

Gerald Mösenlechner and Roland Ottensamer. ARIEL FGS IASW Centroiding for ARIEL, ARIEL-UVIE-PL-TN-001, November 2024. I1R5.

Gerald Mösenlechner, Roland Ottensamer, Armin Luntzer, Christian Reimers, Franz Kerschbaum, Miroslaw Rataj, and Konrad R. Skup. Architectural design of the ARIEL FGS software. In Juan C. Guzman and Jorge Ibsen, editors, *Society of Photo-Optical Instrumentation Engineers (SPIE) Conference Series*, volume 11452 of *Society of Photo-Optical Instrumentation Engineers (SPIE) Conference Series*, page 114521F, January 2021. doi: 10.1117/12.2562201.

Gerald Mösenlechner, Roland Ottensamer, and Franz Kerschbaum. Guiding and Target Acquisition for the Ariel Space Mission: Algorithms and Performance. In *European Planetary Science Congress*, pages EPSC2024–1190, September 2024. doi: 10.5194/epsc2024-1190.

Gerald Mösenlechner. Guiding and Target Acquisition for the ARIEL Space Mission. Master thesis, University of Vienna, 2021.

Gerald Mösenlechner. ARIEL HFS, 2024a. URL https://gitlab.phaidra.org/ottensr5/ariel-hfs. Version 1.3.3.

Gerald Mösenlechner. Stasis astrophysical image simulator, 2024b. URL https://github.com/geraldmoesenlechner/STASIS. Version 1.0.0.

Gerald Mösenlechner. *On-board data processing for the ARIEL payload*. PhD thesis, University of Vienna, 2026. to be released.

Paul Martini. Useful Astronomical Data. URL https://www.astronomy.ohio-state.edu/martini.10/usefuldata.html.

C. Rodrigo and E. Solano. The SVO Filter Profile Service. In *XIV.0 Scientific Meeting (virtual) of the Spanish Astronomical Society*, page 182, July 2020.

Carlos Rodrigo. SVO Filter Profile Service, 2025. URL https://svo2.cab.inta-csic.es/svo/theory/fps/index.php?mode=browse&gname=2MASS. accessed 20.07.2025.

Carlos Rodrigo, Enrique Solano, and Amelia Bayo. SVO Filter Profile Service Version 1.0. IVOA Working Draft 15 October 2012, October 2012.

Carlos Rodrigo, Patricia Cruz, John F. Aguilar, Alba Aller, Enrique Solano, Maria Cruz Gálvez-Ortiz, Francisco Jiménez-Esteban, Pedro Mas-Buitrago, Amelia Bayo, Miriam Cortés-Contreras, Raquel Murillo-Ojeda, Silvia Bonoli, Javier Cenarro, Renato Dupke, Carlos López-Sanjuan, Antonio Marín-Franch, Claudia Mendes de Oliveira, Mariano Moles, Keith Taylor, Jesús Varela, and Héctor Vázquez Ramió. Photometric segregation of dwarf and giant FGK stars using the SVO Filter Profile Service and photometric tools. *A&A*, 689:A93, September 2024. doi: 10.1051/0004-6361/202449998.

SATLANTIS. Space cameras - isim optical payloads. https://www.satlantis.com/space-cameras/, accessed 07.2025.

SATLANTIS. Satlantis - high resolution earth observation. https://www.satlantis.com, accessed 12.2025.

ARRAKIHS team members. Internal communications as part of ARRAKIHS development, 2025.

Pauli Virtanen, Ralf Gommers, Travis E. Oliphant, Matt Haberland, Tyler Reddy, David Cournapeau, Evgeni Burovski, Pearu Peterson, Warren Weckesser, Jonathan Bright, Stéfan J. van der Walt, Matthew Brett, Joshua Wilson, K. Jarrod Millman, Nikolay Mayorov, Andrew R. J. Nelson, Eric Jones, Robert Kern, Eric Larson, C J Carey, İlhan Polat, Yu Feng, Eric W. Moore, Jake VanderPlas, Denis Laxalde, Josef Perktold, Robert Cimrman, Ian Henriksen, E. A. Quintero, Charles R. Harris, Anne M. Archibald, Antônio H. Ribeiro, Fabian Pedregosa, Paul van Mulbregt, and SciPy 1.0 Contributors. SciPy 1.0: Fundamental Algorithms for Scientific Computing in Python. *Nature Methods*, 17:261–272, 2020. doi: 10.1038/s41592-019-0686-2.

A. Weigert, H. J. Wendker, and L. Wisotzki. *Astronomie und Astrophysik - Ein Grundkurs*. Wiley-VCH, 5th edition, 2009.

Y. Yang. Spacecraft attitude determination and control: Quaternion based method. *Annual Reviews in Control*, 36(2):198–219, December 2012. ISSN 13675788. doi: 10.1016/j.arcontrol.2012.09.003. URL https://linkinghub.elsevier.com/retrieve/pii/S1367578812000387.

Acronyms

ΛCDM Λ-Cold Dark Matter model. 1, 2

AOCS Attitude and Orbit Control System. 1, 31, 32, 37, 39, 40, 42–47, 49, 51, 53, 58, 64, 65, 68, 73, 75, 77, 79, 80, 82, 85

APE Absolute Performance Error. 8, 9

ARIEL Atmospheric Remote-sensing Infrared Exoplanet Large-survey. i, iii, v, 8, 10, 16, 17, 19, 21–23, 26, 28, 33, 39, 42, 85

ARRAKIHS Analysis of Resolved Remnants of Accreted Galaxies as a Key Instrument for Halo Surveys. iii, v, 1–5, 7, 8, 10, 19, 21–25, 28, 29, 31, 42, 49, 51, 53, 73, 78, 79, 81, 82, 85, 96

ASW Application Software. iii, v

CCD Charge-Coupled Device. 4, 22, 95

CDM Cold Dark Matter. 2

CMOS Complementary Metal–Oxide–Semiconductor. 4

CoG Center of Gravity. 19, 20

CPU Central Processing Unit. 46, 83

CSA Canadian Space Agency. 96

DC Dark Current. 5, 23, 24, 26, 29

DCM Direction Cosine Matrix. 11, 14, 42

DM Dark Matter. iii, v, 1

ESA European Space Agency. iii, v, 1, 44, 81, 95, 96

FF Full Frame. 22, 25, 26, 28, 32, 33, 37–39, 44, 45, 51, 68, 77, 78, 82, 83, 85, 86

FGS Fine Guidance System. iii, v, 1, 3, 5, 7, 8, 10, 16, 17, 21, 31, 44, 45, 81, 85

FoV Field of View. 3, 4, 17, 21, 24, 26, 28, 31, 33, 34, 51, 73, 80

FWC Full Well Capacity. 28, 29, 33

FWHM Full Width at Half Maximum. 51

HFS High Fidelity Simulator. 22

IHL Intra-Halo Light. 3

IR Infrared. 3, 96

IWC Intensity Weighted Centroiding. 19, 36, 38, 39, 75, 77, 85

IWCoG Iteratively Weighted Center of Gravity. 19, 39, 51, 85

LEO Low Earth Orbit. 7

LoS Line of Sight. iii, 7, 8, 15, 21–23, 25, 31, 40, 42, 52, 53, 56, 58, 59, 63–66, 69–72, 77–81, 85

MPE Mean Performance Error. 9

MW Milky Way. iii, 1, 2, 96

NASA National Aeronautics and Space Administration. 96

NIR Near Infrared. 1, 3–5, 37, 39, 44, 65, 95

PDE Performance Drift Error. 8, 9, 47, 81

PES Pointing Error Source. 8

PRE Performance Reproducibility Error. 9

PSF Point Spread Function. 19–21, 26, 33, 37, 38, 40, 50, 51, 60, 61, 65, 73, 78, 82

RAM Random Access Memory. 82

RN Readout Noise. 5, 23, 24

ROI Region of Interest. 17, 19, 36, 38, 50, 56, 75

RPE Relative Performance Error. 9, 60, 81

SAA South Atlantic Anomaly. 7

SB Surface Brightness. 1–3

SNR Signal to Noise Ratio. 65

UVIE University of VIEnna. iii, v, 16, 17

Glossary

2MASS The Two Micron All-Sky Survey (2MASS) was a NIR survey of the whole sky, which ended in 2003. The surveys scientific objectives included the large-scale structures of the Milky Way and the Local Universe, an first all-sky census of galaxies brighter than 13.5 magnitudes in the K band, and the discovery of new brown dwarfs and active galactic nuclei (IPAC, 2006). 24

ADU Analog to Digital Unit. The analog electrical signal produced by the electrons collected in the well of a CCD pixel is converted by an ADC (Analog-to-Digital Converter) into a digital number. The signal producing an output of one is called an Analog to Digital Unit (ADU). The so-called gain describes how many electrons produce an output of one ADU (Kitchin, 2020). 10, 28, 29, 33

API An API or Application Programming Interface describes a connection between computers or computer programs, which may also be connected via the internet, one side offering a service to the other (Lane, 2019). 24

CHEOPS The CHaracterising ExOPlanet Satellite is an ESA mission that launched in 2019 with the aim to study bright, nearby stars with known exoplanets in order to get their precise size via transit observations (ESA, date unkown). iii, v, 16–19, 33

Euclid The ESA mission Euclid is mapping the large-scale structures of the universe and studying the expansion and structure formation of the universe, the role gravity played in it and the nature of dark energy and dark matter. It was launched on July 1st 2023 (ESA, 2023). 7

F-class mission An F or *Fast* class mission is an ESA-led mission that aims to have a time of less than 10 years from selection to launch readiness (ESA, 2022). iii, v, 1

GSC The Guide Star Catalog (GSC) was first used to support the target acquisition and pointing of the Hubble Space Telescope (HST). Nowadays it is also used by additional missions like the JWST and ground based observatories (McLean, 2024). 24, 25

iSIM-170 The integrated Standard Imager for Microsatellites (iSIM)-170 is a high resolution optical imaging telescope developed by SATLANTIS for Earth observations (SATLANTIS, accessed 07.2025). 3, 4, 96

JWST The James Webb Space Telescope (JWST) is an IR observatory developed by NASA, ESA and CSA and launched in 2021. It aims to study the evolution of the universe from the Big Bang to our solar system (McCoy, 2025). 21, 22, 95

kpc 1 kpc = 1000 pc. 3, 96

M31 M31, also named the Andromeda Galaxy, is a galaxy close to the Milky Way. M31 and the MW are part of the so called local group (Weigert et al., 2009, page 425f). 2

MACC Multiple ACCumulated sampling (MACC) mode is a readout scheme used to reduce the effective readout noise. The detector is non-destructively read leading to an up-the-ramp (UTR) sampling and several readouts are averaged as a group. At the end of the exposure a fit of the group values is performed to obtain the signal from its slope. The implementation of MACC used in ARRAKIHS is described in Kubik et al. (2016). 5

Mpc 1 Mpc = 1 000 000 pc. 3, 96

pc A parsec is a unit of distance. An object is a distance of one parsec away from Earth if from the object's point of view the angle between the Sun and Earth's orbit is one arcsecond (Weigert et al., 2009, page 35f). 96

re-ionization Re-ionization was a phase in the development of the early universe where the light produced by the first generation of stars ionized the hydrogen gas between the first proto-galaxies. As a result the universe also became largely transparent for ultraviolet (UV) photons (Weigert et al., 2009, page 492). 3

SATLANTIS SATLANTIS is a space technology company specialized in Earth observation & universe exploration. They produce telescopes like the iSIM-170 which will be used by ARRAKIHS. Their headquarter is located in Spain (SATLANTIS, accessed 12.2025). 4

A. Non-Normalized Minimum Angle Quaternion

The following is a short validation showing that the minimum angle quaternion $\bar{q}_{min}$ calculated by Equation (1.12) is identical to the one from Equation (1.14), when the vectors $\vec{a}$ and $\hat{a}$, and $\vec{b}$ and $\hat{b}$ are pointing in the same direction and $\hat{a}$ and $\hat{b}$ are unit vectors. $\hat{e}$ denotes the unit vector perpendicular to the other vectors and satisfies the right-hand rule. θ is the rotation angle between them.

$$(1.14) = \begin{pmatrix} ||\vec{a}||\,||\vec{b}|| + \vec{a}\vec{b} \\ \vec{a} \times \vec{b} \end{pmatrix} \frac{1}{\sqrt{(||\vec{a}||\,||\vec{b}|| + \vec{a}\vec{b})^2 + ||\vec{a} \times \vec{b}||^2}} = \frac{1}{\sqrt{2(1 + \hat{a} \cdot \hat{b})}} \begin{pmatrix} 1 + \hat{a} \cdot \hat{b} \\ \hat{a} \times \hat{b} \end{pmatrix} = (1.12)$$

$$\vec{a}\vec{b} = ||\vec{a}||\,||\vec{b}|| \cos\theta, \quad \vec{a} \times \vec{b} = \hat{e}||\vec{a}||\,||\vec{b}|| \sin\theta$$

$$\begin{pmatrix} ||\vec{a}||\,||\vec{b}||(1 + \cos\theta) \\ \hat{e}||\vec{a}||\,||\vec{b}|| \sin\theta \end{pmatrix} \frac{1}{\sqrt{(||\vec{a}||\,||\vec{b}||)^2 (1 + \cos\theta)^2 + ||[\hat{e}||\vec{a}||\,||\vec{b}|| \sin\theta]||^2}} = \frac{1}{\sqrt{2(1 + ||\hat{a}||\,||\hat{b}|| \cos\theta)}} \begin{pmatrix} 1 + ||\hat{a}||\,||\hat{b}|| \cos\theta \\ \hat{e}||\hat{a}||\,||\hat{b}|| \sin\theta \end{pmatrix}$$

$$||\hat{a}|| = ||\hat{b}|| = 1, \quad ||\hat{e}|| = 1$$

$$\begin{pmatrix} 1 + \cos\theta \\ \hat{e} \cdot \sin\theta \end{pmatrix} \frac{\cancel{||\vec{a}||\,||\vec{b}||}}{\sqrt{(\cancel{||\vec{a}||\,||\vec{b}||})^2 (1 + \cos\theta)^2 + (\cancel{||\vec{a}||\,||\vec{b}||} \sin\theta])^2}} = \frac{1}{\sqrt{2(1 + \cos\theta)}} \begin{pmatrix} 1 + \cos\theta \\ \hat{e} \cdot \sin\theta \end{pmatrix}$$

$$\frac{1}{\sqrt{(1 + \cos\theta)^2 + \sin\theta^2}} = \frac{1}{\sqrt{2(1 + \cos\theta)}}$$

$$1 + 2\cos\theta + \underbrace{\cancel{\cos\theta^2 + \sin\theta^2}}_{1} = 2(1 + \cos\theta)$$

$$2 + 2\cos\theta = 2(1 + \cos\theta)$$

$$1 = 1$$